Alma Mater Studiorum – Università di Bologna

DOTTORATO DI RICERCA IN

FISICA

Ciclo 29°

Settore Concorsuale di afferenza: 02/B1

Settore Scientifico disciplinare: FIS/03

ADVANCES IN NANOPARTICLE CONDENSATION FROM THE GAS PHASE: MG-BASED AND TiO_2-BASED MATERIALS FOR ENERGY APPLICATIONS

Presentata da: Marco Calizzi

Coordinatore Dottorato

Prof. Gastone Castellani

Relatore

Prof. Luca Pasquini

Esame finale anno 2017

"I have always thirsted for knowledge,
I have always been full of questions."
- Siddartha

ABSTRACT

This Thesis aims to study nanoparticles (NPs) synthesised via condensation from the gas phase. The advances achieved with this technique, first of all the development of a controlled reactive atmosphere and *in situ* capabilities, are presented. With the set-up developed, it is possible to synthesise NPs of a variety of compounds: alloys, oxides, hydrides, and also complex morphologies like nanocomposites and core-shell structures.

Mg-based NPs are studied for their interest in hydrogen storage applications. Firstly, the problem of severe crystal growth in metallic Mg NPs is addressed. The dynamics of the self-assembly process is studied and the synthesis of Mg metal-oxide core-shell NPs is proved as a way to stabilise small size (in the 20-30 nm range) NPs.

Addition of Ti is known to improve the hydrogen storage properties of Mg. Mg-Ti NPs in the form of air-stable pellets or nanopowders, are synthesised via condensation from inert or hydrogen rich atmosphere. The resulting MgH_2-TiH_2 nanocomposites show excellent hydrogen sorption kinetic properties with fast hydrogen absorptions as well as desorptions observed at temperatures as low as 343 K. Slight to no thermodynamics changes compared to the bulk Mg-H system are retrieved over a wide, low temperature range.

Finally, the addition of V is studied as a method to improve light absorption in the visible range and photocatalytic efficiency of TiO_2 NPs. A deep characterisation of the overall V-TiO_2 NPs structure, morphology and optical properties is carried out along with the characterisation of the local chemical environment of the V ions, proving that V is always substitutional of the cation in TiO_2, irrespective of the TiO_2 polymorph present.

CONTENTS

1 Introduction

In a world where both human population and consumption of resources per individual are growing with increasing rates, our existence's sustainability for the planet has become an issue more and more important and urgent as time passes. "The Millennium project", a non-profit global research think tank[1], identifies 15 global challenges facing humanity among which there are:

- How can sustainable development be achieved for all while addressing global climate change?
- How can population growth and resources be brought into balance?
- How can growing energy demands be met safely and efficiently?

Clearly, the answer to these questions will not be found in the following pages, but the intention is to move small steps towards that direction. The problem of creating a sustainable energy cycle is deeply linked to all the above mentioned global challenges. Energy harvesting, storing, transport and consumption are the four main steps of an energy cycle, and to achieve sustainability, not only each step has to be respectful of the environment, but the whole cycle has to be durable in time, *i.e.* the energy source has to be renewable and there must be no waste products.

From a physicist's point of view, the Earth is a closed system: it does not exchange (or better, exchanges a negligible amount of) matter with the outer space, but it does exchange energy. The main energy income comes from the Sun, which irradiates the Earth with an annual average power of 1.730×10^{17}

W or 173'000 TW (terawatts).[2] For comparison, in 2014 on average the humanity consumed 12.5 TW.[3] Therefore, solar energy can be considered as the ultimate energy source, even fossil fuels can be seen as solar energy stored from life forms that lived in the past. From this perspective, burning fossil fuels is like consuming the solar energy of the past and this is not sustainable because someday, long before their depletion, the energy required for the extraction of oil will be greater than the energy that oil can supply. We need to find equilibrium with the present energy income, harvesting efficiently solar energy (or wind or water, always derived from the sun) and converting it into a useful form, mainly electrical, thermal or chemical.

Electricity is almost a synonym of energy, it is the most diffuse energy form because it can be efficiently transported over long distances and is the most versatile: we know how to transform it into heat, motion, light and is the energy form needed for most machines and devices. The downside is that the electrical energy produced cannot be stored economically in large quantities or for a long time. This leads to the second point of the energy cycle, energy storage. The lack of a satisfactory storing system, of no matter which energy form, is an issue the general public is not aware of but it is, nevertheless, critical. As renewable energy sources become more diffuse, their intrinsic intermittence has to be dealt with. For example, solar energy is harvested during the day, but it cannot be used during the night, or in winter we need more power to heat buildings but there is less sunlight, while in summer it is exceedingly abundant but wasted. Today, energy is not stored at all, power has to be constantly produced, more than the demand, and the excess is lost. Not to mention the problem of storing energy in vehicles, electric and hydrogen powered cars have started mass production in the last few years only, being the development of a "fuel tank" one of the major obstacles.

These are complex political, economic and technological problems. In this picture scientific research, both fundamental and applied, is the sparkle that triggers the innovation. Research on new materials is at the base of the development and improvement of new energy harvesting and storing technologies, and when they will become more convenient than the current there will be enough driving force to switch to a 100% sustainable energy cycle.

The materials studied in this Thesis are "new" in the sense that they are in the form of nanoparticles (NPs). The term nanoparticles, or ultrafine particles, usually refers to particles of size between 1 and 100 nm (nanometers, millionth of millimeter).

A bulk material has constant physical properties regardless of its size, at the nanometric scale instead NPs show size-dependent properties. In general, interesting and genuinely new properties make their appearance when the particle size is reduced and becomes smaller or of the same magnitude as the lenght scale of a physical quantity. Plasmonics, an entirely new field of material science, was opened by the change of optical properties in NPs: being much smaller than the wavelength of visible light (380-760 nm), a NP can couple with it generating collective oscillations of all the free electrons of the NP (a plasmon), exhibiting interesting scattering and absorbance properties with many applications including solar cells, spectroscopy, signal enhancement for imaging, and cancer treatment. Another example is superparamagnetism, a phenomenon which appears in ferromagnetic or ferrimagnetic materials: because of thermal fluctuations, if the NPs are sufficiently small, their magnetization appears to be in average zero, similarly to a paramagnet but with a much larger magnetic susceptibility, with strong implications on the limit on the data storage density in magnetic recording (hard disk drives).

As the average particle size of a material decreases, the surface-to-volume ratio dramatically increases. For this purely geometric feature, a catalyst, a material that promotes a chemical reaction at its surface, if composed of NPs is much more active than its bulk counterpart. To give an idea, 1 kg of particles of 1 mm^3 has the same surface area as 1 mg of particles of 1 nm^3. This approach can be extended to all cases where is needed a fast and strong chemical interaction of a material with its surroundings through the surface.

All the mentioned applications may sound "hi-tech" but the use of NPs goes back in time, and being the simplest nanoscopic structure,

Figure 1.1 The Lycurgus cup, British Museum. The cup looks opaque green when lit from outside (left) and translucent red when light shines through the inside (right), because of the NPs in the glass.

in some cases are formed even spontaneously, like in the smoke of a bonfire or when light bulbs burn. The first uses of NPs are recorded in ancient history; it is famous the case of the Lycurgus Cup (4th century, Rome), the first example of dichroic glass: because of the gold and silver NPs in the glass, the cup looks opaque green when reflecting light but translucent red when light is transmitted through the glass (Figure 1.1)[4].

The origin of the booming interest of scientific research on NPs in the last decades has to be found in the development of characterisation techniques, rather than in NP production methods. The world of NPs has been made accessible thanks to new imaging techniques and nano-probes that allow morphological analysis down to atomic-level resolution, such as field-emission scanning electron microscopes, atomic force microscopy, and transmission electron microscopy. Supported and pushed by proper characterisation means, in the last decades physicists and chemists developed several methods for NPs preparation. These can be broadly divided into top-down techniques, where nanoparticles are obtained starting by bulk material and dividing it into smaller and smaller parts, and bottom-up methods, where nanoparticles nucleate from atomic or molecular precursors.

In this Thesis are presented the improvements on a bottom-up technique, the condensation of NPs from the gas phase, employed in the synthesis of magnesium-based and titanium dioxide-based materials. These classes of materials have great potential applications in the development of a sustainable energy cycle but both applied and fundamental research need to overcome some major problems for their wide technological use. In the dedicated chapters, the energy applications of each type of material are described in more detail and the interest in their synthesis in form of NPs is motivated.

2 The Gas Condensation Technique

All the materials studied in this Thesis were synthesised by Inert Gas Condensation (IGC), a bottom-up physical vapour deposition technique for production of nanoparticles (NPs). In the 1930s, the pioneers of this technique Pfund, Burger and van Cittert, Harris *et al.*[5], were able to evaporate only few metallic elements but thanks to the development of set-ups and procedures today it is possible to synthesise also composites, alloys, core-shell structures, oxides, nitrides, and, for the first time in this work, hydrides. This technique has been extensively employed for the synthesis of loose nanopowders[5], porous nanoparticle assembled films[6] and bulk nanocrystalline materials[7]. In the following sections will be described the theory of NP formation, the unique set-up developed through this Thesis and the techniques routinely used to characterise the NPs.

2.1 Theory of Nanoparticle Formation

Like the other vapour deposition techniques, IGC is a bottom-up synthesis method. Here, vapour is produced heating the precursor material then the hot vapour is quickly cooled by a flow of inert gas, typically He or Ar. Despite the decrease of the vapour's partial pressure caused by the dilution

of the vapour in the inert gas, the cooling effect of the inert gas flow decreases the equilibrium vapour pressure at a faster rate, bringing the system in supersaturation conditions in order to have the gas-to-solid phase transition.

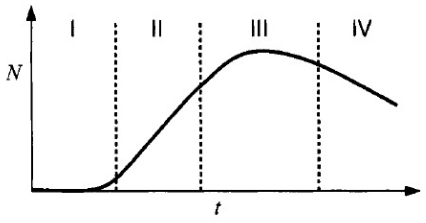

Figure 2.2 Time evolution of the number of particles formed during a discontinuous transformation.

Being a discontinuous transition, NP formation follows four stages, as showed in Figure 2.2 and visualised in Figure 2.1:

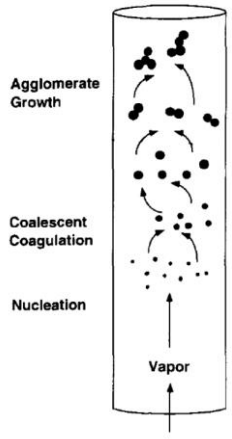

Figure 2.1 Schematic representation of the growth of particles from the gas phase.

I. The i*ncubation period*, where the gas is metastable and small clusters are continuously formed and disrupted; the cluster distribution evolves in time to produce larger clusters and eventually stable NPs.

II. The *quasi-steady-state nucleation* regime the cluster distribution has reached a quasi-stable state and NPs are being produced at a constant rate.

III. In this stage of the transformation nucleation rate decreases and the number of formed NPs is almost constant (usually due to a decrease in supersaturation of the gaseous phase).

IV. The final stage, where nucleation of new NPs is negligible and the already existing ones grow, the larger at expense of the smaller, decreasing the total number of particles.

With IGC, the system is kept out of equilibrium by continuously producing vapour so that the *quasi-steady-state nucleation* regime (stage II) is stabilised and NPs are produced for as long as wanted.

To better understand how NPs nucleate from the saturated vapour, the classical theory of homogeneous nucleation is presented.[8] In this classical model the free energy of a solid cluster of *N* atoms, ΔG_N, is assumed to be separable into bulk free energy and interface free energy:

$$\Delta G_N = \Delta G_N^{bulk} + \Delta G_N^{interface} = N(\mu_{solid} - \mu_{vapour}) + \eta N^{2/3}\gamma \quad (2.1)$$

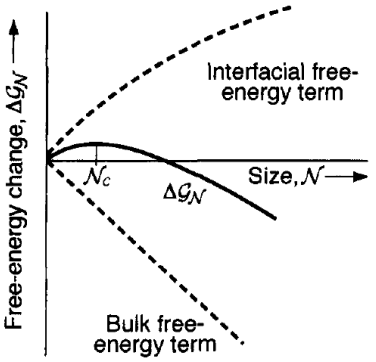

Figure 2.3 Free energy of a cluster composed of N atoms. The dashed lines show the two terms that contrubute to the total free energy, the bulk and the interface term.

where μ is the chemical potential, η a shape factor and γ the interfacial energy per unit area. Here we assume the cluster to be isotropic, therefore it will assume a spherical shape to minimize its surface. The anisotropic case can be treated likewise, replacing the interface free energy term with the sum of the contributions of each facet. Since the vapour is supersaturated, it is unstable towards its condensation, meaning that $\mu_{solid} < \mu_{vapour}$ and therefore $\Delta G_N^{bulk} < 0$. In Figure 2.3 is plotted the total free energy of the cluster as a function of *N*. The maximum free energy is reached at the critical size N_C that can be calculated looking for the maximum from $\frac{d\Delta G_N}{dN} = 0$:

$$N_C = -\frac{8}{27}\left(\frac{\eta\gamma}{\mu_{solid} - \mu_{vapour}}\right)^3. \tag{2.2}$$

The clusters composed of $N < N_C$ atoms are unstable and will probably decompose back to the vapour phase. It can be demonstrated then, that the steady state nucleation rate is

$$J = \sqrt{\frac{\Delta G_C}{3\pi N_C^2 kT}}\beta_C N e^{-\Delta G_C/kT} \tag{2.3}$$

where β_C is the rate at which single atoms from the vapour phase join a cluster of size N_C, k is the Boltzmann constant, T is the temperature and ΔG_C is the free energy of a cluster of size N_C. The factor under the square root is called the *Zeldovich factor* and takes into account the probability that even clusters beyond the critical size can decay back to smaller ones. The typical order of magnitude of this factor is 10^{-1}.

2.2 IGC set-up description

The IGC synthesis apparatus was realised *ad hoc* and is always under development. The instrument is sketched in Figure 2.4 for a more clear understanding. It is composed of a main cylindrical *Thermionics* ultra high vacuum stainless steel chamber, 70 cm high with an internal diameter of 45 cm for a total volume of ~110 dm^3, and a smaller secondary chamber connected to the main one via a gate valve. The chambers have separated vacuum systems both composed of a *Varian TURBO* turbomolecular pump backed by an *Edwards* rotary pump. They are both equipped with two pressure sensors: a *Varian ConvecTorr p-type* Pirani gauge and a *Varian* inverted magnetron gauge. The main chamber is also equipped with a *Varian* ceramical capacitance diaphragm gauge, used during evaporation because it is not sensitive on the type of gases in the atmosphere, and with a *Pfeiffer-Vacuum Prisma QMS200* quadrupole mass spectrometer to monitor the quality of the vacuum. The base pressure reached is 10^{-8} mbar.

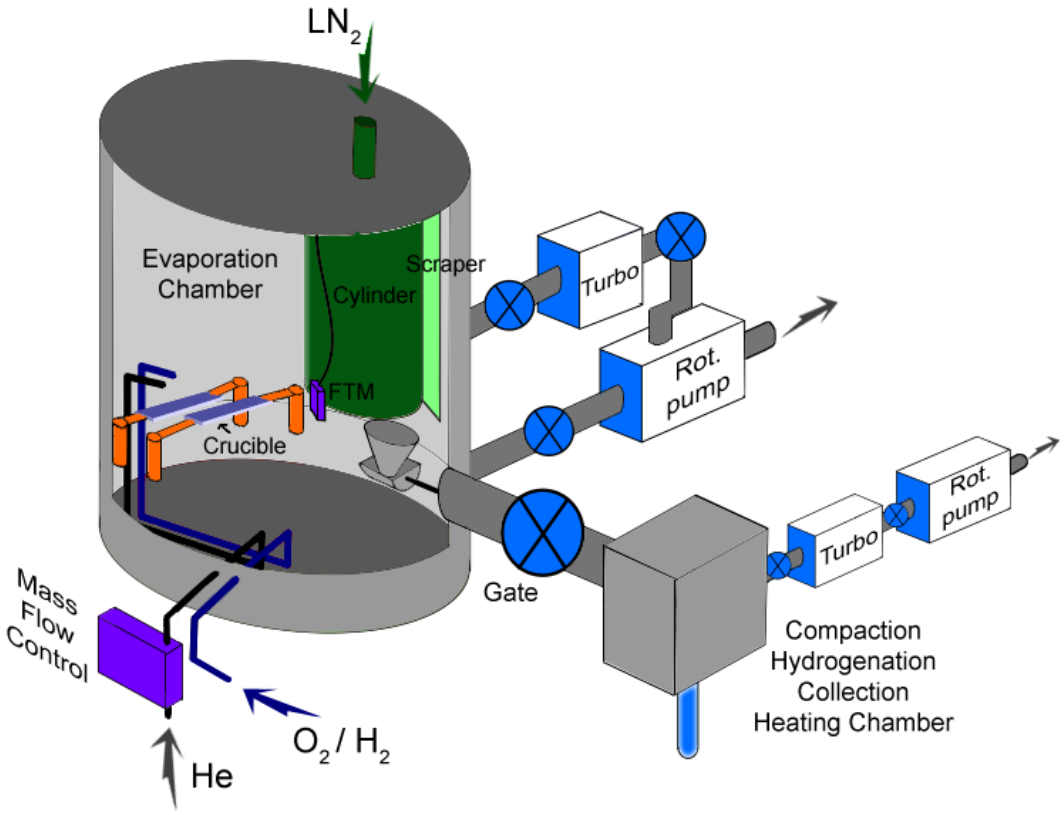

Figure 2.4 Illustration showing the disposition of the main elements of the evaporation chamber, the secondary chamber and their independent vacuum systems.

The main chamber

Inside the main chamber there are two couples of copper electrodes that can hold two tungsten crucibles for heating the precursor materials by Joule effect. The copper electrodes are connected to two independent high-amperage *Thermionics* alternate current generators, up to $I_{eff} \approx 500$ A. The inert gas flow is realised with 99.9999% pure Helium; the inlet is controlled by a *Bronkhorst EL-FLOW* mass flow controller and directed towards the collecting site passing over the crucibles. Once reached the desired pressure, to keep the pressure constant the gas outlet is balanced with the rotary pump, pumping through a needle valve that bypasses the turbomolecular one. Usually, the volumetric flow rate is set between 7 ml_n/min and 65 ml_n/min, and the pressure is kept at 2 Torr (*i.e.* 270 Pa).

The NPs are collected on a steel cylinder 305 mm high and 150 mm large mounted on the chamber lid, free to rotate on its axis and moved by an external motor. The cylinder is hollow and can be filled with liquid nitrogen to improve collection efficiency, thanks to the thermophoretic effect caused by the temperature gradient between the hot crucible and the cold cylinder. The cylinder can be used either for the synthesis of nanoparticulate films on substrates, or for the massive collection of NPs for the synthesis of "nanopowders". In the first case, NPs can be deposited on any substrate attached to the cylinder and thanks to the cylinder's mobility the exposure of the substrates to the NP flow can be controlled. In the second case, the liquid nitrogen-cooled cylinder surface is directly used for the NP collection while it is continuously rotating.

The advance of the evaporation is monitored with an *Edwards Film Thickness Monitor FTM7* quartz microbalance positioned next to the cylinder facing the crucibles. Measuring this parameter is fundamental for controlling the rate of deposition and the total amount of material produced, but doing it is not as straightforward as it is usually for atomic depositions in vacuum where the layer deposited is compact and uniform over a wide solid angle. In the case of IGC instead, the FTM underestimates the real thickness because when NPs stack on each other leave a lot of empty spaces. Also, the majority of NPs is carried by the He flow which is directed towards the cylinder, therefore the deposition is not uniform at all over the solid angle, underestimating even more the real thickness deposited.

After the evaporation, the nanopowder can be scraped off the the cylinder's surface and collected in a cup under the scraper (see Figure 2.4).

Reactive gas condensation (RGC)

The main chamber has been upgraded during this Thesis with the possibility to add reactive gases during evaporation, *i.e.* H_2 (99.9999% purity) and O_2 (99.9999% purity). The flow of these gases can be accurately set controlling the pressure in a gas lines connected to the chamber through a needle valve. The gas lines volumes are big enough to assure the flow rate is constant over the duration of the experiment when H_2 and O_2 expand on the main chamber. The gas inlet is in different positions depending on which reactive gas is used: in the case of H_2 it is next to the He inlet (Figure 2.5) so that the evaporated materials see a mixture of He and H_2 along all the path to the collecting cylinder. In the case of O_2, the inlet is between the crucible(s) and the cylinder (Figure 2.6) to avoid the oxidation of the tungsten crucible or of the precursor material, that would inhibit its evaporation.

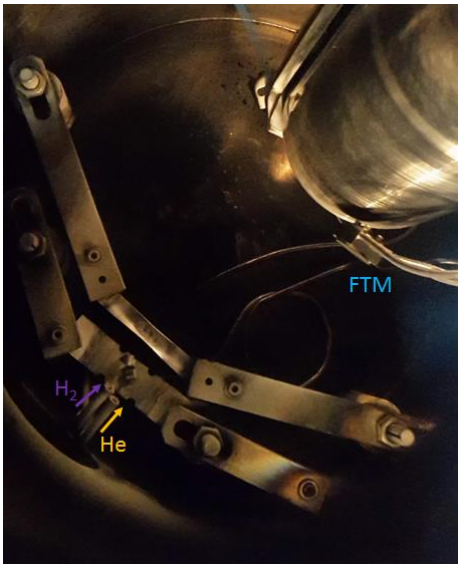

Figure 2.5 The main chamber in the double crucible configuration, with the H_2 inlet next to the He.

Demonstrations of reactive gas condensed NPs will be shown, at the end of Chapter 4 with oxygen for the synthesis of Mg/MgO core/shell structures, in Section 5.2 with hydrogen for the synthesis of Mg-Ti-H NPs.

The secondary chamber

Once the nanopowders are scraped from the cylinder and collected into the cup, the cup is moved to the secondary chamber through the gate valve by a linear positioner manually actuated from outside the chambers, via magnetic coupling. In the secondary chamber, the nanopowder can be annealed in vacuum or H_2 atmosphere up to ~520 K.

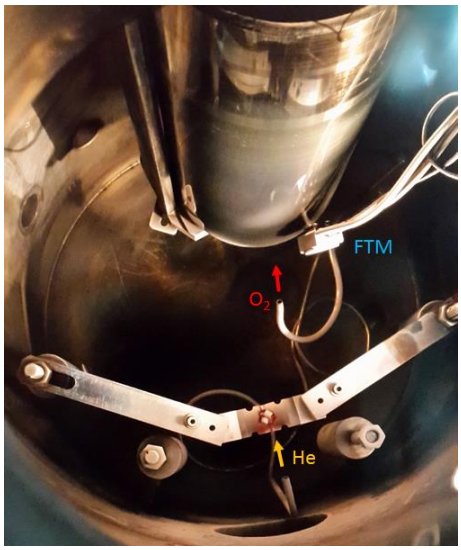

Figure 2.6 During reactive gas synthesis using O_2, the O_2 inlet is along the He flow, after the crucible to avoid oxidation of the hot source.

Depending on how the chamber is prepared, the nanopowder is poured in a

borosilicate glass vial mounted on the bottom of the chamber or in a piston where it can be compacted into a pellet by a *SPX Power Team 100TON* idraulic press.

This chamber can also be used as an *in situ* Sievert apparatus: being the volume calibrated and the temperature controlled, solid-gas reactions, *i.e.* gas absorptions or desorptions, are studied by measuring pressure changes in the $10^0 - 10^5$ Pa range.

To extract the sample under inert atmosphere, a glovebag is sealed to the secondary chamber's bottom and filled with Ar; the bottom of the chamber is then opened and the nano-pellet or the nanopowder in the vial is extracted with no exposure to the atmosphere.

2.3 Laboratory characterisation techniques

Depending on the particular properties studied, many different investigation techniques are used in this Thesis, but a general characterisation is always carried on each sample. The combined use of scanning electron microscopy (SEM), energy dispersive x-ray spectroscopy (EDX) and powder x-ray diffraction (XRD) gives a lot of information without any special sample preparation. The typical morphological and structural properties revealed are estimation of NP size and shape, aggregation level, elemental composition, quantitative phase composition and crystallite size (mostly important when related to the NP size).

Another very powerful technique for the characterisation of NPs that has been often used is transmission electron microscopy (TEM), since it allows observations on single nanoparticles.

An important part of this work is also dedicated to the characterisation of the hydrogen storage properties of Mg-Ti NPs. Both kinetic and thermodynamic H-sorption properties are mainly investigated with the volumetric method, using a Sievert apparatus.

In the following, is given a short description of the instruments from the University of Bologna used for this routine characterisation.

Scanning electron microscopes

Most of the SEM pictures of this Thesis are taken with a *Leica Cambridge Stereoscan 360* SEM, using a tungsten filament as electron source, 20 kV of acceleration potential and a secondary electrons detector.

The microscope is also equipped with an *Oxford Instruments X-Sight* that uses a Si(Li) x-ray detector for EDX measurements.

Higher quality observations were possible using a Leo Zeiss 1530 Gemini field emission SEM (FE-SEM) thanks to the collaboration with IMM - CNR, Bologna, Italy.

Transmission electron microscope

Again, thanks to the collaboration with IMM - CNR, TEM observations were made using a FEI Tecnai F20 ST Transmission Electron Microscope that can be operated in high-resolution mode (HR-TEM), high angle annular dark field scanning mode (HAADF-STEM) and can perform elemental profiling (EDX-TEM) with a spatial resolution of about 2 nm.

X-ray diffractometer

XRD patterns were collected with a PANalytical X'celerator diffractometer using Cu-K_α radiation (1.5406 Å), working in the Bragg-Brentano $\theta - 2\theta$ geometry.

XRD data were quantitatively analysed using the MAUD Rietveld refinement software[9].

Sievert apparatus

H-sorption measurements were made mainly with a home-built Sievert apparatus. It was designed with minimal volumes to be able to measure even a few milligrams of material. The whole system is thermalised in water while the sample holder can be heated in a tubular oven up to ~750 K. H_2 pressure can be applied in a range that spans from rotary pump-quality vacuum up to 20 bar and is measured with 10^{-3} bar accuracy. Gas inlet, outlet and the connections of the sample holder to the rest of the system are controlled through pneumatic valves by the HSA program, a LabVIEW-based software for the measurement of gas-solid reactions.

3 MG-BASED MATERIALS

In this Chapter is presented the work done on Mg-based NPs. Starting from the characterisation of simple metallic Mg NPs, acquiring experience and control of the system, it has become possible to synthesise also Mg-Ti alloys, MgH_2-TiH_2 composites. The main application for these materials is solid state hydrogen storage, one of the main research fields of this Thesis. In the following section is therfore resumed the basic theory of the metal-hydride transition, followed by the studies on Mg-only NPs and on Mg-Ti NPs.

3.1 Metal Hydrides for H-storage

The first observation of large quantities of H_2 by a metal dates back to 1866, when Thomas Graham was studying Palladium:

"Spongy palladium, from the ignition of the cyanide, being heated in hydrogen at 200C, and allowed to cool slowly in the same gas for four hours, the metal was found to have taken up 686 vols. of hydrogen." [10]

Since then, the interaction between hydrogen and metals has been studied for scientific curiosity and for applications in the field of hydrogen purification, getter pumps and Ni-MH batteries. However, it is in modern times, pushed by the need of creating a new energy economy, that the research is focussing systematically and with more interest on these materials and their

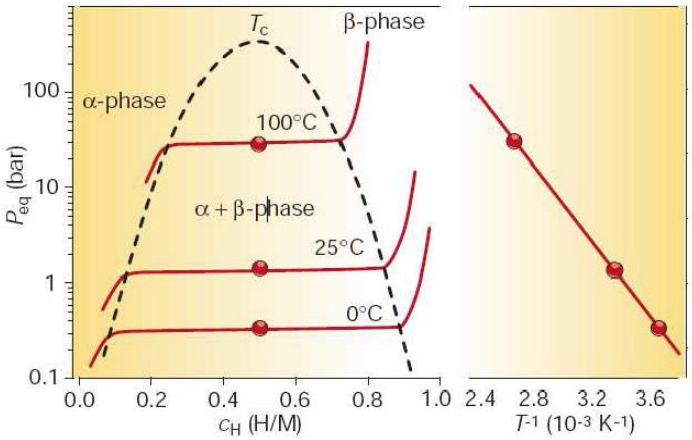

Figure 3.1 (left) Pressure-composition isotherm (PCI) plots overlaid to the phase diagram for a generic MH system; (right) the van 't Hoff plot of the corresponding equilibrium points.

ability to store hydrogen. In the next subsections will be presented thermodynamic and kinetic phenomena of metal hydride systems, both important to characterise the hydrogen storage properties of materials.

Thermodynamics

The reaction of molecular hydrogen with a metal M is of the type

$$M + \frac{x}{2} H_2 \rightarrow MH_x + \delta Q \tag{3.1}$$

where δQ is the heat absorbed by the system, therefore $\delta Q < 0$ for exothermic reactions. In the following, α will be the metallic phase (which can contain some H atoms in solution in the lattice) and β the hydride phase. Below the critical temperature T_C, there is a miscibility gap of α and β phases, and the system is separated in the two phases with concentrations c_α and c_β, respectively. As displayed in Figure 3.1, as long as the system is in the miscibility gap, there is a constant pressure P_{eq}, and any H_2 addition or removal does not affect this equilibrium pressure but will change the α-to-β concentration ratio. The temperature dependence of P_{eq} is described by the van 't Hoff equation which is obtained from classical thermodynamic considerations.
In analogy with Equation (3.1), the transformation from α to β is written

$$2MH_{c\alpha} + (c_\beta - c_\alpha) H_2 \rightarrow 2MH_{c\beta} \tag{3.2}$$

At equilibrium, the same reaction can be written in terms of the chemical potentials μ for each element in each phase:

$$2\ \mu_{\alpha}^{M} + c_{\alpha}\mu_{\alpha}^{H}\ + (c_{\beta} - c_{\alpha})\mu_{H_2} = 2(\mu_{\beta}^{M} + c_{\beta}\mu_{\beta}^{H}) \tag{3.3}$$

where μ_{H_2} is the chemical potential of gaseous molecular hydrogen, μ_{α}^{M} and μ_{α}^{H} the chemical potentials of the metal and the hydrogen in phase α, μ_{β}^{M} and μ_{β}^{H} in phase β. Chemical potential μ can be written as

$$\mu = \left(\frac{\partial G}{\partial n}\right)_{p,T} = \left(\frac{\partial H}{\partial n}\right)_{p,T} - T\left(\frac{\partial S}{\partial n}\right)_{p,T} = \bar{H} - TS \tag{3.4}$$

where $\bar{H}$ and S are the molar partial enthalpy and entropy. Substituting the last relation in Equation (3.3) we obtain

$$\Delta H_{\alpha\to\beta} = T\Delta S_{\alpha\to\beta} \tag{3.5}$$

with

$$\begin{aligned} \Delta H_{\alpha\to\beta} &= 2\frac{H_{\beta} - H_{\alpha}}{c_{\beta} - c_{\alpha}} - \bar{H}_{H_2} \\ \Delta S_{\alpha\to\beta} &= 2\frac{S_{\beta} - S_{\alpha}}{c_{\beta} - c_{\alpha}} - S_{H_2} \\ H_i &= \bar{H}_i^{M} + c_i\bar{H}_i^{H} \qquad (i = \alpha, \beta) \\ S_i &= S_i^{M} + c_i S_i^{H} \qquad (i = \alpha, \beta) \end{aligned} \tag{3.6}$$

From classical thermodynamics it is known that partial molar entropy has a logarithmic dependence from pressure

$$S_{H_2} = R\ln\left(\frac{p}{p_0}\right) + S_{H_2}^{0} \tag{3.7}$$

where $R = 8.314$ J mol^{-1} K^{-1} is the ideal gas constant and $S_{H_2}^{0} \approx -130$ J mol^{-1} K^{-1} is the molar entropy at standard conditions ($p = p_0 = 1.013 \cdot 10^5$ Pa, $T = 273.15$ K). Actually, $S_{H_2}^{0}$ has a slight logarithmic pressure dependance

too, but it is negligible in the temperature range $300\ \text{K} < T < 800\ \text{K}$. Combining (3.7) and (3.5), it is found the well-known $\text{van' t Hoff equation}$:

$$\ln\left(\frac{p_{eq}}{p_0}\right) = \frac{\Delta H_{\alpha\to\beta}}{RT} - \frac{1}{R}\left(2\frac{S_\beta - S_\alpha}{c_\beta - c_\alpha} - S^0_{H_2}\right) \tag{3.8}$$

This equation shows that the relation between temperature and equilibrium pressure p_{eq} depend on the enthalpy and entropy of the α to β transition. Measuring equilibrium points is therefore very important for the thermodynamic characterisation of a metal-hydrogen system, which gives information on heat transfers and driving force of the reaction.

Kinetics

While thermodynamics give information about the ambient conditions at which a transformation takes place and its driving force, it cannot predict how long will it take. The kinetic study of a reaction focusses on what happens between the initial and final states studied by thermodynamics. In Figure 3.2 is plotted the free energy of a single atom (or molecule, or ion) following a spontaneous process, *i.e.* where the final state has a lower energy than the initial $G_F < G_I$. The energy difference between final and initial states is the driving force $\Delta G = G_F - G_I$, but in order to undergo the transformation, the atom has to be in a higher energy state, the activated state. The energy barrier ΔG_A between the activated and initial states determines the overall rate of transformation, because thermal fluctuations give enough energy to some atoms to pass over the energy barrier. This phenomenon is called thermal activation.

The progress of a metal-to-hydride transition or vice-versa as a function of time, is usually modeled with the Johnson-Mehl-Avrami-Kolmogorov (JMAK) phase transition theory on random nucleation and growth. The hypotheses of this model are:

i. the nucleation sites of the new phase are randomly distributed in the sample's volume and surface;

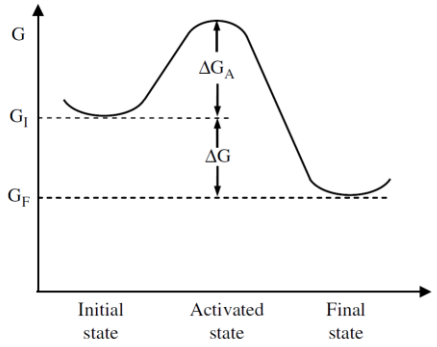

Figure 3.2 Free energy of a general thermodynamically favoured transformation from an initial to a final state passing through an energy barrier.

ii. the sample's dimensions are much larger than those of each transformed region;

iii. the nucleation rate is constant.

It must be remarked that in reality, because of the finite size of the sample, this model does not apply in the final part of the transformation where hypotheses *ii* and *iii* are no longer valid.
Being $\alpha(t)$ the transformed fraction, from JMAK theory it is known that

$$\alpha\ t\ = 1 - \mathrm{e}^{-\ \mathrm{kt}\ ^{n}} \tag{3.9}$$

The parameters that describe the transformation kinetics, like nucleation rate and growth rate, contribute to the k parameter. Analysis of the temperature dependence of k gives a measure of the activation energy ΔG_A through the relation

$$k(T) = k_0 e^{-\Delta G_A/RT} \tag{3.10}$$

The second parameter of Equation (3.9), the order of reaction n also called Avrami exponent, conveys some information on the geometry of the reaction mechanisms. It is the sum of other parameters:

$$n = a + bc \tag{3.11}$$

where a is related to the nucleation rate and equals 0 when nucleation is instantaneous and 1 when it is constant; b is the dimensionality of the growth and c equals 0.5 or 1 when the growth is diffusion or interface controlled, respectively. In a metal to hydride transition, the rate limiting step is generally considered to be the slow motion of H atoms in the hydride phase, meaning that absorptions are diffusion controlled ($c = \frac{1}{2}$) while desorptions are interface controlled ($c = 1$).

3.2 Magnesium and magnesium hydride

Mg has *hcp* structure with cell parameters[11] $a = 3.2094$ Å and $c = 5.2108$ Å, while the most stable allotrope of its hydride, β-MgH_2, has a rutile-type *bct* structure with cell parameters[12] $a = 4.5010$ Å and $c = 3.0100$ Å (see Figure 3.3). As it usually happens in metal to hydride transitions, the Mg to MgH_2 reaction takes place with a great volume expansion, which can be calculated from the volume ratio of the unit cells:

$$\frac{V_{MgH_2}}{V_{Mg}} = \frac{a^2_{MgH_2} c_{MgH_2}}{a^2_{Mg} c_{Mg} \sin\frac{\pi}{3}} = \frac{60.9796 \text{ Å}^3}{46.4818 \text{ Å}^3} = 1.3119 \tag{3.12}$$

The interest in producing Mg-based materials is motivated by some desirable properties of both the metal and its hydride. $\mathrm{Mg\ is\ abundant\ on\ earth's}$ crust, is inexpensive and, being the 12th element of the periodic table, is light compared to other metals (molar mass $M_{Mg} = 24.305$ g mol^{-1}). The low weight of Mg is the cause of the most appealing property of MgH_2, the high hydrogen capacity. The gravimetric capacity C_G is the ratio between H mass and the total mass:

$$C_G = \frac{m_H}{m_{MgH_2}} = \frac{2M_H}{M_{Mg} + 2M_H} = 7.66 \text{ wt}\% \tag{3.13}$$

where $M_H = 1.008$ g mol^{-1}. The volumetric capacity C_V is defined as the mass of H per unit volume

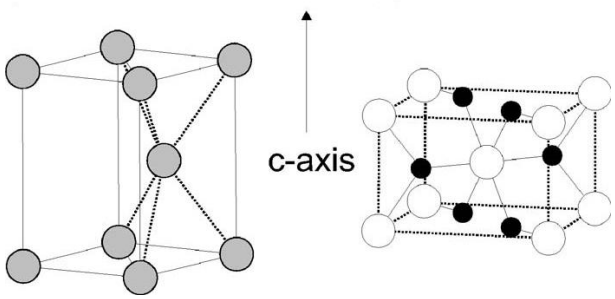

Figure 3.3 On the left, hexagonal close packed (hcp) structure of metallic Mg, space group $P6_3/mmc$; on the right, rutile-type tetragonal structure of MgH_2, space group $P4_2/mnm$. H atom positions are in black.

$$C_V = \frac{m_H}{V_{MgH_2}} = C_G \rho_{MgH_2} = 111 \text{ kg mol}^{-1} \tag{3.14}$$

where $\rho_{MgH_2} = 1450$ kg m^{-3} is MgH_2 density. These are high capacity values, already above the optimistically high targets ($C_G = 5.5$ wt%, $C_V = 40$ kg mol^{-1}) for H storage systems set by the US Department of Energy for the year 2020[13].

However, Mg has two major downsides that prevent its wide implementation as a H-storage material. The first one is the high stability of MgH_2: the enthalpy and entropy of formation of the hydride are[14] $\Delta H = -74.060 \text{ kJ mol}_{\text{H}_2}^{-1}$ and $\Delta S = -133.4 \text{ J K}^{-1} \text{ mol}_{\text{H}_2}^{-1}$ respectively, meaning that desorption conditions require too high temperature or too low H_2 pressure for practical applications. The second downside is the slow diffusion of H atoms in MgH_2. Even if the reaction is thermodynamically favoured, at temperatures below ~ 600 K H-absorptions and (especially) desorptions are blocked by the slow kinetics and heating above 600 K is not desirable in practical applications. Another aspect that has to be dealt with is the volume expansion of a metal to hydride transformation. Equation (3.12) shows that the Mg to MgH_2 reaction involves a 31.19% volume increase, an issue that has to be dealt with at practical application scale, but can also become an opportunity to mechanically induce thermodynamic changes in the hydride as it will be discussed in the following subsection.

Approaches to improve MgH_2 storage properties

With the aim to improve H-sorption kinetics and thermodynamics over bulk Mg, many Mg-based materials have been synthesised following different approaches: alloying with other elements[15], mixing with catalysts such as transition metals[16] or transition metal oxides[17], refining the micro/nanostructure primarily via ball milling[18–20], but also by sputtering[21–23] or chemical precipitation[24].

In nanostructured materials, the high surface-to-volume ratio and the short diffusion paths lead to an enhancement of H-sorption kinetics. Moreover, new interesting phenomena may arise at the nanoscale, such as a reduction of hydride formation enthalpy due to interface energy contribution[21], or due to the effect of elastic boundary conditions[25,26]. These effects could lower the H-desorption temperature at the pressure of 0.1 MPa, one of the main

goals for practical H-storage applications. On the other hand, challenging issues like microstructure coarsening and oxidation arise in nanostructures during H-sorption cycles at elevated temperature.

Among the various catalysts employed to lower the activation energy for H-sorption in Mg-based systems, titanium (Ti) and its hydride TiH_2 have gained considerable attention[18,19]. In fact, Ti is relatively lightweight and abundant, and the resulting kinetics of H-sorption are among the fastest ever observed for Mg-based materials.

The study of the Mg-Ti-H system is an important field of research of this Thesis and will be described thoroughly in Chapter 5.

4 MG-ONLY NANOPARTICLES

4.1 Self-assembly of Mg nanoparticles

Morphological evolution of materials is driven by capillary forces which tend to decrease the total excess free energy by reducing the area and/or the energy per unit area associated with surfaces and interfaces. Well known examples are surface smoothing, surface faceting, grain growth, and the coarsening of a particles ensemble. Coarsening may occur by monomer exchange when small particles, characterised by high mean curvature and solubility according to the Gibbs–Thomson equation, lose the competition for solute in favor of large particles. The mechanism of shrinking and dissolution paralleled by the growth of large particles, generally named Ostwald ripening[27] (OR), can be described by the Lifshitz–Slyozov–Wagner mean-field theory[28,29] and subsequent modifications which account for the effects of nanoscale size[30] and particle shape[31].

Alternatively, morphology evolution may involve the dynamics of building blocks much larger than the simple monomer, such as the aggregation of small particles having a certain degree of mobility possibly followed by their coalescence. In the case of crystalline particles, coalescence may be accompanied by a coordinated particles rotation towards a common crystallographic orientation, which eliminates the inter-particle interface yielding a larger single crystal. In a similar self-organized process, fine grains in a polycrystalline material can achieve the same orientation and eventually grow

removing the grain boundaries. Indeed, the phenomenon of oriented attachment (OA) was observed in colloidal NPs solutions[32] almost at the same time when grain growth by grain-rotation coalescence (GRC) was demonstrated to occur in thin gold films with a columnar structure at relatively low homologous temperature ($T/TM \approx 0.4$)[33]. Since then, both experiments[34] and molecular dynamics simulations have established OA/GRC as important self-organized crystallization mechanisms[35,36].

Clearly, understanding the coarsening mechanisms which rule the morphological evolution of nanoparticles assembled materials is not only relevant for basic materials science but is also a prerequisite for tailoring the growth and controlling the stability of nano-engineered materials.

This Section focuses on the morphology evolution resulting from self-organization of Mg NPs on room temperature substrates synthesised by IGC. The evolution of the NPs size, at the level of single NPs and of their agglomerates, as well as the crystallite growth, is usually ascribed to processes occurring in proximity of the vapour source at elevated temperatures/kinetic energy[37]. The collection on cold substrates at or below room temperature is generally accompanied by an increase of the aggregate size without significant enlargement of the NPs/crystallite size. Even the NPs cold compaction yields bulk nanocrystalline materials with a crystallite size which remains quite close to the original NPs size[38]. In contrast to this widespread behavior, it is showed here that self-assembly of primary Mg NPs provokes a dramatic increase of both NPs and crystallite size with increasing coverage on room temperature substrates. This phenomenon provides a key to understand previous experiments where it was observed that the size of Mg NPs readily reached the micron scale with increasing yield of material[39–41]. In this respect, the ability to limit morphological coarsening is relevant to upscaling the synthesis of Mg-based nanostructures for hydrogen storage applications. It is well established that small NPs exhibit with enhanced kinetics of hydrogen sorption[40]. In addition, it has been predicted that the equilibrium temperature for hydrogen desorption can be lowered by encapsulating small Mg NPs inside a stiff shell, like the one provided by controlled oxidation of the NPs surface[26]. A precise control over the morphology of Mg NPs represents an important step towards the development of a Mg-based nanocomposite with kinetics and thermodynamics features more amenable to practical hydrogen storage applications.

Emphasis is given to the mechanisms and parameters that are of general relevance in the self-organization and coarsening of other NPs materials with common characteristic.

Synthesis conditions

The main synthesis chamber was set up for deposition of Mg NPs on substrates, using Mg ingots (99.9% purity) as precursor material. The He flow was adjusted to 65 std cm^3 min^{-1}, keeping the pressure constant at 270 Pa. Super-smooth silicon substrates (Agar Scientific, dimensions 5×5×0.5 mm^3, surface finish roughness <1 nm, crystallographic orientation (111)) and TEM grids coated by a holey carbon film were fixed on the cylinder kept at room temperature at a distance of about 150 mm from the thermal source. Using a thin K thermocouple, it was checked that the substrates also remained at room temperature during the evaporation. During one deposition experiment, NPs were also collected on a quartz single crystal specially cut to contribute zero background to XRD measurements.

In order to study the morphology evolution, different substrates were exposed to the incoming aerosol in sequence and for increasing time, by rotating the cylinder while keeping the evaporation rate constant. After the deposition, the chamber was evacuated and pure O_2 was admitted very slowly up to a pressure of 270 Pa, in order to form a MgO layer which prevents the specimens from ignition and severe oxidation upon air exposure. Finally, the chamber was vented and the specimens were stored in a glove box under argon atmosphere prior to electron microscopy observations.

TEM methods

In addition to the SEM observations of NPs deposited on silicon substrates, complementary TEM methods were used to investigate the NPs deposited on the TEM grids. In collaboration with EMAT - University of antwerp, a FEI Titan microscope operating at 300 kV and 120 kV was used to perform HAADF-STEM, HR-TEM and electron energy loss spectroscopy (EELS) mapping. Additionally, energy filtered TEM (EFTEM) imaging was performed using a Philips CM30 electron microscope operating at 300 kV. HAADF-STEM and HR-TEM imaging provide information on the

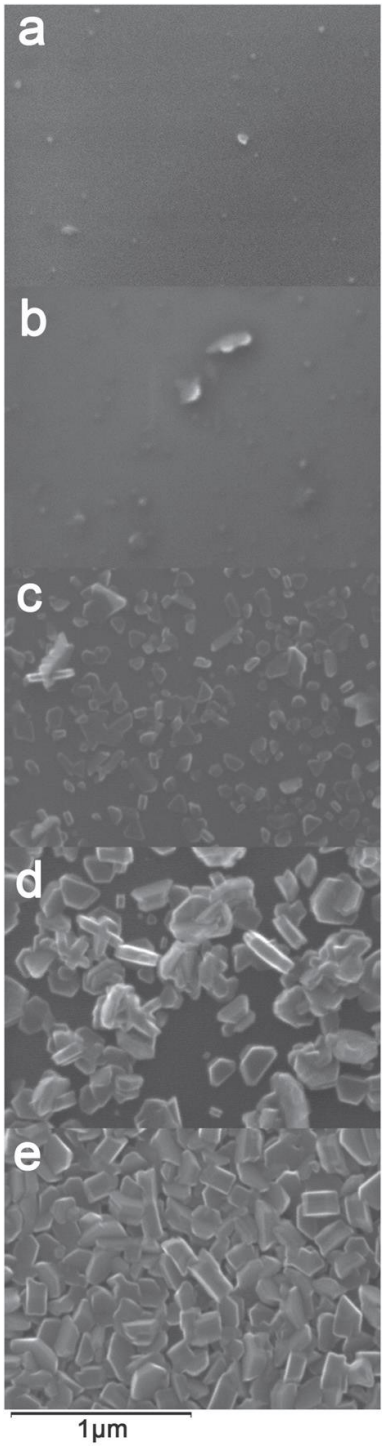

Figure 4.1 SEM images representing the morphological evolution ofMgNPs on Si substrates at room temperature. The only difference between the specimens is the increasing deposition time: (a) 30 s; (b) 60 s; (c) 120 s; (d) 300 s; (e) 600 s.

morphology and atomic structure of the NPs, including the orientation of the facets. EELS and EFTEM mapping provide chemical information, which allows insight into the distribution of the various elements within the sample. The results were not dependent on the electron energy and the specimens did not change with time from the beginning of the observation. Also, no signs of evaporation or displacement of material were ever detected, ensuring that electron beam did not influence the observed morphology.

Characterisation

The morphology evolution of gas-phase condensed Mg NPs with increasing deposition time is illustrated in Figure 4.1, where the NPs assemblies obtained after 30, 60, 120, 300 and 600 s are displayed. A parallel increase in substrate area coverage and average NPs size is observed, as summarised in Figure 4.2. The NPs size is defined from here on as the diameter of the circle inscribed in the NPs as they appear in the electron microscopy image. The

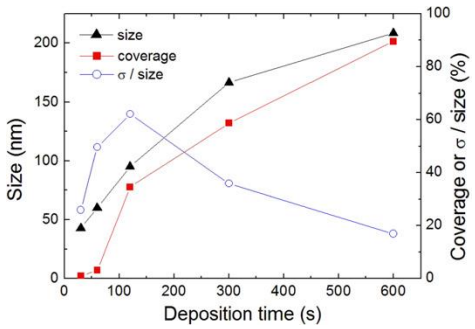

Figure 4.2 Average NPsize and substrate area coverage as a function of the deposition time, derived from analysis of the image sequence in Figure 4.1. The standard deviation σ of the NPs' size distribution is also plotted as a percentage of the average size.

coverage is defined as the percentage of substrate area which is coated by Mg NPs, independently on the local thickness of the deposited material. At early deposition times (Figure 4.1a) the observed NPs are rather small, in the 30–50 nm range, with mutual separation distance much larger than the NPs size. Following this individual NPs stage, larger particles begin to appear (Figure 4.1b), originating from the aggregation/coalescence of the smaller ones. With still increasing coverage (>30%, Figure 4.1c and Figure 4.3), NPs in the 100–200 nm range

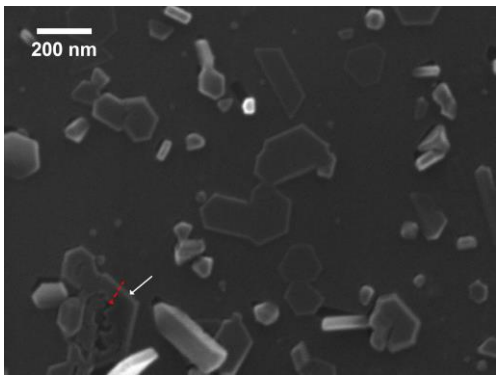

Figure 4.3 intermediate stage of the morphological evolution of Mg NPs on silicon substrate, for a coverage similar to Figure 4.1c. The white solid arrow indicates a large NP "under construction" whose surface is partly constituted by planar facets. The dashed red arrow highlights an example of imperfect attachment of NPs building blocks. Several small NPs with size in the 20-50 nm range are still visible.

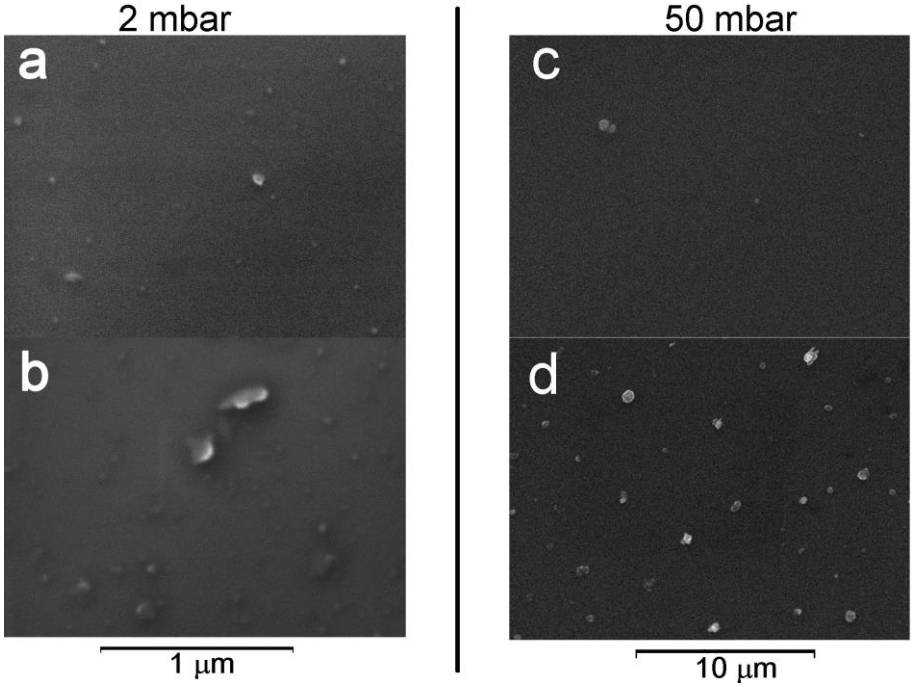

Figure 4.4 SEM images of gas-phase condensed Mg NPs deposited on silicon substrates at two different helium pressures: p_{He}=2 mbar (left column) and p_{He}= 50 mbar (right column). To be noticed the different magnifications of the left and right column. Images a) and b) are the same as in Figure 4.1a and b. In the deposition at high pressure p_{He}= 50 mbar, NPs with size of several hundreds of nm were detected even at the early deposition stages and very low coverage, as shown in c). On the contrary, NPs smaller than 50 nm, rather abundant at p_{He}=2 mbar, were not observed also at higher magnification. With increasing time and coverage, the NPs size distribution at p_{He}= 50 mbar was not seen to evolve significantly. The average NP size in d) is 340 ± 120 nm and the coverage is 1%. The much larger NPs size at the higher p_{He} value for similar (low) substrate coverage is a clear indication that NPs are formed and grow in the gas phase along the fly path between the vapour source and the collection substrate.

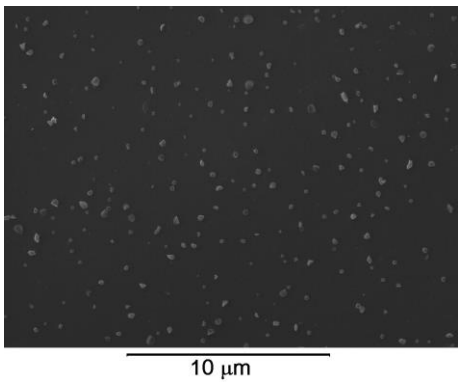

Figure 4.5 SEM image showing the influence of source power (i.e. evaporation rate) on Mg NPs morphology. In comparison with Figure 4.1, these Mg NPs were deposited at a source power higher by 20 %, resulting in a 4-fold increase of the deposition rate. Under these conditions, significantly larger NPs were obtained (the average size is 150 ± 80 nm) even at low substrate coverage (3% in this image, similar to Figure 4.1b), providing further indication of NPs formation and growth in the gas phase.

with faceted shape become the dominant feature of the distribution, although small NPs are still detected with significant frequency. At this point, the relative width of the NPs size distribution, defined as its standard deviation σ divided by the average size, exhibits a maximum value close to 60% (Figure 4.2). Noteworthy is the presence of many particles 'under construction', such as the one marked by the white arrow in Figure 4.3, which show regular planar facets as well as irregular surfaces resulting from the coalescence of smaller building blocks. In some cases, the geometrical matching between such blocks is imperfect and small voids are left behind (dashed red arrows in Figure 4.3). Finally, the frequency of small NPs decreases significantly and a narrower distribution of NPs with faceted shape develops at high coverage (>75%, Figure 4.1d and e).

The average NPs size increases significantly with augmenting He pressure or evaporation power (see Figure 4.4 and Figure 4.5), providing clear indication that NPs are formed in the gas phase. Clearly, this dependence of the NPs size distribution on the deposition parameters is more evident during the early deposition stages, i.e. at low substrate coverage before the occurrence of significant coalescence on the substrate. For the sake of comparison, Mg deposition on silicon was also carried out under high vacuum (10^{-6} mbar) keeping the same deposition rate and times as in Figure 4.1: in this case, uniform-coverage Mg films were obtained, which did not exhibit any morphological contrast during SEM observations.

The coverage and the amount of deposited material are strongly influenced by the nature of the substrate: Figure 4.6 compares the NPs distribution observed on a silicon substrate (Figure 4.6a, SEM image) and on a holey carbon TEM grid (Figure 4.6b, HAADF-STEM image) obtained after the same deposition. The comparison between the two images suggests that the sticking probability of the incoming NPs is lower on the holey carbon TEM grid, yielding a lower coverage (17% versus 60%) and a rather small NPs

average size (25 ± 11 nm). The NPs size distribution derived from the analysis of Figure 4.6b is reported in Figure 4.7. On account of the excellent resolution of the HAADF-STEM image and neglecting coalescence phenomena at low coverage, we suggest that Figure 4.7 represents well the NPs size distribution in the gas phase prior to deposition.

The inset of Figure 4.6a depicts the XRD profile measured on the corresponding NPs specimen deposited on single-crystal quartz. This profile should be taken as representative of NPs on Si only, since SEM indicates that coverage, size distribution and morphology are very similar on silicon, glass and quartz substrates (see Figure 4.8). The relative intensities of the three Bragg peaks characteristic of hcp Mg: (100), (002) and (101) clearly reveal a preferential orientation of the NPs with the (001) basal plane parallel to the substrate. The (002) Bragg

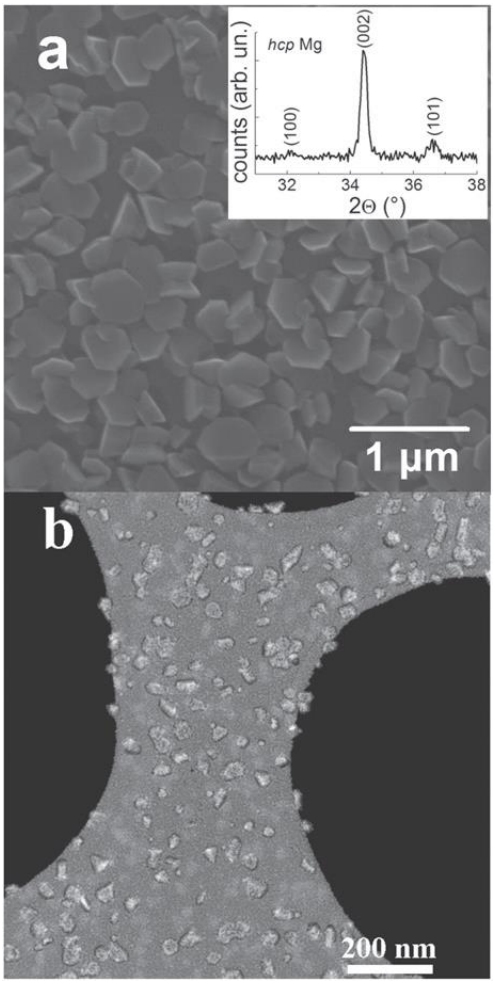

Figure 4.6 Influence of the deposition substrate on coverage and NPs morphology. (a) SEM image of Mg NPs on Si substrate (60% coverage). The inset displays the XRD profile of the corresponding specimen deposited on quartz, having similar morphology according to SEM (Figure 4.8); (b) HAADF-STEM image of Mg NPs on holey carbon TEM grid (17% coverage).

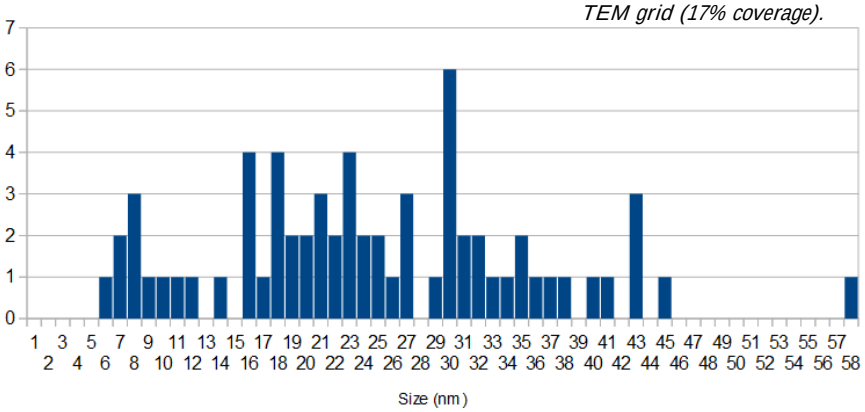

Figure 4.7 Mg NPs size distribution (NPs counts) obtained from the analysis of Figure 4.6b. The resulting average size is 25 ±11 nm.

peak is quite narrow, making it difficult to obtain a precise estimate of the crystallite size. Nevertheless, taking into account the instrumental resolution, from the (002) Bragg peak width it can be concluded that, for NPs on silicon/quartz and at high coverage, the average crystallite size along the [001] direction is larger than 100 nm. The HAADF-STEM picture of Figure 4.6b and Figure 4.7 also highlight the presence of very small NPs with size in the 5–10 nm range. The frequency of these small NPs decreases significantly with increasing deposition time and coverage, and a coarsening of the NPs distribution takes place on the TEM grids as well, as shown by Figure 4.9a corresponding to a coverage of 75%. However, NPs assemble on the TEM grids yielding preferentially elongated or ramified structures, in comparison to the larger NPs with hexagonal shape mainly observed on silicon substrates. The influence of the substrate on the NPs morphology is a clear proof that coarsening processes indeed occur on the substrate at room temperature.

A thin oxygen-rich layer is observed only around the surface of the NPs assembly (O signal in Figure 4.9b). The fast Fourier transform (FFT) of HRTEM images of this external layer (Figure 4.10a, b) permits one to identify it with cubic MgO, as expected

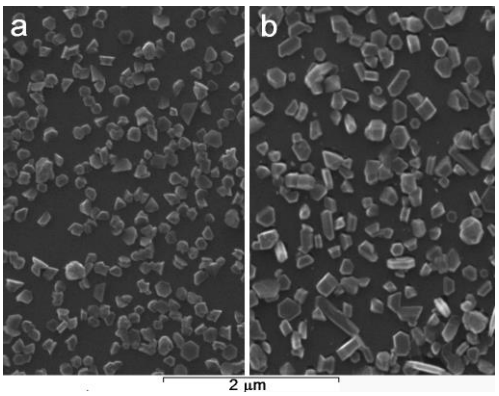

Figure 4.8 SEM images of Mg NPs deposited on quartz (a) and silicon (b), showing the similarity of NPs size and morphology on these two substrates.

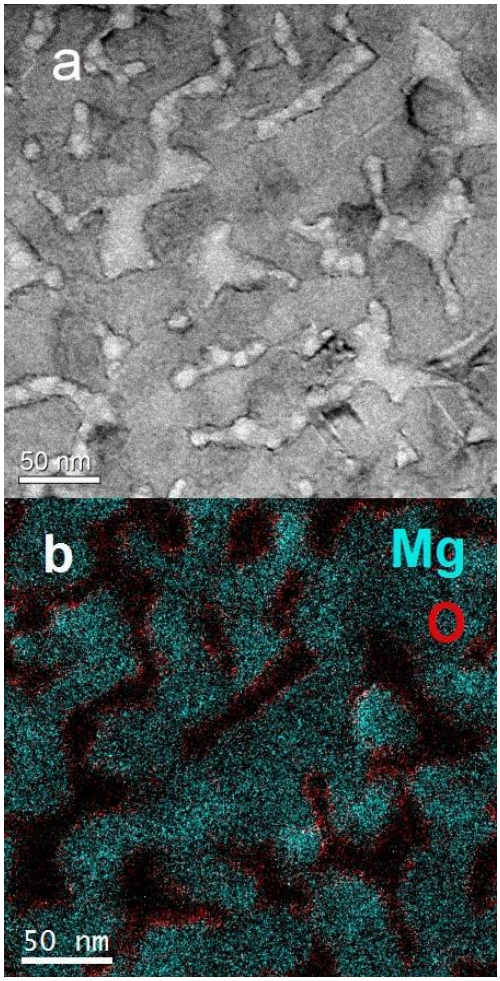

Figure 4.9 (a)TEM image of Mg NPs ensembles deposited on aTEM grid and (b) EFTEM mapping of Mg and O distribution in the same region. The coverage amounts to 75%.

and in agreement with previous observations[40,42]. It is worth noting that the O distribution map in Figure 4.9b reveals no internal oxidation, suggesting that dense interfaces are formed through metal–metal contact during NPs coalescence and that an overall core–shell Mg–MgO morphology develops after exposure to oxygen at the end of the deposition. It seems reasonable to assume that this oxide distribution, where external surfaces are coated by a 4–5 nm thick oxide layer whereas internal interfaces are oxide-free, applies also to NPs grown by coalescence on silicon substrates. NPs oxidation is sometimes coupled to the appearance of nano-voids, the size of which can reach tens of nm, as shown by the HAADF image in Figure 4.11. The EELS map of one such void (inset of Figure 4.11) confirms the presence of a continuous oxide shell and of a partly hollow Mg core.

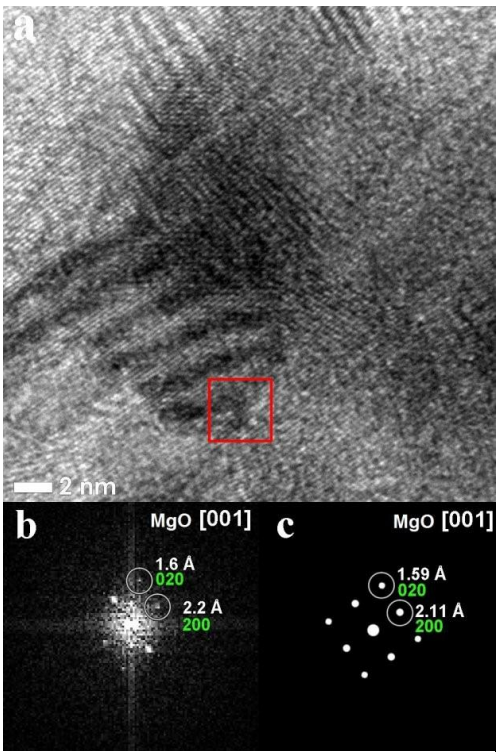

Figure 4.10 (a) HRTEM image of a NP, including the O-rich shell region; (b) FFT pattern of the area inside the red frame in (a); (c) simulated electron diffraction pattern along the [001] zone axis of cubic MgO.

HRTEM was also employed to investigate the crystalline domains in the Mg cores, as reported for the NP in Figure 4.12a. The corresponding FFT pattern (Figure 4.12b), which matches the diffraction pattern along the [001] zone axis of hcp Mg (Figure 4.12c), remains unchanged when different portions of the NP are selected, proving its single-crystal nature. Differently, elongated and ramified structures are usually constituted by two or more crystals. Figure 4.13 displays an HRTEM image of a triple junction between NPs: the corresponding FFT patterns (shown on the right) permit identifying the relevant zone axes proving that the NPs have different crystallographic orientation. The HRTEM crystallographic analysis reveals a preferential orientation with the NPs' hexagonal (001) basal plane parallel to the substrate. In general, the crystallite size is significantly larger than the size of the smaller NPs observed at the early deposition stage, indicating the

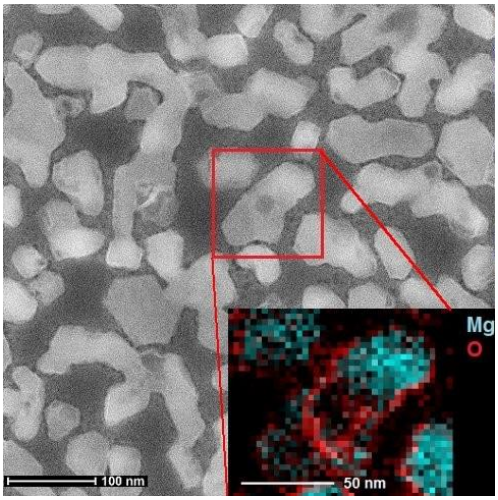

Figure 4.11 HAADF-STEM image showing the formation of nanovoids in Mg NPs assemblies. The inset is a EELS mapping of the framed area, demonstrating the presence of a partly hollow Mg core inside the MgO shell.

occurrence of a recrystallization mechanism upon aggregation and coalescence, in agreement with XRD.

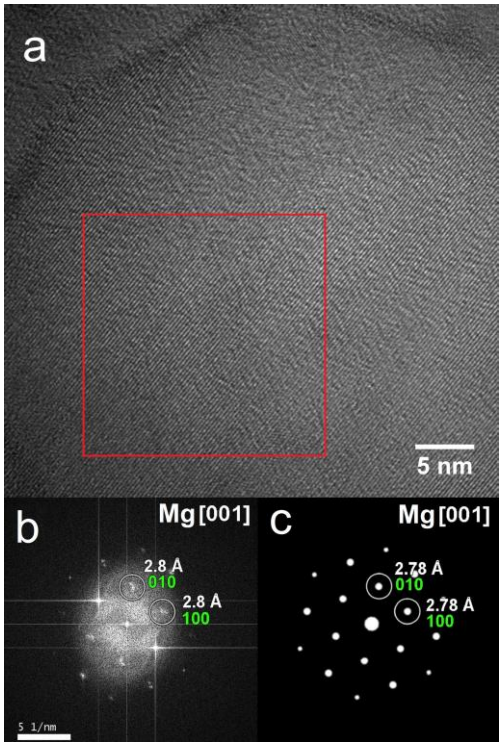

Figure 4.12 (a) HRTEM image of a Mg NP; (b) FFT of the framed area and (c) simulated electron diffraction pattern for hcp Mg along the [001] zone axis. The FFT pattern remains unchanged when different portion of theNP are selected proving its single-crystal nature.

Discussion

The evolution of NPs morphology clearly demonstrates that a significant coarsening of the NPs size distribution takes place on the room temperature substrate, far away from the hot crucible. The thermodynamic driving force for this process is the reduction of the total surface/interface free energy of the NPs ensemble. We will now discuss our results with reference to the two mechanisms presented in the introduction: OR versus OA/GRC, with the aim to identify the one responsible for the observed behaviour.

In the OR process, larger NPs grow at the expenses of smaller ones, the last having larger averaged mean curvature k_γ and hence higher vapor pressure according to the Gibbs-Thomson equation[8]:

$$P(k_\gamma) = P_0 e^{\left(\frac{\Omega k_\gamma}{k_B T}\right)} \tag{4.1}$$

where $P_0(T)$ is the vapour pressure at temperature T and zero curvature, Ω is the atomic volume and k_B is Boltzmann's constant. The exact vapour pressure resulting from the Gibbs–Thomson equation should be calculated

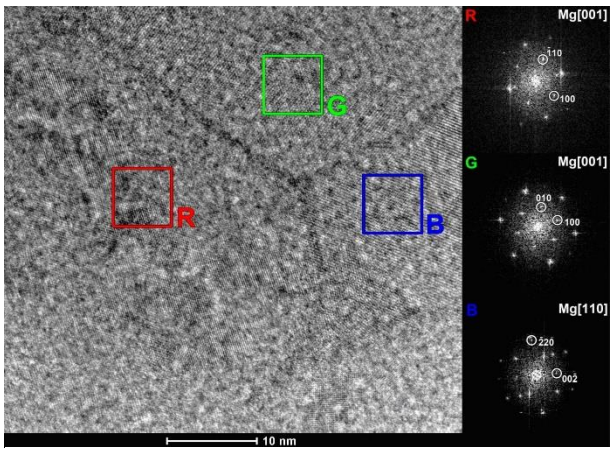

Figure 4.13 HRTEM image of a triple junction between NPs; on the right the FFT diagrams and the zone axis corresponding to the framed areas R, G, B are shown.

taking into account the real NP shape, as observed experimentally or as derived from the Wulff's construction[43]. It is anyhow simple to estimate the resulting correction by taking the simplified formula for isotropic surface energy γ and spherical NPs of radius *r*:

$$P\ r\ = P_0\ T\ e^{\left(\frac{2\Omega\gamma}{rk_BT}\right)} \equiv P_0\ T\ f\ r,T \tag{4.2}$$

using $\gamma = 0.52$ Jm^{-2} (as calculated for Mg (001) surface in [43]), $\Omega = m_A/\rho = 2.32 \cdot 10^{-29}$ m^3, one gets $f(r = 5\ \mathrm{nm}, 300\ \mathrm{K}) \approx 3.2$. In order to assess whether OR is effective in our NPs ensemble, we need to estimate if appreciable Mg evaporation occurs during the deposition. The time scale for evaporation of one Mg layer with thickness *t* from the outer NP surface is given by

$$\tau_{ev} = t\rho/M \tag{4.3}$$

where ρ is the mass density and M is the rate of mass evaporation per unit area, that can be calculated by the Langmuir equation

$$M = P\sqrt{\frac{m_A}{2\pi k_B T}} \tag{4.4}$$

m_A being the atomic mass. Using literature values for $P_0(T)$[44], and taking $t = 1$ nm, we obtain $\tau_{ev} \approx 10^{11}$ s at 300 K. This order-of-magnitude estimate safely rules out any possibility that the observed coarsening can be

related to OR mediated by evaporation and atomic transport in the vapour phase.

In addition, the particle shapes highlighted in Figure 4.3, showing an intermediate stage in the build-up of larger particles, clearly suggest the involvement of building-blocks with a typical size <30 nm, and the substrate dependent morphological evolution indicates that the dynamics of such blocks is influenced by their interaction with the substrate. This leads us to consider the second coarsening mechanism by NPs aggregation and coalescence, which, in a first step, requires that two or more NPs get in contact. In the present experimental setup, this occurs when an incoming NP transported by the inert gas flow impinges on already deposited NPs. The observation that the coverage increases faster than linearly in the first deposition stages ($t \leq 120$ s in Figure 4.2) indeed suggests that the sticking probability on already deposited NPs is higher than on the bare substrate. At the same time, random walk of the NPs on the substrate may also contribute to their aggregation. Indeed, while epitaxial clusters larger than the dimer are essentially immobile on substrates, the diffusion of NPs as a single entity has been demonstrated for Sb NPs (5 nm diameter) on graphite[45]: the resulting formation of ramified island and the main features of the aggregation dynamics were described satisfactorily by the diffusion–deposition–aggregation (DDA) model[46], and a NP diffusion coefficient $D = D_0\ e^{-E/k_B T}$ was determined. The pre-exponential factor D_0 decreased with increasing number of atoms in the NPs according to a power law, suggesting that this mechanism deactivates quickly with increasing NPs size[46]. Although NPs mobility may be enhanced in our set-up by small mechanical vibrations stimulated by the incoming helium flow, it is likely that only the smaller NPs, *i.e.* the ones with size in the 5–10 nm range, are able to move on the surface and to aggregate with each other or with larger NPs. Furthermore, the mobility of the NPs is expected to decrease significantly with increasing substrate roughness and density of surface defects, as demonstrated using ion-irradiated surfaces[47]. Therefore, the larger NPs size observed on silicon with respect to holey carbon film can be understood under the reasonable assumption that NPs mobility is enhanced on the super-smooth substrate. In summary, both direct impingement and Brownian motion may contribute to NPs aggregation, the latter rapidly losing relevance with increasing NPs size above 10 nm.

While the ramified structures formed on the holey carbon film seem consistent with the DDA model, one remarkable difference observed here is the occurrence of crystal growth in parallel with NPs aggregation. With increasing coverage, we highlight the formation of isolated single-crystal NPs as well as NPs interconnected in a ramified structure, the crystal size of which is significantly larger than the typical NPs size observed at low coverage. This feature strongly supports the occurrence of NPs self-assembly via OA/GRC, with the consequent elimination of their common grain boundary (GB) and formation of a full-density crystal. The theoretical modelling of GRC was proposed already by Harris *et al.*[33] and further developed by Moldovan *et al.*[48,49]. Essentially, grain rotation is a viscous process—in analogy to GB migration—where the grain angular velocity is proportional to the torque via a "rotational $\mathrm{mobility}$" $M(d) \propto d^{-p}$ with d the NP's diameter, and $p = 5$ or 4 for accommodation by GB diffusion or lattice diffusion, respectively[48]. For nearly spherical NPs, such as those reported in [34], the initial contact area is almost independent on the relative crystallographic orientation and the torque acting on the NPs arises solely from the anisotropy of the interfacial free energy. Differently, for our faceted NPs, the maximization of the contact area provides a further driving force for the rotation. Let us consider for simplicity the lateral contact between two Mg NPs having the shape of a hexagonal prism with the base parallel to the (001) plane. Assuming that the six lateral surfaces belong to the {100} family, any rotation which brings two such surfaces in contact, accompanied by short range displacement accommodation of the two lattices, results in a new single crystal. The free energy released by this process amounts to twice the surface free energy γ. According to ab initio calculations[50], $\gamma \approx 0.055$ eV Å^{-2} for Mg {100} surfaces. If this energy is initially taken up as heat by a material slice of thickness δ, the sudden temperature variation can be roughly estimated as

$$\Delta T \approx \frac{2\gamma\Omega}{3k_B\delta} \tag{4.5}$$

yielding $\Delta T \approx 200$ K for $\delta = 5$ nm. This temperature increase, coupled to the relatively low melting point of Mg ($T/T_M \approx 0.33$ at room temperature), permits additional accommodation via lattice and/or surface diffusion, favouring the formation of fully dense, single crystal NPs via self-organized OA of NPs with different shape and size.

Due to the strong dependence of NPs translational and rotational mobility on size, NPs/substrate interaction and substrate roughness, self-assembly via OA/GRC progressively lose importance as NPs get larger and/or NPs/substrate adhesion increases. When OA/GRC becomes inactive, the coalescence between two or more NPs, instead of producing larger single crystals, generates oxide-free GB-like interfaces, as shown in Figure 4.13 for the three NPs with different crystallographic orientations. The transition to this behaviour occurs at a lower average NPs size in holey carbon film with respect to silicon, likely due to a lower rotational and translational NPs mobility, as previously discussed.

The observed formation of nano-voids is in agreement with previous electron microscopy observations[42] and can be attributed to the nanoscale Kirkendall effect[51], *i.e.* to an inward flow of Mg vacancies which compensates the faster diffusion of Mg^{2+} cations with respect to O^{2-} anions across the developing MgO shell during oxidation. This process clearly does not affect the morphological evolution of the NPs during the deposition experiments but may contribute to the final microstructure when the NPs are exposed to reactive atmospheres.

Conclusions

Mg NPs deposited from the gas phase exhibit significant coarsening phenomena on room temperature substrates. With increasing substrate coverage, it is observed that the average NPs size increases, the small-particle tail of the distribution disappears and large NPs with faceted shape develop. This process is accompanied by crystal growth, yielding NPs with single-crystal character through the coordinated assembly of smaller NPs units the typical size of which is in the 10–50 nm range. These features point to self-assembly via GRC/OA as the mechanism responsible for the morphological evolution. The degree of NPs translational mobility is also relevant to the overall coarsening and appears enhanced on smooth substrates.

The key ingredients to the NPs self-organization can be summarized as:

i. the anisotropic shape of the primary NPs, which provides a strong driving force for the rotation and matching of crystallographic orientation upon contact;

ii. the high value of the free energies of specific crystallographic surfaces, which favours their elimination by oriented attachment inducing a large temperature increase;
iii. the low melting point of the NPs material, which permits additional accommodation via lattice/surface diffusion due to the relatively high homologous temperature;
iv. the realization of a clean atmosphere which prevents oxidation and allows for metal/metal contact;
v. the NPs translational and rotational mobility, depending on substrate-particle adhesion and therefore on substrate roughness and substrate–particle chemical interactions.

By tuning these parameters, self-assembly and coarsening may be either enhanced or inhibited. As long as the amount of deposited material is low, *i.e.* below 100% coverage, coarsening may be avoided simply by reducing NPs mobility, for instance using rough substrates and/or lowering the substrate temperature. However, in order to upscale the synthesis of small Mg NPs it appears necessary to prevent coalescence and oriented attachment also when two NPs eventually get in contact. On the basis of the present results, it is suggested that this may be achieved by controlled modification of the NPs surface prior to deposition, for instance by exposure to a reactive gas (such as O_2 or H_2) which forms a shell around the NPs to prevent metal/metal contact. Alternatively, co-deposition of a second phase may be employed to prepare a nanocomposite. Experiments in this direction will be the subject of the next sections.

4.2 Mg-MgO nanoparticles

Reactive condensation with O_2

In this section is given a demonstration of reactive gas condensation of NPs using O_2.

The main chamber was set-up for massive nanopowder collection. Mg ingots (99.9% purity) were heated under a He flow rate $\Phi_{He} = 65\ \mathrm{ml_n min^{-1}}$, keeping the atmosphere in the chamber constant at 270 Pa. As soon as Mg starts to evaporate, the oxygen gas line is opened and O_2 starts to flow directed towards the cylinder as showed in Figure 2.6. Controlling the opening of the needle valve and the pressure in the gas line, the flow rate was set to $\Phi_{O_2} = 2\ \mathrm{ml_n min^{-1}}$. This value of Φ_{O_2}, converted in atoms s^{-1}, was chosen to be safely smaller than the Mg evaporation rate; in this way, all the O_2 is consumed by the evaporated Mg, avoiding the oxidation of the W crucible or of the Mg ingots that would halt the experiment. At the end of

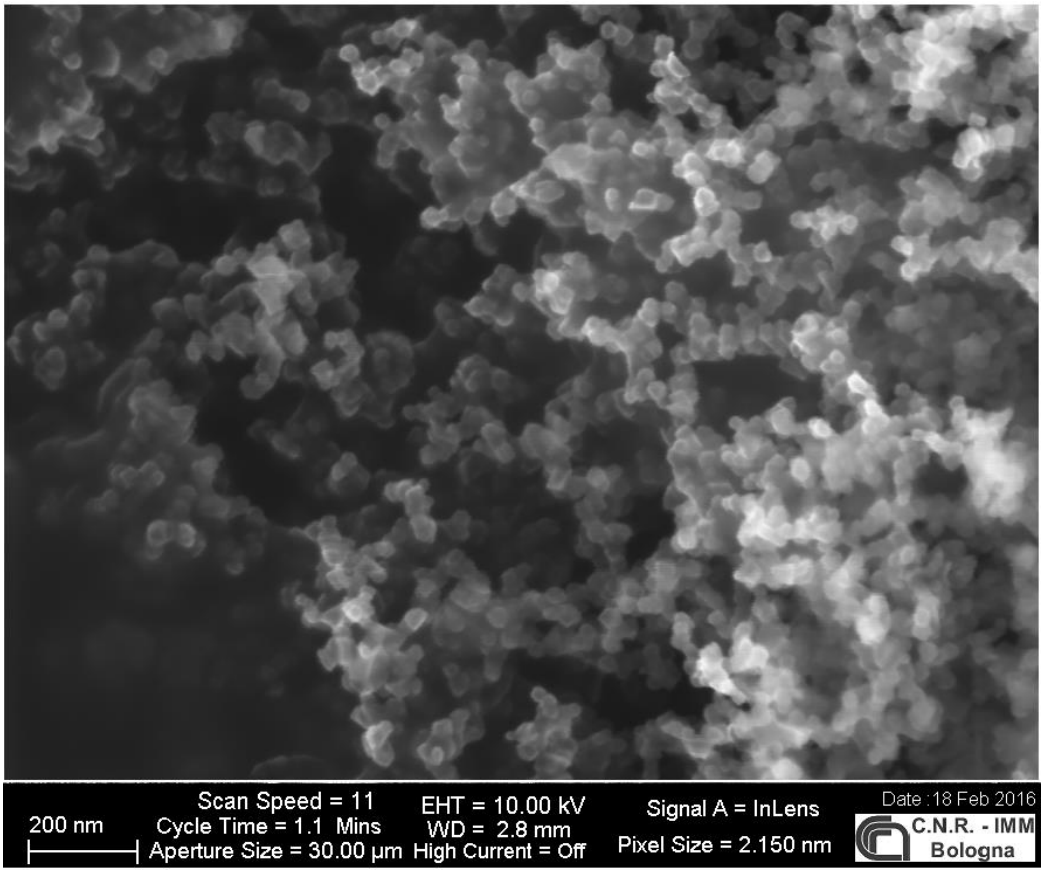

Figure 4.14 FE-SEM image of Mg NPs synthesised reactive (O_2) gas condensation.

the evaporation, the chamber was slowly vented and the sample was collected in air.

Characterisation

A FE-SEM image of the RGC synthesised Mg NPs is showed in in Figure 4.14. The effects of the oxidising atmosphere on the morphology are evident comparing the nanopowder in Figure 4.14 with the thick film, considerable as a nanopowder, of IGC synthesised Mg NPs (Figure 4.1e). The NP size is in the 20-30 nm, a ten-fold reduction with respect to the IGC case and the hexagonally-faceted shape is not observed anymore.

Rietveld refinement of XRD data in Figure 4.15 permits a more quantitative discussion. Metallic Mg and MgO phases were detected with fractions 52±1 wt% and 48±1 wt%, respectively. This means that 64% of the Mg atoms were oxidised. No unit cell modifications nor microstrain were observed. The mean crystallite size d has been extrapolated for both phases: $d_{Mg} = 24 \pm 3$ nm for Mg and $d_{MgO} = 4.4 \pm 0.7$ nm for MgO. The agreement of d_{Mg} with the NP size observed by FE-SEM (in Figure 4.14) suggests that the NPs are Mg single crystals; the small crystallite size of MgO can then be interpreted as the thickness of the MgO shell surrounding the Mg core. The shell to core weight ratio can be calculated with

$$\frac{m_{shell}}{m_{core}} = \frac{\rho_{shell}[\ 2d_{shell} + d_{core}\ ^3 - d_{core}^3]}{\rho_{core} d_{core}^3} \tag{4.6}$$

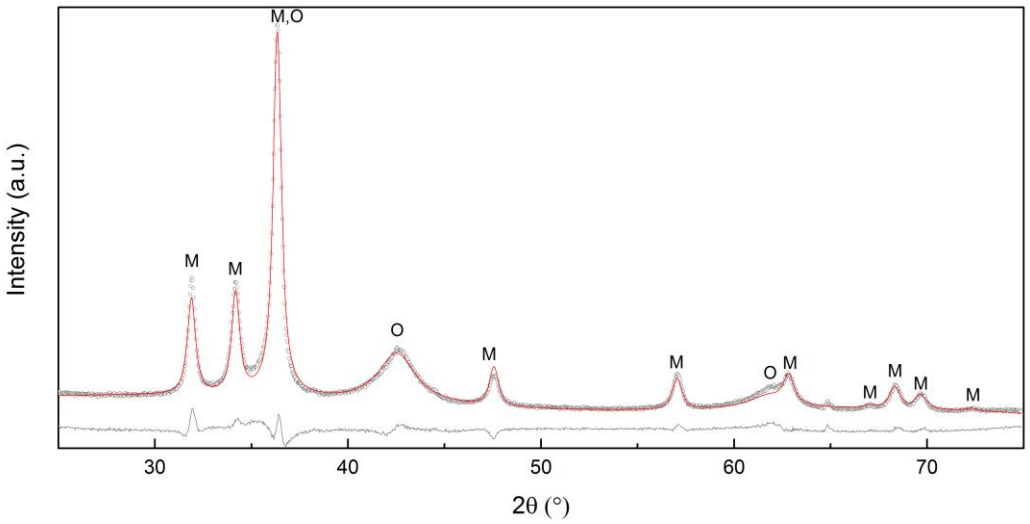

Figure 4.15 XRD pattern of the RGC synthesised Mg sample; the red line superimposed to the data (open circles) is the result of the Rietveld refinement, the grey line below is the residual difference between experiment and calculation. The peaks belonging to the Mg or MgO phase are marked as M or O, respectively.

where $d_{core} = d_{Mg}$, $d_{shell} = d_{MgO}$, $\rho_{shell} = 3.58$ g cm^{-3} is the MgO density, $\rho_{core} = 1.74$ g cm^{-3} is the Mg density[52]. This simple but shape-independent model gives a $\frac{m_{shell}}{m_{core}}$ that overestimates ~3 times the MgO/Mg weight ratio experimentally observed by XRD. This calculation assumes isolated NPs, but when NPs impinge and stick, they share the same MgO layer and the actual shell thickness per each NP is therefore halved. Then, considering $d_{shell} = d_{MgO}/2$ in Equation (4.6), the estimated shell to core ratio is in agreement with the observation, concluding that the NPs synthesised have indeed a Mg core surrounded by a MgO (shared) shell.

Final comments

The size of the RGC synthesised Mg-MgO NPs corresponds to the smaller units observed in the IGC case in the previous section. The crystalline disorder introduced by the formation of the MgO phase, completely blocks the crystal growth phenomenon observed in pure Mg NPs. The results presented here for Mg can be easily extended to other metals or other multi-elemental systems that suffer from sever grain growth, turning RGC an effective technique for the synthesis of small NPs where also "classic" IGC fails.

In principle, adjusting the O_2 flow with respect to the He flow and the evaporation rate it should be possible to synthesise NPs with an oxide shell of controlled thickness. It has to be noted that also geometric factors are critical, like the position of the O_2 inlet (close to the source or to the collection site).

5 MG-TI NANOPARTICLES

An important part of the work presented in this Thesis is the research on Mg-Ti nanoparticles for hydrogen storage. This choice is motivated, as already written at the end of Section 3.2, by the interest on improving Mg H-storing properties and the excellent catalytic properties of Ti[18,19]. In order to achieve a fine dispersion of Ti in Mg, or the formation of a Mg–Ti solid solution, non-equilibrium synthesis techniques are required because Mg and Ti are almost immiscible. Given this picture, Inert and Reactive Gas Condensation prove to be the right techniques to force the coexistence of Ti and Mg at the nanoscale while the nanoparticulate morphology assures a high surface-to-volume ratio beneficial for improving sorption kinetics.

Some nanostructured Mg–Ti systems have already been synthesised primarily via ball-milling[18–20,53,54], but also by sputtering[21–23] or by chemical precipitation[24]. The growth of Mg–Ti nanoparticles (NPs) from the gas phase was carried out by spark discharge generation using Ti and Mg electrodes[55] and by sputtering of a composite Mg–Ti target[56].

In the next Sections are demonstrated the growth, structure, composition and H-storage performances of Mg–Ti nanoparticles by Inert or Reactive Gas Condensation, in the form of compacted pellets or nanopowders.

5.1 Mg-Ti nano-pellets

Synthesis conditions

Mg–Ti samples were synthesised in nanopowder collection mode. Mg ingots (99.9% purity) and Ti powder (Alfa Aesar 99.9% purity, 150 mesh) were used as starting materials. In the IGC chamber, Mg and Ti were evaporated simultaneously in two different crucibles, disposed so that the He flow hits first the Mg vapour source and then the hotter Ti vapour source. The He flow rate was set to Φ= 7 std cm^3 min^{-1} and the pressure was kept constant at P_{He}=270 Pa. Samples with different Ti contents were synthesised by changing the power applied to the Ti-boat.

After the collection on the cylinder, the nanopowder was transfered in the secondary chamber and compacted by the piston for 30 s under a pressure of 400 MPa into a pellet (mass between 12 mg and 40 mg). One subset of the samples was subjected to H-absorption in the secondary chamber, for 3 h at 150 °C under a H_2 pressure of 0.0133 MPa before compaction. Such a pressure was selected to ensure full sample hydrogenation (*i.e.* it is higher than the equilibrium pressures of MgH_2 and TiH_2 at 150 °C). After compaction, O_2 was admitted slowly before venting the chamber, in order to form a passivating oxide layer which prevents the specimens from ignition and severe oxidation upon air exposure. The samples were finally extracted from the chamber and transferred to the equipment for structural analysis and measurement of H-sorption properties under atmospheric conditions.

Seven Mg–Ti samples were synthesised: four compacted in the as-grown state, named MgTi6, MgTi10, MgTi12, and MgTi15 (first subset) and three compacted after in situ H-absorption, named MgTi9H, MgTi12H, and MgTi22H (second subset). The number in each name represents the measured Ti atomic percentage (considering only Mg and Ti elements). In the following, the first and second subsets will be referred to as MgTi# and MgTi#H, respectively. In addition, one sample without Ti was synthesised under the same conditions as reference.

Alongside the usual SEM, EDX and XRD for structural characterisation, TEM-EDX mapping and High Angle Annular Dark Field Scanning TEM (HAADF-STEM) observations were conducted on Mg–Ti NPs directly deposited on a holey carbon grid, using a FEI Titan microscope in collaboration with EMAT - University of Antwerp.

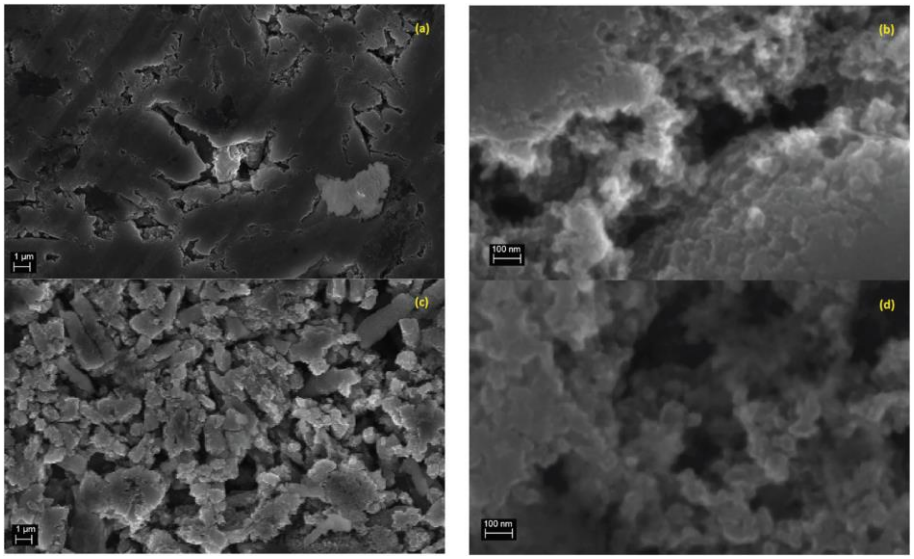

Figure 5.1 FE-SEM images showing the typical morphology of the as prepared MgTi# and MgTi#H pellets. (a and b) Sample MgTi15; (c and d) sampleMgTi22H. The higher magnification images in (b and d) were taken in the proximity of surface cracks.

The hydrogen sorption properties were studied using a Sensys Evo High-Pressure Differential Scanning Calorimeter (HPDSC) from ICMPE - CNRS, Thiais, France. The samples were cycled between 200 °C and 410 °C at a heating rate of 5 °C min^{-1} under H_2 pressures of 0.2 Mpa and 0.4 MPa. The kinetics were measured in the Sievert apparatus at 300 °C under conditions far from equilibrium, starting from 0.9 MPa for H-absorption and 0.015 MPa for H-desorption.

Results

Structure and morphology

SEM images in Figure 5.1 show the typical morphology of both MgTi# and MgTi#H as prepared pellets. Figure 5.1a shows that the surface of MgTi# pellets has flat and uniform regions whose size is around 5–10 mm, meaning that the original morphology of the NPs at the surface is distorted by compaction. Many micrometric cracks on the surface reveal more clearly the presence of NPs inside the pellet with a typical size <20 nm (Figure 5.1b). The picture is different for the as prepared MgTi#H samples, where the surface seems to be more porous and the typical extent of the flat regions does not exceed 1 mm (Figure 5.1c). By FE-SEM resolution, no differences at the nanoscale morphology are observed in the investigated composition range (6–22 at% Ti) or between inner, undistorted NPs of MgTi# samples (Figure 5.1b) and MgTi#H NPs (Figure 5.1d). Figure 5.2 displays the XRD

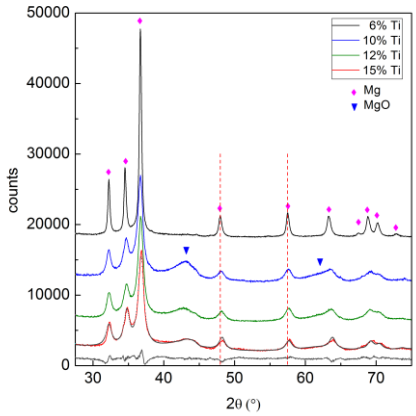

Figure 5.2 XRD pattern of the as-prepared MgTi# samples. The dashed lines highlight the shift of the Mg peaks with increasing Ti content. The best fit to the data and the residual are given for sample MgTi15 (grey lines).

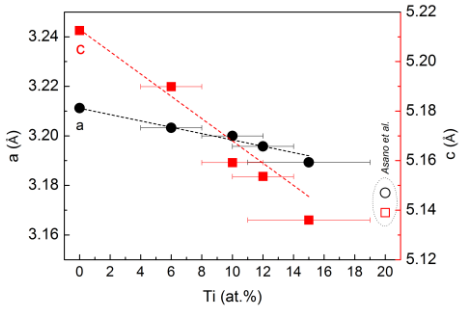

Figure 5.3 Cell parameters a and c of the hcp Mg structure in MgTi# samples, plotted as a function of Ti at%. The dashed lines represent a linear fit to the data. Open symbols are taken from ref. [53].

patterns of the MgTi# samples. While the Bragg reflections of *hcp* Mg are clearly visible, neither *hcp* Ti nor TiO_2 is observed. Notably, the Mg diffraction peaks move toward higher angles with increasing Ti content, revealing a contraction of the lattice parameters (Table 5.1). Figure 5.3 reports the lattice parameters *a* and *c* of the *hcp* Mg phase, determined by Rietveld refinement, against the Ti content determined by SEM-EDX. A linear fit of these data gives the correlation factors $\mathrm{R} = 0.997$ for *a* and $\mathrm{R} = 0.986$ for c. TEM-EDX mapping (Figure 5.4) shows that Ti is well dispersed in the NPs. The maps show a preferential location of O at the surface, together with Mg, whereas Ti coexists with Mg in the NP interior. It must be remarked that the NPs in Figure 5.4 were not compacted and therefore oxidation is expected to be stronger than for pellets. However, the presence

Table 5.1 Ti at% from SEM-EDX, phase abundance (wt%), crystallite size and lattice parameters of hcp Mg (above the dashed line) and rutile b-MgH2 (below the dashed line). The last column reports the weighted residuals of refinements.

Sample	Ti at% EDX	Phase abundance (wt.%)					Mg/β-MgH_2 cell parameters		Cryst. size (nm)			Rwp (%)
		MgH_2	Mg	MgO	TiH_2	Mg-Ti-H	*a* (Å)	*c* (Å)	Mg	β-MgH_2	TiH_2	
MgTi6	6(2)	-	100	0	-		3.2033(1)	5.1899(3)	37.8(2)			8.4
MgTi10	10(2)	-	61(5)	39(5)	-		3.2000(3)	5.1592(9)	11.5(1)			5.7
MgTi12	12(2)	-	66(2)	34(2)	-		3.1958(3)	5.1536(9)	11.5(2)			6.5
MgTi15	15(4)	-	75(1)	25(1)	-		3.1893(9)	5.1360(14)	11.8(1)			5
MgTi9H	9(1)	β-55(1) γ-3.5(3)	3.3(2)	27(1)	11(1)		4.5245(4)	3.0260(2)		32.5(3)	3.5(2)	5.8
MgTi12H	12(1)	β-29(1) γ-19(2)	-	23(1)	29(1)		4.5195(6)	3.0203(8)		11.7(1)	3.0(2)	4.7
MgTi22H	22(4)	β-32(1) γ-17(1)	-	10(1)	37(1)	4(1)	4.5175(9)	3.0260(13)		9.0(1)	4.9(4)	4.0

of MgO in the form of thin layers at open surfaces of the samples is also suggested by the broad MgO diffraction peaks observed in Figure 5.2 and Figure 5.5, from which a MgO crystallite size of ~ 3 nm can be estimated.

Figure 5.5 reports the XRD patterns of MgTi#H samples. The results of Rietveld refinement (Table 5.1) show that MgTi#H samples are composed mainly of rutile β-MgH_2 and orthorhombic γ-MgH_2. The presence of TiH_2 crystallites with fluorite structure and size less than 5 nm can be evinced from the presence of two bumps centred around 2θ positions compatible with the TiH_2(111) and (200) reflections, *i.e.* at 35.01 and 40.71, respectively (Figure 5.5). Hydride formation is almost complete in all samples: 3 wt% of residual *hcp* Mg is detected only in sample MgTi9H with the highest Mg content. The lattice parameters of β-MgH_2 are very close (within 0.2%) to those reported for bulk β-MgH_2 (lit.[57], *a*=4.5170 Å, *c*=3.0205 Å). Sample MgTi22H, the one with the highest Ti content (22 at%), exhibits a peak at $2\theta = 34.51$, marked "*", attributed to a Mg–Ti–H *fcc* phase not observed in the other samples.

The mean crystallite size of Mg and β-MgH_2, as determined from Rietveld refinement, decreases with increasing Ti content (Figure 5.6) and stabilises at about 12 nm above 10 at% Ti.

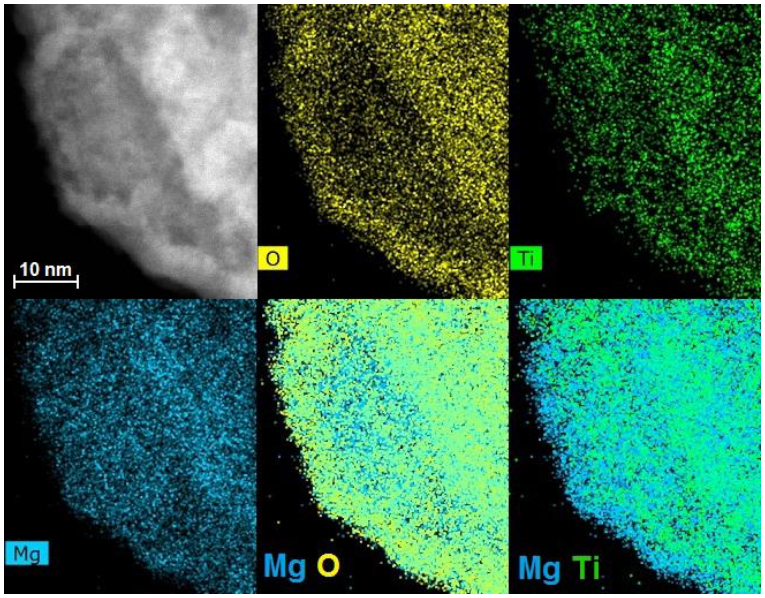

Figure 5.4 HAADF-STEM image (top left) and EDX mapping of Mg–Ti NPs showing O, Ti and Mg signals in yellow, green and blue, respectively. Ti atoms are dispersed in the core of the NPs while a MgO shell is formed after exposure to air.

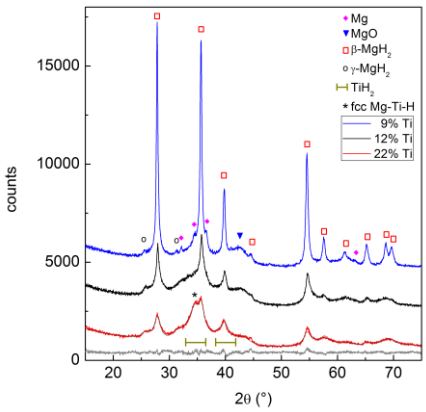

Figure 5.5 XRD profiles of the as-prepared MgTi#H samples. The best fit to the data and the residual are given for sample MgTi22H (grey lines).

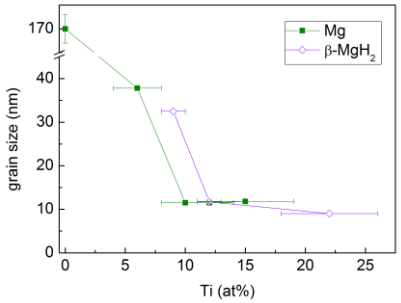

Figure 5.6 Mean crystallite size of the Mg and β-MgH_2 phases in MgTi# and MgTi#H samples, respectively, as a function of Ti content. The straight lines are a guide to the eye.

In MgTi#H samples, the Ti atomic fractions calculated from the relative abundance of the phases detected by XRD are compatible within the uncertainties with the Ti atomic fractions measured by SEM-EDX.

Hydrogen sorption properties

Before HPDSC measurements, MgTi# samples were activated for 3 h under 1 MPa H_2 at 300 °C. Without such activation, H-ab/desorption could not be observed under the temperature/pressure conditions of the experiments. Figure 5.7a shows that for sample MgTi10 the reacted fraction, proportional to the integral area of the peaks, increases with cycling. The same behaviour is observed in other MgTi# samples. Differently, MgTi#H samples needed no activation, readily desorbing H from the first cycle, as shown for sample MgTi12H in Figure 5.7b.

The enthalpy of hydride formation ΔH can be estimated from the HPDSC traces as explained by Rongeat *et al.*[58]: filling the van 't Hoff plot with the onset temperatures of absorption/desorption at different pressures under/overestimates the measure of ΔH. ΔH is then estimated as the average $(\Delta H_{abs} + \Delta H_{des})/2$ with an associated error $(\Delta H_{abs} - \Delta H_{des})/2$ (Table 5.2).

H-sorption kinetics were measured in the Sievert apparatus for samples MgTi12 and MgTi9H. MgTi12 absorbs and desorbs 2.8 wt% H in about 120 min. MgTi9H desorbs 2.7 wt% and absorbs 2.5 wt% in about 15 min. MgTi12 achieves 90% of reaction completion in about 50 min, MgTi9H in 2 min for desorption and less than 1 min for absorption.

Table 5.2 Enthalpy of hydride formation estimated from HPDSC measurements.

Sample	ΔH (kJ $\mathrm{mol}_{H_2}^{-1}$)
MgTi6	-75 ± 15
MgTi10	-79 ± 3
MgTi12	-78 ± 14
MgTi15	-73 ± 1
MgTi19H	-74 ± 7
MgTi12H	-72 ± 10
MgTi22H	-73 ± 3

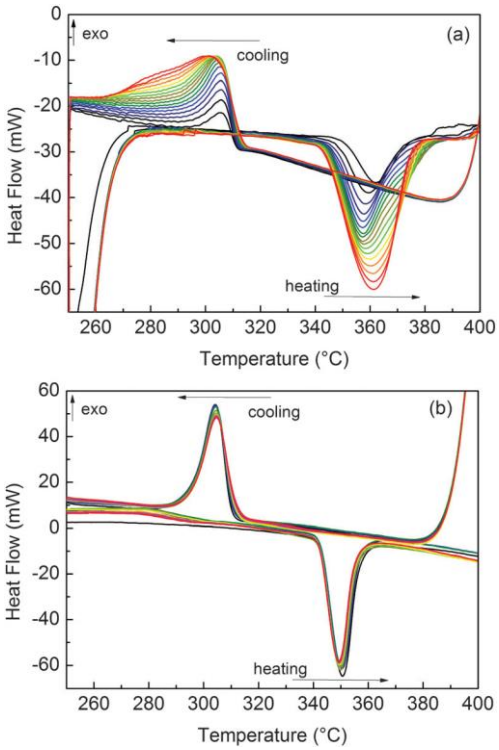

Figure 5.7 Evolution of the H-ab/desorption reactions in the HPDSC under 0.4 MPa of H_2 pressure. In these plots, MgTi10 is cycled 17 times (a) and MgTi12H 11 times (b). Cycling number increases progressively going from the black to the red lines.

After HPDSC cycles (ended with an absorption) the samples were again investigated by XRD. These patterns are shown in Figure 5.8 and the results of the Rietveld refinements are summarised in Table 5.3. The mean crystallite size of β-MgH_2 is significantly larger than in the as-prepared MgTi#H samples. The *hcp* Mg phase is still present in the MgTi# samples while it is not detected in the others (apart from very small amount in MgTi9H). Its crystallite size is up to 10 times larger than in the as-prepared samples, and its lattice parameters are close to those of bulk *hcp* Mg (lit.[11], *a*=3.2094 Å, *c*=5.2108 Å). After cycling, the main broad reflection of TiH_2 becomes clearly visible at position $2\theta = 35.01$. The MgO wt% is larger than in the as-prepared samples, especially for the MgTi#H samples, while γ-MgH_2 is no longer detected. The pellets are still intact after being cycled up to 31 times.

Table 5.3 Results of Rietveld analysis of the samples after cycling between 15 and 31 times in the HPDSC: phase abundance, crystallite sizes and lattice parameters of Mg and β-MgH_2.

Sample	Phase abundance (wt.%)				Cryst. size (nm)			β-MgH_2 cell parameters		Mg cell parameters	
	β-MgH_2	Mg	TiH_2	MgO	β-MgH_2	Mg	TiH_2	*a* (Å)	*c* (Å)	*a* (Å)	*c* (Å)
MgTi6	10(2)	25(4)	16(3)	25(4)	61(3)	53(5)	7(1)	4.5169(16)	3.024(2)	3.2109(8)	5.2132(14)
MgTi10	20(3)	55(4)	19(2)	55(4)	38(2)	39(6)	1.6(2)	4.5202(9)	3.0226(8)	3.2019(16)	5.203(5)
MgTi12	20(2)	59(2)	15(2)	59(2)	50(1)	100(30)	8 (1)	4.5186(9)	3.0219(10)	3.2109(12)	5.218(4)
MgTi15	13.4(6)	47(2)	22(2)	47(2)	46(4)	110(30)	4.1(2)	4.5191(11)	3.0212(12)	3.2064(10)	5.203(2)
MgTi9H	10.6(7)	82(3)	5.3(4)	82(3)	91(5)	53(14)	4.4(4)	4.5183(4)	3.0225(5)	3.2125(17)	5.223(6)
MgTi12H	7.3(5)	84(4)	8.7(5)	84(4)	38(1)	-	4.7(1)	4.5190(12)	3.0232(13)	-	-
MgTi22H	8.6(6)	75(4)	17(1)	75(4)	42(4)	-	6.1(7)	4.523(2)	3.027(2)	-	-

Discussion

Formation of Mg–Ti solid solution and the effect of in situ H-absorption

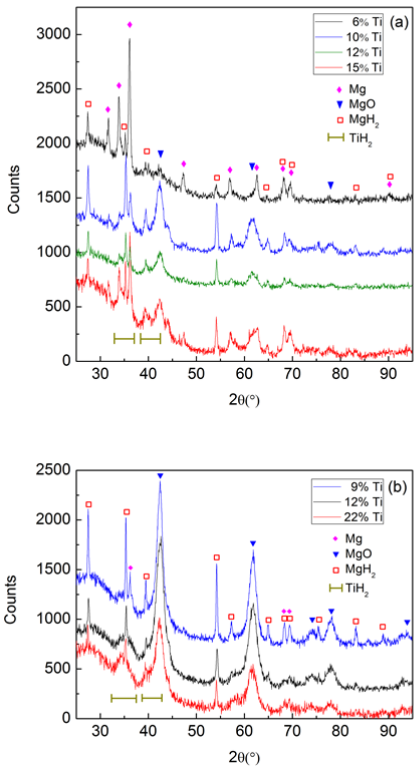

Figure 5.8 XRD profiles of MgTi# (a) and MgTi#H (b) samples after HPDSC cycles, ended with an absorption.

Mg and Ti are immiscible at equilibrium[59],21 but can form a metastable alloy. The contraction of the unit cell observed in our as-prepared MgTi# samples (Figure 5.3) can be attributed to substitutional Ti in the *hcp* Mg lattice. This is in agreement with Vegard's empirical law, since Ti crystallises in the *hcp* structure with lattice parameters smaller than Mg (lit.[59], a=2.9511 Å, c=4.68433 Å) and the contraction is linear with Ti content. Fig. Figure 5.9 shows the XRD profile of another sample with 23 at% Ti without *in situ* hydrogenation where new peaks suggest the presence of small amounts of *hcp* Ti. Metastable *hcp*, *fcc* and *bcc* Mg–Ti alloys have been observed, both rich in Mg[20,53,55] and in Ti[54,60]. Asano *et al.*[53] studied the structure of Mg–Ti milled powders between 20 at% and 65 at% Ti. After prolonged milling (200 h) they obtained a *hcp* $Mg_{80}Ti_{20}$ phase whose lattice parameters are in good agreement with our data (Figure 5.3). At higher Ti content, they observed the formation of both *bcc* and *fcc* Mg–Ti alloys, depending on the milling energy. Anastasopol *et al.*[55] synthesised Mg–Ti NPs with 30 at% Ti via spark discharge generation (SDG), and found a Mg–Ti *bcc* phase mixed with the pure and separated Mg and Ti *hcp* phases. These findings suggest that the solution of Ti in Mg reported in this work up to 15 at% Ti could extend to about 20 at% Ti, while at higher Ti contents Ti-rich phases start to appear.

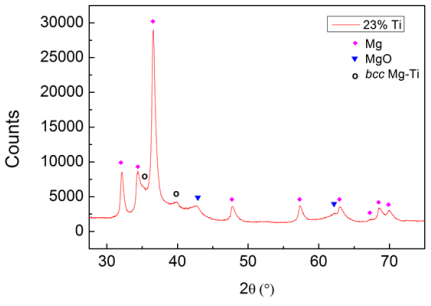

Figure 5.9 XRD profile of an as prepared sample without in situ hydrogenation with 23 at.% Ti.

The observation of TiH_2 and β-MgH_2 with lattice parameters close to the bulk values (Figure 5.5) in the MgTi#H samples suggests that, during the first H-absorption, Ti atoms dissolved in the NPs segregate out of the Mg lattice while forming the hydride. A rough estimate of the average number *n* of TiH_2 crystallites per MgH_2 crystallite, assuming spherical crystallites, can be obtained simply from the formula:

$$n = \frac{V_{TiH_2} d_{MgH_2}^3}{V_{MgH_2} d_{TiH_2}^3} \tag{5.1}$$

where *d* is the crystallite size of the hydride phases and the volume ratio V_{TiH_2}/V_{MgH_2} is calculated from the weight fractions determined by XRD (Table 5.1) using hydride densities[52] $\rho_{MgH_2} = 1.45$ g cm^{-3} and $\rho_{TiH_2} = 3.75$ g cm^{-3}. This equation yields a value of *n* that increases from 3 to 13 as the MgH_2 crystallite size increases from 9 nm to 33 nm, suggesting that the decomposition gives rise to several TiH_2 crystalline domains per NP.

The XRD pattern of sample MgTi22H (Figure 5.5) reveals the presence of a Mg–Ti–H *fcc* phase, in agreement with previous reports at higher Ti content[54,55,61,62]. The lattice parameter of 4.51(1) Å is very close to the value of 4.49 Å reported for the $Mg_{42}Ti_{58}H_{177}$ composition[63]. Such a Mg–Ti–H *fcc* phase is known to form upon hydrogenation of the previously discussed *bcc* $Mg_{50}Ti_{50}$ phase[63], which is synthesised in Mg–Ti systems with Ti content >20 at%: this explains why it is present in sample MgTi22H only. The Mg–Ti–H *fcc* phase is not detected in the XRD pattern of Figure 5.8, meaning that it decomposed upon cycling in the HPDSC. Instability upon H-cycling was generally reported for this ternary compound, and for other Mg–Ti–H phases with different structures[64–66].

MgO formation, TiO_2 absence

Considering that the MgO crystallite size corresponds to the formation of an oxide shell of thickness $d_{shell} = 3$ nm around a Mg/MgH_2 sphere of diameter d_{core} equal to the Mg or β-MgH_2 crystallite size (for MgTi# or MgTi#H samples, respectively), we can estimate the shell to core weight fraction m_{shell}/m_{core} using Equation (4.6) where $\rho_{shell} = 3.58$ g cm^{-3} is the MgO density, $\rho_{core} = 1.74$ g cm^{-3} or 1.45 g cm^{-3} is the Mg or β-MgH_2 density,[52] respectively. This simple core–shell model overestimates from 3 to 30 times the amount of oxide, compared to the experimental data. This result suggests that the 3 nm thick MgO layer does not form around each NP but

around high density assemblies of NPs produced by compaction when the samples are exposed to the oxidising atmosphere.

Oxidation of MgTi# samples partially decomposes the Mg–Ti alloy. Since TiO_2 is less stable (lit.[52], $\Delta_f H°\ 298.15\ \mathrm{K} = -944\ \mathrm{kJ\ mol}_{\mathrm{O_2}}^{-1}$) than MgO (lit.[52], $\Delta_f H°\ 298.15\ \mathrm{K} = -1204\ \mathrm{kJ\ mol}_{\mathrm{O_2}}^{-1}$), Mg is segregated out of the NPs to form a protective MgO layer that prevents further oxidation of NPs[67]. This phenomenon is observed in TEM-EDX maps (Figure 5.4), in particular the last one showing Mg and Ti signals together, where only Mg (bonded to O) is at the surface. In MgTi#H samples, the absence of TiO_2 is due to the high TiH_2 stability to O_2.

NP size vs. Ti content

The Mg/MgH_2 crystallite size decreases with increasing Ti content and is weakly affected by in situ hydride formation. In Chapter 4 we showed that in the case of Mg NPs without Ti, capillary forces induce the crystal growth of deposited Mg NPs by the grain rotation coalescence/oriented attachment (GRC/OA) mechanism, eventually yielding NPs and crystals larger than 200 nm. Interestingly, Ti seems to inhibit this mechanism by acting as a grain refiner. As a possible explanation for this effect, we consider different atomic sizes and electronic structures of the two elements. The random distribution of Ti atoms at the NP surface locally deforms the *hcp* Mg lattice. Because of this random deformation, it is no longer possible for two adjacent NPs to achieve perfect lattice coincidence by simple rotation/translation and the driving force for GRC/OA is correspondingly reduced. This effect gains importance with increasing Ti content. Our results suggest that coalescence of the as-deposited NPs becomes inhibited for Ti content above 10 at%, where the crystallite size reaches a lower limit. This minimum crystallite size is probably representative of the primary NP size formed in the gas phase, prior to their agglomeration and coalescence. Lu *et al.*[18] showed that 10 at% Ti in reactively ball milled MgH_2 is a sufficient quantity to have very good kinetics and cyclability.

Effects of in situ hydride formation on H-sorption kinetics

Three experimental results clearly indicate that MgTi#H samples exhibit kinetic properties and activation behaviour superior to MgTi#:

i. the direct comparison between isothermal H-sorption kinetics reported in Figure 5.10;

ii. the presence of *hcp* Mg in MgTi# samples after several HPDSC cycles ending with H-absorption (Figure 5.8 and Table 5.3), meaning that part of Mg never transformed into hydride;

iii. the fact that, for MgTi# samples, the integral area of the HPDSC peaks in Figure 5.7 increases with cycling and the H-absorption peaks are highly asymmetrical.

The peak asymmetry can be due to the overlapping of two H-absorption processes with different kinetics. The sample fraction, which already reacted during previous cycles, likely contributes to the fast process. Differently, H-absorption by sample regions that were not activated in previous cycles contributes to the slow component and to the progressive increase of the peak integral area. The slower H-absorption process continues with decreasing speed since the diffusion coefficient decreases during cooling until it is completely blocked by low temperature (260 °C). Also, as the reaction proceeds MgH_2 may grow preferentially near the surface forming a shell/core MgH_2/Mg structure. Diffusion of hydrogen in the MgH_2 shell (slower than in Mg) contributes to the slower process since the shell increases in thickness as absorption advances.

For practical H-storage applications it may be more convenient to handle pellets rather than nanopowders. In this respect, our results suggest that hydride formation before NP compaction is beneficial to kinetic and activation behaviour. A possible explanation for this observation may be searched in the higher ductility of metallic Mg in comparison with hydride MgH_2, which results in a lower porosity of the compacted pellets for MgTi# samples, as can be seen by comparing SEM Figure 5.1a and c. If porosity is low, H cannot reach the inner pellet regions simply by gaseous diffusion, and a

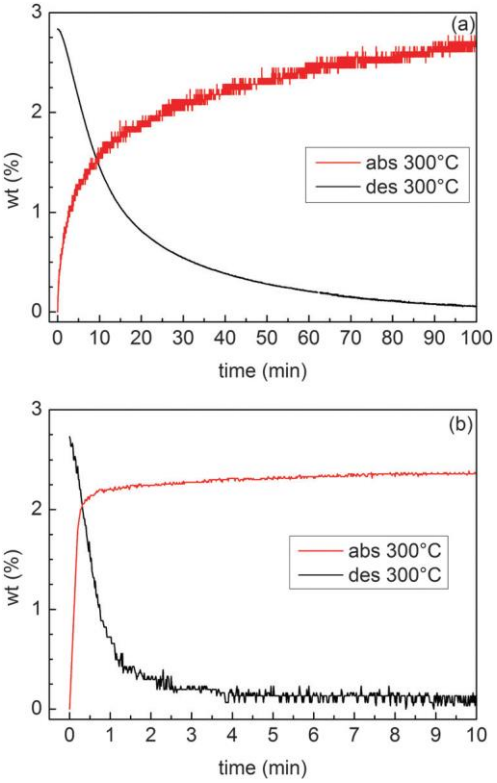

Figure 5.10 H-sorption kinetics of the samples MgTi12 (a) and MgTi9H (b) at 300 °C. The initial H_2 pressure is 0.9 MPa for absorption and 0.015 MPa for desorption.

slower process, i.e. diffusion along interfaces, becomes the dominant transport mechanism. Since MgTi# and MgTi#H samples have a similar crystallite size, the difference in the kinetic properties cannot be attributed to a different volume fraction of interfaces, while it could be ascribed to a different porosity. The difference in porosity observed for the two sets of samples reveals also why MgTi# samples needed an activation treatment. The as prepared MgTi# samples have a less porous surface that slows down H-sorption reactions to the point that they are not measurable on a single HPDSC run (~30 min). To activate the samples, prolonged exposure to H is needed to crack the surface thanks to the volume expansion that occurs in the metal to hydride transition. The beneficial effects of activation and cycling can be seen comparing SEM images before (Figure 5.1a) and after cycling (Figure 5.11). The pore structure as a function of both compaction pressure and hydride formation treatment could be the subject of a future study aimed at optimising H-sorption kinetics of the pellets. On the other hand, a lower porosity and a lower surface area reduce the risk of contamination by oxygen and moisture when the pellets are exposed to air, and this can explain why MgTi# samples have a lower oxide content after HPDSC cycles in comparison with MgTi#H samples (Table 5.3).

It is nevertheless worth remarking that if the amount of produced material is small, residual impurities present in the H_2 gas or desorbed from the equipment walls can lead to extensive oxidation[55], even if the transfer processes are carried out under a clean atmosphere.

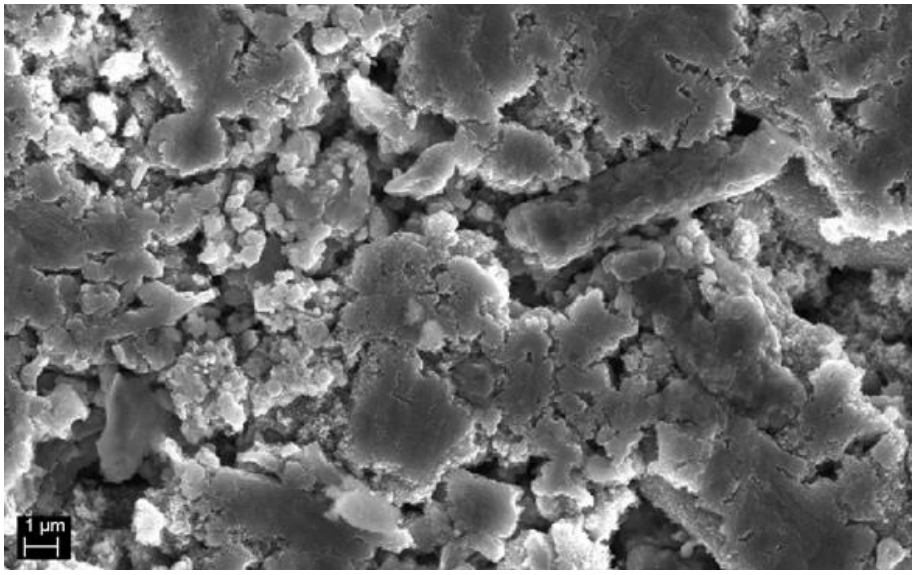

Figure 5.11 SEM image of sample MgTi15 after cycling in the HPDSC.

The H-sorption kinetics in Figure 5.10b are among the fastest reported for Mg-based materials. TiH_2 is known to be a good catalyst and it has been proposed[18] to act as a gateway for hydrogen since it helps in the dissociation of H_2 and H diffusion is fast through TiH_2 octahedral sites[18,19,68]. Moreover, Ti combines well by the IGC technique for the production of smaller Mg NPs. All these effects contribute to the increase in the kinetic performances of this material.

Thermodynamics of H-sorption

For all samples, independently of the kinetic behaviour, we determined the enthalpy of hydride formation (Table 5.2) compatible (within the uncertainties) with the one reported for bulk Mg (lit.[69], $-74.1 \pm 2.9\ \mathrm{kJ\ mol_{H_2}^{-1}}$). Hydride formation/decomposition and high temperature operation lead to segregation of MgH_2 and TiH_2 phases and to significant crystallite growth of Mg/MgH_2 (as reported in Table 5.3). Therefore, thermodynamic changes due to Ti substitution in *hcp* Mg are not expected. In another paper[70], Asano *et al.* demonstrated clearly that MgH_2 nanometer-sized clusters in a TiH_2 matrix have a reduced enthalpy of formation because of interface effects. The enthalpy of formation is lowered by $\sim 10\ \mathrm{kJ\ mol_{H_2}^{-1}}$ for samples with >60 at% Ti content and Mg NPs size <3 nm while our samples have <23 at% Ti and NPs size >10 nm. Furthermore, MgH_2 and TiH_2 are no longer finely dispersed after *in situ* hydride formation at 150 °C. The coarsening of the microstructure reduces the volume fraction occupied by MgH_2/TiH_2 interfaces. In this scenario, modification of thermodynamics due to interface energy effects[21,70] or coherency strain[71] may be too small to be detected.

Our results, suggesting no change in the thermodynamics of H-sorption in samples subjected to H-sorption cycles in the 260–400 °C range, fully agree with previous investigation on MgH_2/TiH_2 reactively ball-milled nanocomposites[19].

Conclusions

The condensation of a mixture of supersaturated Mg and Ti metal vapours leads to the formation of Mg–Ti NPs with a Ti solubility in the *hcp* Mg lattice, which extends well beyond the solvus line of the bulk phase diagram. This important result sets gas-phase condensation as a powerful, up-scalable tool for the bottom-up preparation of metastable NPs constituted by elements with poor mutual solubility. The synthesis method also demonstrated a good control over the product composition with overall structural and

chemical homogeneity. Upon hydrogen absorption, the structural changes associated with the metal-hydride transformation push the system out of its metastable state, and an MgH_2/TiH_2 nanocomposite develops. A possible exception to this decomposition path occurs only at higher Ti content (>20 at%) where an *fcc* Mg–Ti–H phase is observed and is ascribed to H-absorption by *bcc* Mg–Ti. It is worth remarking that Asano *et al.*[53] reported a similar phase landscape for Mg–Ti samples synthesised by top-down ball milling.

Mg–Ti NPs are less prone to coarsening and recrystallisation by oriented attachment than Mg NPs: above 10 at% Ti, a lower limit of about 10 nm is obtained for the Mg–Ti crystallite size.

The presence of Ti or its hydride results in excellent H-sorption kinetics, in particular for NPs subjected to hydride formation before *in situ* compaction. Conversely, the enthalpy of hydride formation ΔH, as measured by HPSDC in the 260–400 °C range, does not differ from the one reported for pure, bulk Mg. This result is contrary to the strong ΔH and ΔS reduction reported in Mg–Ti nanoparticles with about 30 at% Ti synthesised by spark discharge generation[55] ($\Delta H = -45\ \mathrm{kJ\ mol}_{\mathrm{H_2}}^{-1}$). The reason for this difference appears to be the higher stability of the *bcc* Mg–Ti phase in NPs with higher Ti content, leading to a different H-sorption path, *i.e.* from *bcc* Mg–Ti to *fcc* Mg–Ti–H, with different thermodynamics. Conversely, at lower Ti content –and therefore at higher reversible H-storage capacity– the reversible transformation path goes from *hcp* Mg to *bct* MgH_2, in agreement with experiments on ball-milled samples[19].

5.2 Mg-Ti nano-powders

Synthesis conditions

Like in the previous Section, Mg-Ti NPs were synthesised evaporating simultaneously Mg ingots (Alfa Aesar, purity 99.9%) and Ti powder (Alfa Aesar, purity 99.9%, 150 mesh) in two different crucibles, with the gas flow that crosses the Mg vapour source first, then the hotter Ti source and finally hits the cylinder where the NPs are collected. The Ti content was controlled changing the power applied to the Ti source.

One subset of samples was synthesised by "standard" IGC, *i.e.* with the He flow rate set to 7.0 std cm^3 min^{-1} keeping the chamber pressure at 270 Pa. The other subset instead, was synthesised by RGC, adding an equivalent flow rate of H_2 (7.0 std cm^3 min^{-1}) next to the He flow (see Figure 2.5). Also the equimolar He/H_2 mixture was kept constant at 270 Pa.

After the evaporation, once in the secondary chamber NPs were exposed to 13.3 kPa of H_2 for ~3600 s at a temperature of 400 K. The NPs treated in this way and just extracted from the chamber will be named *as-prepared NPs*, to distinguish them from those treated at higher temperature and hydrogen pressure in the Sievert apparatus.

The average $X_{\mathrm{Ti}} \equiv$Ti/(Mg+Ti) atomic ratio ranges from 6 up to 60 at%; from here on we will call the corresponding samples MgTiX_{Ti}.

The amount of material obtained in one batch ranges between 15 mg and 60 mg.

Characterisation of as-prepared NPs *In operando* hydrogenation

In Figure 5.12 is shown an XRD profile of Mg-Ti NPs synthesised by RGC, before the *in situ* hydrogen absorption treatment in the secondary chamber. Figure 5.12 indeed shows that the NPs contain a mixture of Mg and MgH_2 just after the synthesis. In fact, once NPs are cooled below about 390 K by collisions with the gas molecules, the equilibrium pressure of

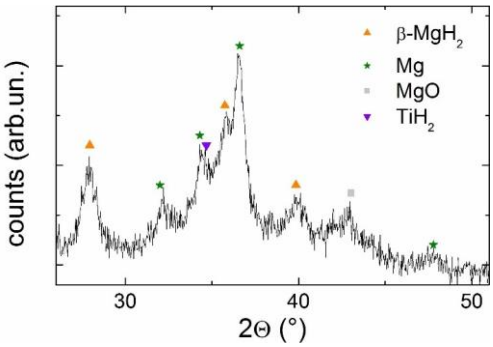

Figure 5.12 XRD pattern of RGC sythesised MgTi6 NPs extracted before the in situ hydrogen absorption treatment in the secondary chamber, showing that partial MgH_2 formation takes place already as a consequence of the H_2-enriched synthesis atmosphere. The pattern is noisy because the sample quantity for this experiment was rather low.

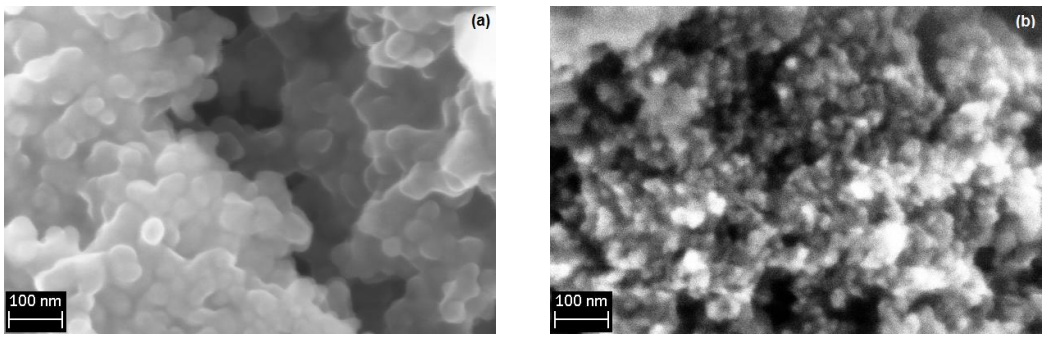

Figure 5.13 SEM images showing the morphology of as-prepared NPs in sample MgTi24 (a) and MgTi6 (b).

MgH_2 becomes higher than the hydrogen partial pressure in the chamber (135 Pa), allowing the formation of the hydride. Most likely, the metallic Mg detected lies in the NP core while the hydride formation is limited to the NP surface because the rapid quenching each NP experiences, kinetically blocks any further absorption of H.

After the *in situ* absorption treatment, hydrogenation is complete and RGC and IGC synthesised samples become alike. Therefore, in the following, samples will be discussed disregarding of the inert or reactive atmosphere used during synthesis.

Morphology and crystaline structure

The FE-SEM pictures in Figure 5.13 show the typical morphology of the as-prepared samples. The individual NPs can be resolved within the large agglomerates, which constitute the nanopowder. The NPs size is in the 10-20 nm range, in agreement with reports on the pellet-shaped samples of Section 5.1. The different Ti contents do not induce evident changes in NPs

Table 5.4 Weight fraction of the crystalline phases in as-prepared NPs (upper part) as a function of X_{Ti}, determined by Rietveld refinement of XRD profiles. For the phases β-MgH_2 and ε-TiH_2, the crystallite size d and lattice parameters are also reported. Rietveld agreement factors R_{wp} and R_{exp} are given. The numbers in parenthesis represent the standard deviations referred to the last digit. Where no error is given, the parameter was fixed to ensure fit stability due to the low phase amount and/or very small crystallite size. The lower part of the table reports the same data for the NPs after hydrogen sorption cycles at T>430 K.

X_{Ti}			β-MgH_2			ε-TiH_2			MgO	γ-MgH_2	Mg	R_{wp}	R_{exp}
at%	wt%	*d* (nm)	*a* (Å)	*c* (Å)	wt%	*d* (nm)	*a* (Å)	*c* (Å)	wt%	wt%	wt%	(%)	(%)
as-prepared NPs													
6(1)	65(5)	20(2)	4.5190(2)	3.0229(3)	16(3)	2.5(5)	3.1871	4.381	6(2)	12(1)	1	5.1	1.3
15(2)	53(5)	18(2)	4.5200(6)	3.0224(7)	26(3)	6(1)	3.1871	4.381	10(1)	10(1)	1	6.7	2.0
30(3)	34(3)	15(1)	4.5224(4)	3.0227(5)	49(5)	7(1)	3.1871(6)	4.381(2)	9(1)	8 (1)	2(1)	4.0	1.9
60(5)	8(1)	13(1)	4.5205	3.0267	86(7)	9(1)	3.196(1)	4.360(2)	3(1)	0	3(1)	5.7	2.2
after hydrogen sorption cycles at T> 430 K													
6(1)	78(5)	80(8)	4.5193(2)	3.0225(1)	13(2)	4	3.1831	4.386	9(1)	0	0	5.5	2.8
30(3)	36(4)	25(3)	4.5207(4)	3.0242(3)	55(5)	7(1)	3.1831(7)	4.386(2)	9(1)	0	1	5.1	2.1
60(5)	7(2)	14	4.529(2)	3.0267	85(7)	8(1)	3.192(1)	4.381(2)	8(2)	0	0	6.4	2.8

shape or level of aggregation, but have an effect on the average NP size. NPs in sample MgTi24 (Figure 5.13b) appear smaller than those of sample MgTi6 (Figure 5.13a), with a lower Ti content. This is also in agreement with the measured mean crystallite size as it will be discussed quantitatively in the following X-ray diffraction study. No significant differences were found between IGC and RGC synthesised NPs.

Figure 5.14 displays the XRD patterns of emblematic as-prepared NPs with a Ti content X_{Ti} that spans over the whole investigated range. The corresponding quantitative Rietveld analyses are summarised in Table 5.4. MgH_2 occurs in two phases: rutile-type tetragonal β-MgH_2 and orthorhombic γ-MgH_2, a polymorph that is stable at high pressure and is usually found in ball-milled MgH_2.[19] The β-MgH_2 crystallite size decreases with increasing X_{Ti}, as already observed for Mg-Ti NPs synthesised under inert He atmosphere in Section 5.1. The lattice parameters of the β-MgH_2 phase (Table 5.4) in the NPs are very close to the bulk values (a=4.5185 Å and c=3.0220 Å, this work, or a=4.5180 Å and c=3.0211 Å [72]), the discrepancy being lower than 0.1% for all samples. Figure 5.15 displays the relative variation of the β-MgH_2 unit cell volume in the Mg-Ti NPs with respect to bulk β-MgH_2, measured as a function of X_{Ti}. If Ti solubility in MgH_2 occurred, one would expect a shrinkage of the unit cell by about 0.3% per at% Ti [23]. Instead, Figure 5.15 shows a very small –if any-

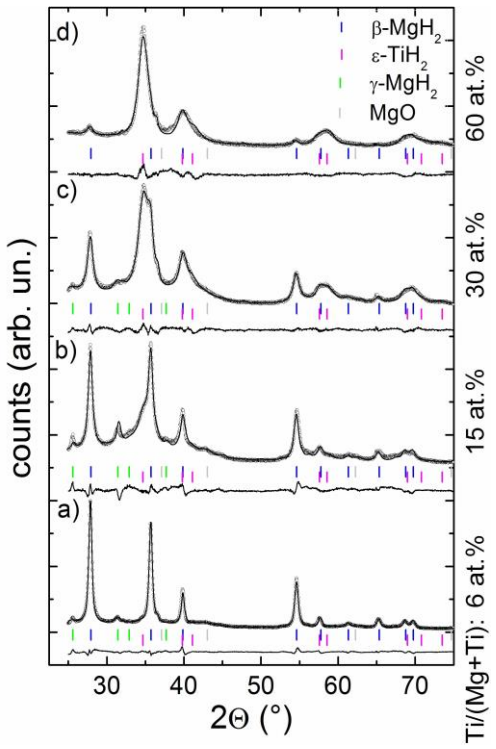

Figure 5.14 XRD patterns of as prepared NPs with different Ti content X_{Ti}. Open circles are experimental data while the calculated Rietveld best fit is represented by the solid line. The fit residual is shown below each pattern, and the coloured vertical bars mark the Bragg reflections of the main crystalline phases. For γ-MgH_2, only the first four peaks are marked because the other ones are too weak. The Bragg peaks of metallic Mg, the fraction of which is always below 3 wt%, are not indicated.

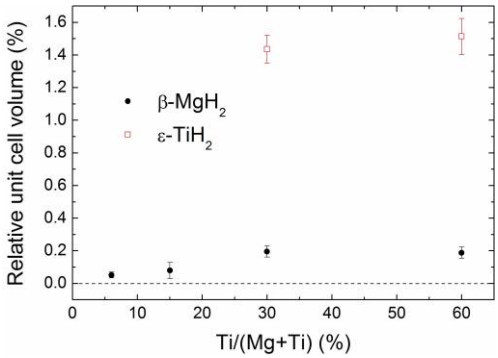

Figure 5.15 Variation of the unit cell volume in Mg-Ti NPs as a function of the average Ti content. The dashed line represents no volume variation with respect to bulk pure hydride powders.

volume expansion in the 0.05 to 0.2 % range, demonstrating that no significant solubility of Ti in β-MgH_2 takes place within the NPs.

The β-MgH_2 to γ-MgH_2 weight ratio diminishes slightly from ~5.4 to ~4.3 with increasing X_{Ti} from 6 to 30 at.%. The reflections of γ-MgH_2 are not observable in the XRD pattern of sample MgTi60: the detection and the quantitative analysis of minority phases in these NPs are rather difficult and prone to large relative errors, if not impossible, because of the severe line broadening due to the small size of coherently diffracting domains.

TiH_2 is known to exhibit a transition from a fluorite cubic structure (δ-TiH_2, space group *Fm*-3*m*) to a tetragonal structure (ε-TiH_2, space group *I*4/*mmm*) on cooling at about 17 °C [73]. The same transition is observed with increasing pressure above 2.2 GPa. The ε-TiH_2 phase was also detected as majority phase in MgH_2-TiH_2 ball-milled nanocomposites on a wide composition range[19]. In the cubic to tetragonal transition, the (200), (220) and (311) reflections of the cubic structure split in two tetragonal reflections. In our XRD patterns, the line broadening makes it difficult to distinguish between the two phases. Nevertheless, the Rietveld refinement of MgTi30 and MgTi60 reveals that the tetragonal ε-TiH_2 phase dominates. Better fit quality is obtained with ε-TiH_2. In the samples MgTi6 and MgTi15, the low Ti content does not allow to identify unambiguously the TiH_2 phase because the fit quality does not change significantly and the reflections at high angles are very weak. The results reported in Table 5.4 are obtained assuming the presence of the tetragonal phase. The TiH_2 crystallite size decreases with increasing Mg content, reaching an extremely low value of about 2.5 nm in sample MgTi6. The lattice parameters could be determined reliably only for samples MgTi30 and MgTi60 with a higher Ti content: the relative variation of the unit cell volume with respect to ball-milled ε-TiH_2 powders[19] is displayed in Figure 5.15, showing a volume expansion of about 1.4 %. Using Vegard's law and literature data for MgH_2 and TiH_2 cell volumes[19,23], we can attribute this result to a Mg solubility in TiH_2 of about 5 at.%. This conclusion is also supported by Figure

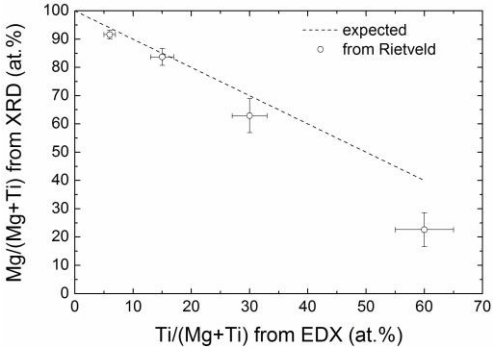

Figure 5.16 Mg atomic fraction determined from Rietveld analysis versus Ti atomic fraction measured by EDX. The dashed line represents the equation y=100-x, i.e. the Mg fraction measured by EDX. The deviation of the experimental data from this line indicates that Rietveld analysis underestimates the Mg content, probably due to a certain degree of Mg solubility in TiH_2.

5.16, which depicts the Mg/(Mg+Ti) ratio obtained from the Rietveld phase abundances. The clear Mg underestimation compared to EDX results may well be due to a certain degree of Mg solubility in TiH_2, which the Rietveld model does not account for.

The other phase observed in relevant amount is MgO, which exhibits broad lines indicating a very small crystallite size of 4-5 nm for all samples. Its fraction, which never exceeds 10 wt%, is remarkably low compared to the Mg-Ti nano-pellets (Table 5.1) or previous reports on Mg-based NPs of similar size[55]. The fraction of oxidized Mg atoms calculated from the Rietveld analysis exhibits a positive correlation with X_{Ti}, increasing from about 5% in Mg-6Ti to 15% in Mg-60 Ti.

It is worth noticing that the as-prepared NPs are relatively stable against oxidation even under ambient conditions. In fact, the XRD patterns reported in Figure 5.14 were collected under air in a typical time of about 1 hour. No significant changes in the patterns were observed by immediately repeating the measurements.

Finally, small residues of metallic Mg are detected (1-3 wt%), while neither metallic Ti nor Ti oxides are observed, confirming that hydride formation is almost completed in the as-prepared NPs.

Single NP characterisation

In order to gain insight on the element distribution at the single NP level, morphological and elemental analysis were performed with TEM. Figure 5.17 displays HAADF-STEM images of as prepared NPs MgTi6 (a, c) and MgTi 30 (b, d). The NP size is determined clearly, it ranges between 10 and 20 nm confirming the SEM observation, and it is compatible with the *d* values size determined by XRD for β-MgH_2, suggesting a one-to-one correspondence between NPs and β-MgH_2 crystallites. Since the contrast in incoherent HAADF images is proportional to the square of the atomic number, the brighter areas can be ascribed to a Ti-rich phase in the NPs, *i.e.* to TiH_2 based on XRD analysis. Furthermore, STEM-EDX line-scans of Mg and Ti elements (Fig. 3 e,f) detect the X-ray fluorescence of both elements at almost every step within the NPs. The count fluctuations represent local compositional changes and/or thickness variations. The results shown in Figure 5.17 are representative of a large number of investigations on similar NPs.

In summary, the following picture emerges from combined XRD and STEM analyses: each NP is a nanocomposite, where ultra-fine TiH_2 crystallites are dispersed within an MgH_2 matrix constituted by a single crystalline

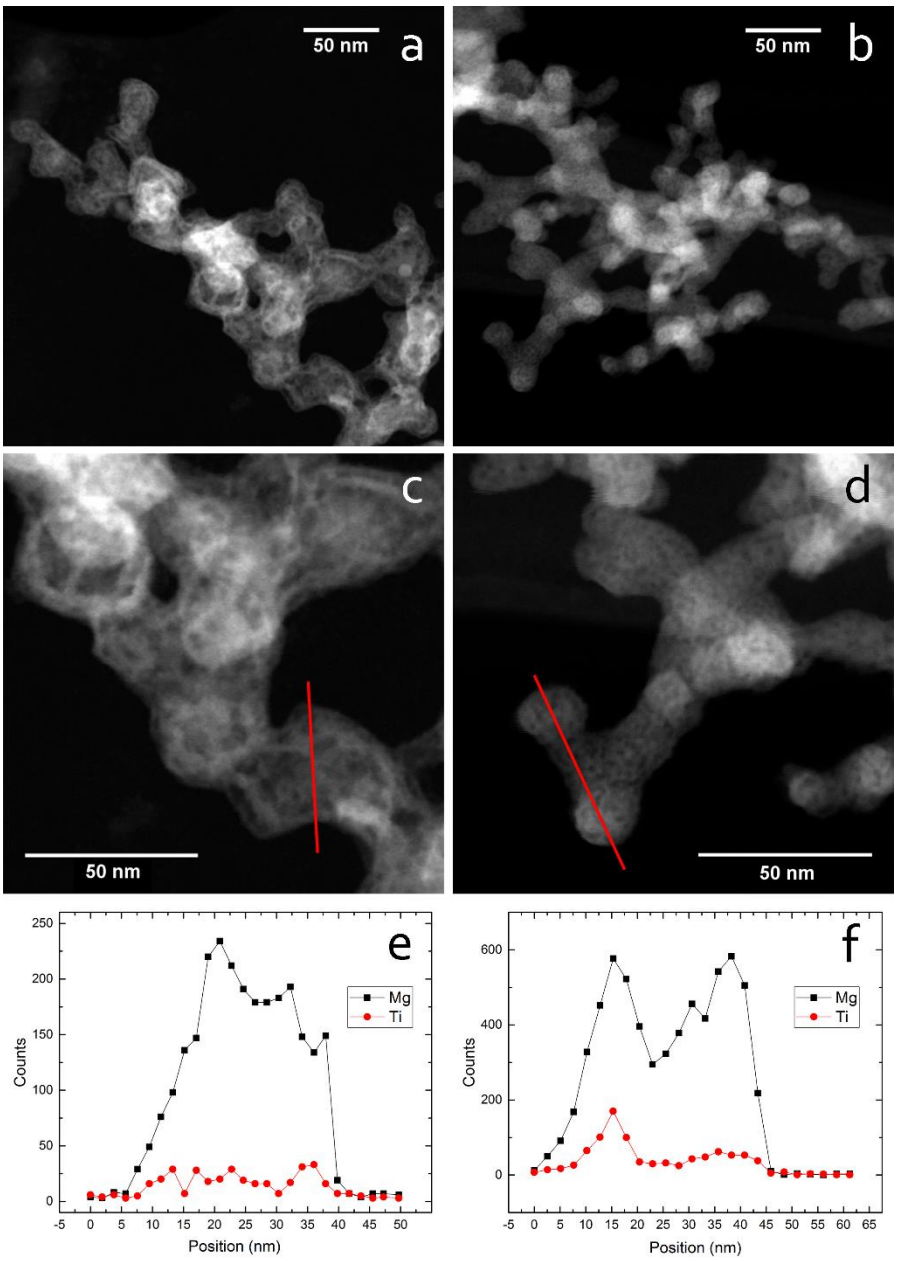

Figure 5.17 HAADF-STEM images at different magnifications of as prepared Mg-6Ti (a, c) and Mg-30Ti (b, d) NPs; frames e, f display the corresponding STEM-EDX line scans taken along the red lines in c, d.

grain. The TiH_2 crystallites actually contain some dissolved Mg, whereas no significant solubility of Ti in MgH_2 occurs.

Reaction mechanism

The time evolution of the compounds during H-absorption and desorption was studied on sample MgTi6 by the *in situ* synchrotron radiation (SR)-XRD set-up[62,74] implemented at the beamline I711 of MAX II synchrotron

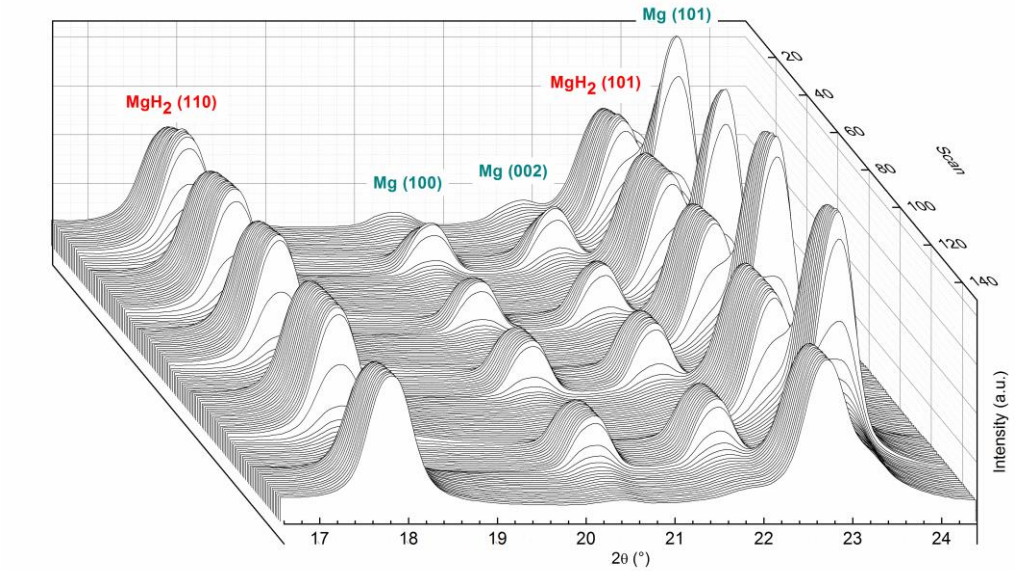

Figure 5.18 In situ SR-PXD patterns of sample A while being cycled at 280 °C. A diffraction pattern is acquired every 34 s.

in the research laboratory MAX-lab, Lund, Sweden. Sample transfer from the synthesis chamber into the SR-XRD set-up was entirely performed under Ar atmosphere.

Sample MgTi6 was kept at 553 K and alternately exposed to vacuum (~8 kPa) and H_2 pressure (>500 kPa) in order to complete five cycles while recording XRD patterns every 34 s. The X-ray wavelength used for this experiment was 0.9938 Å.

All the SR-XRD patterns taken during the five desorption-absorption cycles at 553 K cycles are plotted in Figure 5.18. The only observed Bragg reflections are Mg and MgH_2. Mg and MgH_2 peaks appear and disappear alternately as the sample is exposed to H_2 pressure or vacuum. To better appreciate the time evolution of the two phases, the intensities of the non-overlapped reflections, *i.e.* Mg (100) and MgH_2 (110), are normalised separately between 0 and 1 and plotted as a function of time in Figure 5.19. The intensities of Mg and MgH_2 always sum to 1 point by point, the dashed horizontal line

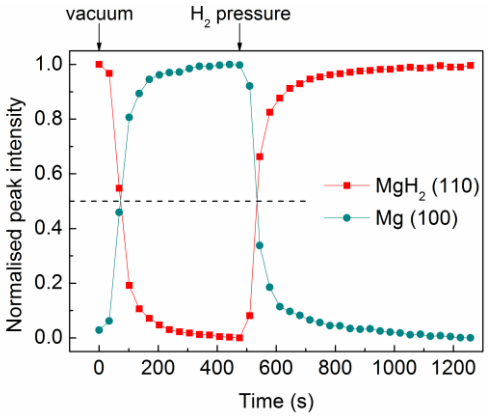

Figure 5.19 Normalised intensities of the (100) Mg and (110) MgH_2 reflections of Figure 5.18 during one cycle. The lines are a guide to the eye.

drawn at half intensity highlights the symmetrical evolution of the two phases. This is the demonstration that the ongoing reaction is simply the reversible hydrogen absorption and desorption of magnesium.

As it will be shown, the equilibrium measurements in the Sievert apparatus also support this result.

H-sorption kinetics and thermally induced changes

The reaction kinetics were studied on sample MgTi6 paying attention to avoid strong microstructural and morphological evolution during cycling at different temperatures. To do that, H desorption-absorption cycles were recorded in two sets of measurements, every time in order of decreasing temperature. In the first set, identified as $T_{max} = 523\ K$, kinetics were measured first at 523 K and subsequently at 508 K, 493 K, 478 K (Figure 5.20a). In the second set, the order was 573 K, followed by 238 K, 523 K and 478 K (Figure 5.20b) and we will refer to it as $T_{max} = 573\ K$. The initial pressure was chosen in order to maintain the same driving force, namely $T_{DF} = T\left(1 - \sqrt{P_{eq}/P_{abs}}\right) = 230$ K for absorptions and $T_{DF} = T\left(1 - \sqrt{P_{des}/P_{eq}}\right) = 320$ K for desorptions, resulting in an initial pressure between 8 mbar and 320 mbar for desorptions and between 260 mbar and 4.5 bar for absorptions for the 205-573 K temperature range. All the curves were fitted with the Johnson-Mehl-Avrami (JMA) model for random nucleation and growth:

$$\alpha = 1 - e^{-\,kt^{\,n}} \tag{5.2}$$

where α is the reacted fraction at the time *t*. The data fitted were in the $0 < \alpha < 0.8$ range, as the JMA model hypotheses do not hold in the last stage of the phase transition. The kinetic parameters k derived from the fits

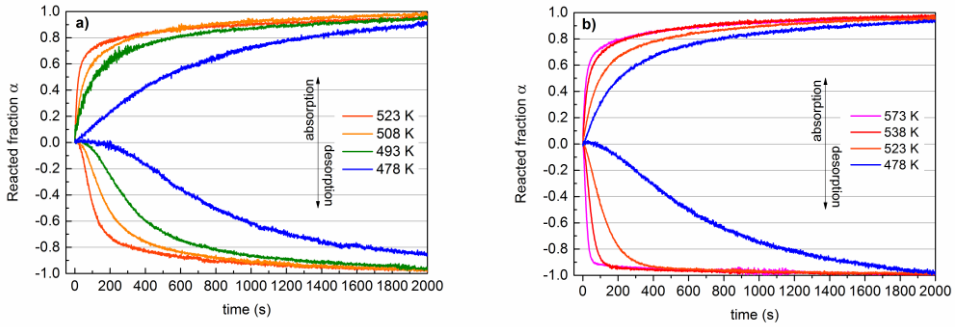

Figure 5.20 H-sorption kinetics on sample MgTi6 measured in order of decreasing temperatures starting (a) from 523 K and then (b) from 573 K. The reacted fraction is normalised between 0 and -1 for desorption.

Table 5.5 Sample MgTi6 energy of activation for H-absorption and desorption obtained from the linear fits in Figure 5.21. E_A values for bulk MgH_2 and MgH_2+Nb_2O_5 are reported for comparison.

E_A (kJ mol^{-1})		Absorption	Desorption
MgTi6	After 523 K	155±11	95±8
	After 573 K	68±8	78±4
Bulk MgH_2 [75]		95÷130	120÷160
MgH_2+Nb_2O_5 [76]		61	-

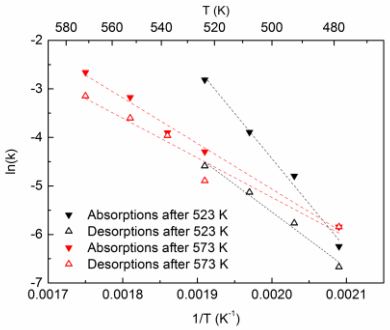

Figure 5.21 Kissinger plot for the kinetics in Figure 5.20 after $T_{max} = 253\ K$ in black, after $T_{max} = 573\ K$ in red, on sample MgTi6.

at different temperatures are shown in the Kissinger plot in Figure 5.21. The activation energy E_A was calculated for the two sets of measurements separately, according to the Arrhenius law $k = k_0 e^{-E_A/RT}$. The values of E_A are compared in Table 5.5 to those reported for bulk MgH_2 [75] and for MgH_2 catalysed with Nb_2O_5 [76]. The two sets of measurements (red and black data) have very different slopes, reflecting different activation energies. After $T_{max} = 523\ K$, E_A values are in the range usually reported for bulk MgH_2 [75] for both absorptions and desorptions, but after $T_{max} = 573\ K$, E_A greatly decreases, reaching 68 kJ mol^{-1} for absorption and 78 kJ mol^{-1} for desorption (Table 5.5). These values of E_A compete with the ones found using Nb_2O_5, one of the best catalyst for H-sorption reactions in Mg known so far[76]. It is suggested that the decrease of E_A after cycling at 573 K is connected to surface activation, which may result from the breaking of the MgO/$Mg(OH)_2$ layers at the NPs surface. The decrease of the rate constant k, observed for H-absorption despite the decreased activation energy, may be due to NPs coarsening and grain growth after cycling at 573 K.

The fitted Avrami parameters n for the first set of cycles are $n_{abs}\ T_{max} = 523\ K\ = (0.9 \pm 0.1)$ for absorptions and $n_{des}\ T_{max} = 523\ K\ = (2.0 \pm 0.1)$ for desorptions. For the second set of cycles the Avrami parameters are $n_{abs}\ T_{max} = 573\ K\ = (1.0 \pm 0.1)$ and $n_{des}\ T_{max} = 573\ K\ = (1.6 \pm 0.3)$.

The differences in the H-sorption kinetics induced after cycling sample MgTi6 at $T_{max} = 523\ K$ and after $T_{max} = 573\ K$ are summarised in the Kissinger plot in Figure 5.21. The Avrami parameters n convey some information on kinetics and geometry of the reaction mechanisms. We recall that $n = a + bc$, where a is related to the nucleation rate and equals 0 when nucleation is instantaneous and 1 when it is constant, b is the dimensionality

D of the growth and c equals 0.5 or 1when the growth is diffusion or interface controlled, respectively. The rate limiting step is generally considered to be the slow motion of H atoms in MgH_2, meaning that absorptions are diffusion controlled ($c = 0.5$) while desorptions are interface controlled ($c = 1$). Since all absorptions have n_{abs}~1, the mechanism could be instantaneous nucleation with 2-D diffusion controlled growth ($a = 0$, $bc = 1$) or decreasing nucleation rate with 1-D diffusion controlled growth (a~0.5, bc~0.5). For desorptions, $n_{des}\ T\_\max = 523\ K\ =\ 2.0 \pm 0.1$ and $n_{des}\ T\_\max = 573\ K\ =\ 1.6 \pm 0.3$. As mentioned before, desorptions are interface controlled, therefore, assuming $c = 1$, n_{des} values are compatible with instant nucleation and ~2-D motion of the interfaces ($a = 0$, b~2) or nearly constant nucleation and 1-D interface motion (a~1, $b = 1$).

Equilibrium measurements and thermodynamic properties

Thermodynamic properties were studied under isothermal conditions using the secondary chamber as a Sievert apparatus for measurements in the 340 K < T < 425 K range and the home-built external Sievert in the 430 K < T < 550 K range.

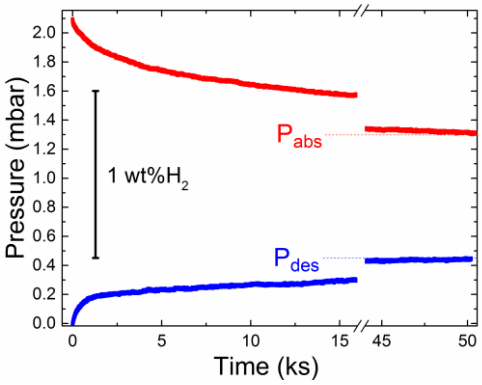

Figure 5.22 Pressure variations measured during the first hydrogen desorption (bottom, blue) and the first hydrogen absorption (top, red) on sample Mg-15Ti at 375 K. The equilibrium values P_{abs} and P_{des} are indicated, as well as the pressure change that corresponds to 1 wt% change due to hydrogen sorption by the sample.

The plateau pressures for hydrogen absorption (P_{abs}) and desorption (P_{des}) were determined at the first absorption or desorption step, respectively, reaching equilibrium. The pressures actually measured would be the knees in a full PCI where absorption and desorption plateaus start. The equilibrium pressure at each temperature was then calculated as the geometric average of P_{abs} and P_{des}

$$P_{eq} = \sqrt{P_{abs} \cdot P_{des}} \qquad (5.3)$$

Figure 5.22 illustrates the typical amount and time scale of pressure variations for sample MgTi15. The time derivative of the pressure decreases rapidly as the pressure rises (desorption) or falls (absorption) from the initial

value towards equilibrium, which is attained in several ks. The phase transformation is not completed after a single step: after restoring the initial values, the pressure restarts to change, approaching the equilibrium. The repetition of several desorption steps permits to construct a full PCI, as represented by the desorption branch in Figure 5.23. Similarly, a series of absorption steps can be done to measure the PCI absorption branch. The low equilibrium pressures and slow kinetics in this temperature range, together with the high storage capacity of the material, call for many lengthy measurements steps to complete a PCI branch. For instance, the PCI in Figure 5.23 took about two weeks to be measured. For this reason, the equilibrium properties were mainly determined by the first absorption/desorption step rather than through full PCIs. The main motivation behind this choice is to limit as much as possible the amount of coarsening and microstructure evolution, which occurs during the measurement themselves, as it will discuss later on.

Qualitatively similar results were obtained on NPs with X_{Ti}=6 and 30 at%. As an example, Figure 5.24 displays the hydrogen sorption curves recorded at 355 K on sample Mg-6Ti. At slightly higher temperatures (see Figure 5.25), since the time required for each step to reach equilibrium is drastically reduced, it is possible to easily measure PCI absorption branches, useful also as a measure of the sample's total capacity; plateau pressures are still too low to completely empty the sample step by step in a desorption branch.

The only exception is sample MgTi60 that exhibits pressure variations an order of magnitude smaller on even slower time scales. These features impeded a reliable determination of its

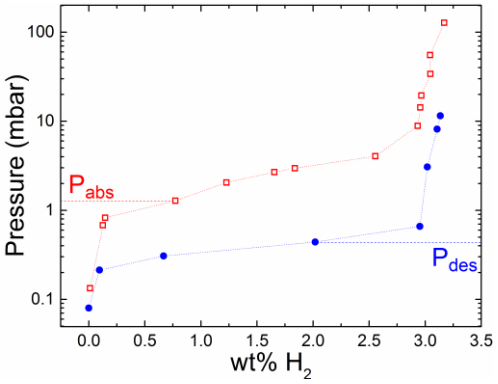

Figure 5.23 Full PCI measured on sample Mg-15Ti at 375 K. The values P_{abs} and P_{des} derived from the curves reported in Figure 4 are indicated. The dotted lines are just a guide to the eye.

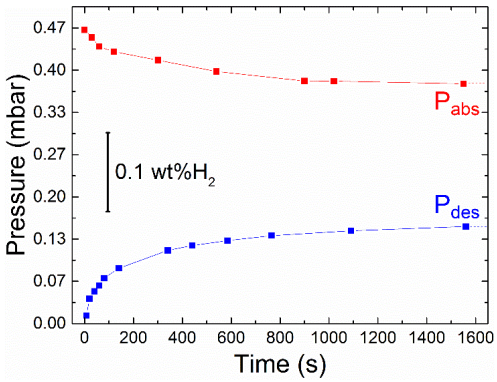

Figure 5.24 Pressure variations measured during the first hydrogen desorption (bottom, blue) and the first hydrogen absorption (top, red) on sample Mg-6Ti at 355 K. The equilibrium values P_{abs} and P_{des} are indicated, as well as the pressure change that corresponds to 0.1 wt% change due to hydrogen sorption by the sample.

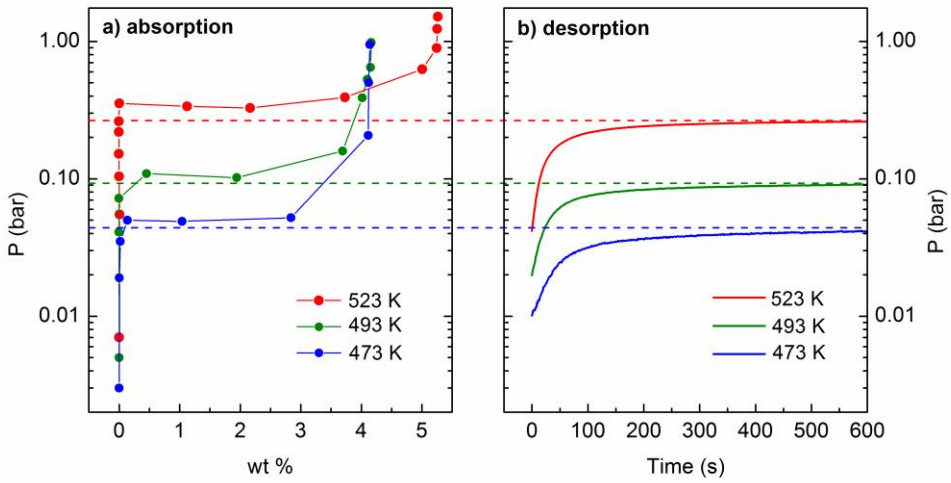

Figure 5.25 (a) PCI absorption branches and (b) pressure evolution of the first desorption steps reaching equilibrium, at different temperatures, on sample MgTi6.

hydrogen sorption properties, which will not be presented. The main causes for this failure are the significantly lower amount of Mg and the higher degree of Mg oxidation, as it was discussed previously. All P_{eq} values measured on Mg-Ti NPs with X_{Ti} in the 6-30 at% range are collected in a single

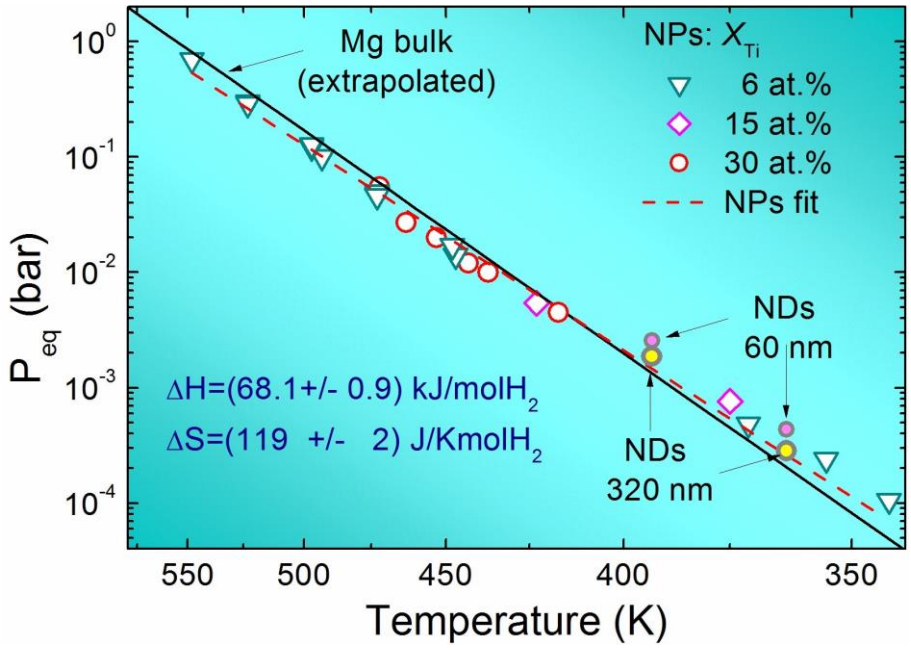

Figure 5.26 van' t Hoff plot of equilibrium pressures P_{eq} *(log scale) versus T (reciprocal scale) measured on NPs samples with Ti content X_{Ti}=6, 15, and 30 at%. The plot reports also P_{eq} values recently measured on Mg/Ti/Pd three-layer nanodots (NDs) with lateral size of 60 and 320 nm*[77]*. The dashed red line is the best linear fit on NPs data only, from which the tabulated enthalpy-entropy values were obtained. The solid black line is an extrapolation of high temperature data on bulk Mg/MgH$_2$* [14].

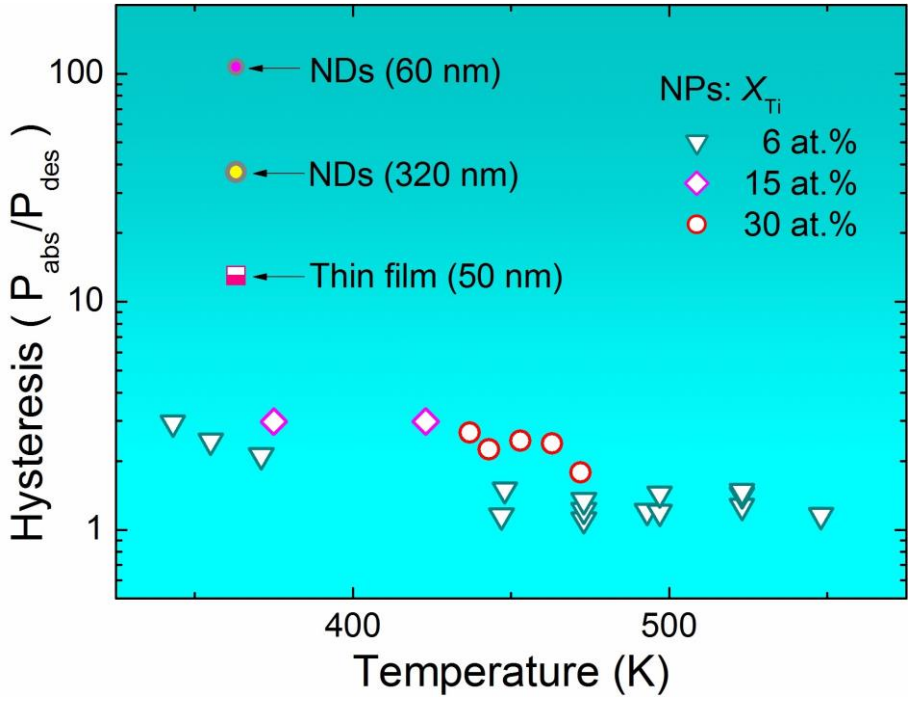

Figure 5.27 Collection of pressure hysteresis values P_{abs}/P_{des} versus temperature measured on NPs samples with Ti content X_{Ti}=6, 15, and 30 at%. The plot reports also values recently measured on Mg/Ti/Pd three-layer nanodots (NDs) with lateral size of 60 and 320 nm [77] and on a quasi-free Mg film 50 nm thick[21].

van 't Hoff plot in Figure 5.26. The data fall reasonably well on a single straight line whose slope and intercept yield the enthalpy and entropy of hydride formation, respectively. The values displayed in Figure 5.26: $\Delta H = 68.1 \pm 0.9\ \mathrm{kJ/mol_{H_2}}$ and $\Delta S = 119 \pm 2\ \mathrm{J/K \cdot mol_{H_2}}$, are both lower compared to literature values for bulk MgH_2 at higher temperature and to the values reported in the previous Section for Mg-Ti pellets. The solid black line is a low temperature extrapolation of bulk MgH_2 data according to ref.[14]. Thermodynamic changes, if any, are found only at T<400 K where the nanostructure is not affected by the thermal treatment and the equilibrium points are slightly higher. Determining if MgH_2 has been really destabilised is a delicate question, the debate on the real or artifact (caused by the fit in the van 't Hoff plot) nature of the observed enthalpy-entropy compensation effect is still open. However, even if the enthalpy change is real, it is too small for any practical application. Figure 5.26 also reports P_{eq} values obtained on Mg/Ti/Pd three-layer nanodots (NDs) by pressure vs. optical transmission isotherms[77]. It is noticed that NDs with lateral size of 320 nm fall almost on the same van 't Hoff plot as the NPs, while 60 nm NDs have slightly higher P_{eq} values. Another interesting parameter to address is the amount of pressure hysteresis that can be quantified by the ratio between

P_{abs} and P_{des}. Figure 5.27 gathers data from all Mg-Ti NPs together with the aforementioned NDs and a Mg thin film (50 nm)[21]. NPs demonstrate a significantly lower pressure hysteresis compared to NDs, caused by the intrinsic absence of constraints on the free NPs.

Effects of Ti addition

The presence of Ti atoms prevents NPs coalescence, a phenomenon that occurs extensively during IGC synthesis of pure Mg like it was demonstrated in Chapter 4. As Table 5.4 shows, the crystallite size of β-MgH_2, representative of the mean NP size, is smaller for the sample with higher Ti content. Grain growth during cycling is also reduced with increasing Ti concentration (see Table 5.4).

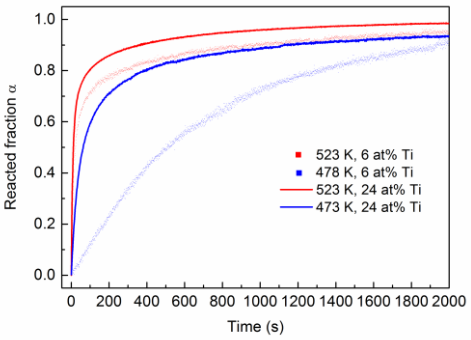

Figure 5.28 Comparison of the reaction kinetics at 523 K and 473 K of sample MgTi6 after $T_{max} = 523\ K$ and sample MgTi24.

In Figure 5.28, the comparison between the absorption kinetics of samples MgTi6 and MgTi24 at 523 K and 473 K shows that the already fast kinetics observed for sample MgTi6 can be further improved increasing catalyst concentration, obviously at the cost of a reduced capacity of the material. As mentioned before, a higher Ti content reduces the NPs size, which is also beneficial for the reaction speed.

The relatively light weight of TiH_2 as a catalyst allows to reach high gravimetric capacities. The capacity measured during the PCIs of sample B was 4.1 wt% at low temperatures (Figure 5.25a) and increases to 5.3 wt% when heated up to 523 K. The increased capacity might be due to activation effects in a portion of the sample, since the PCI at 523 K was chronologically the last one. The theoretical reversible hydrogen capacity C_x of a MgH_2-TiH_2 composite with x at% Ti is calculated by the formula

$$C_x = C_0 \frac{100 - x\ M_{MgH_2}}{100 - x\ M_{MgH_2} + xM_{TiH_2}} \tag{5.4}$$

where $C_0 = 7.66$ wt% is the theoretical capacity of MgH_2, $M_{MgH_2} = 26.32$ g mol^{-1} and $M_{TiH_2} = 49.88$ g mol^{-1} are the molar masses of the hydrides. For

sample MgTi6, the theoretical maximum is $C_6 = 6.83$ wt%, which is higher than the measured value (5.3 wt%). This difference is mainly attributed to oxide formation (Table 5.4) that could be reduced by improving sample transfer and increasing the amount of synthesised material.

After cycling characterisation

The Mg-Ti NPs exhibit a certain degree of microstructure evolution due to hydrogen sorption cycling, which strongly depends on the time/temperature history. Exemplary XRD patterns recorded after hydrogen sorption cycles are presented in Figure 5.29 and the Rietveld analyses are summarised in Table 5.4. The most evident changes are the disappearance of the metastable γ-MgH_2 phase in favour of β-MgH_2 and the coarsening of the β-MgH_2 crystallite size. The lattice parameters of the β-MgH_2 and ε-TiH_2 phases exhibit small relative changes below 0.1% compared to as-prepared NPs. The MgO fraction remains approximately constant below 10 wt% for all samples. STEM investigations provide more detailed and local information on the microstructure evolution and highlight the dramatic influence of the maximum temperature experienced by the NPs. Figure 5.30 illustrates different situations that arise in a sample subjected to 375-423 K cycling. On one side, local coarsening phenomena are observed, which lead to the formation of larger NPs (about 100 nm size) containing Ti-free zones (Figure 5.30a, c). On the other, most NPs maintain the initial morphology and elemental distribution (Figure 5.30b, d), showing good thermal stability in this temperature range on a time window of approximately one month. At

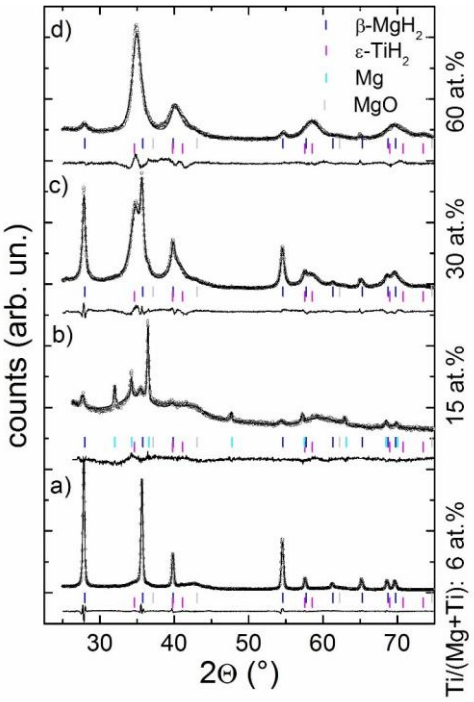

Figure 5.29 XRD patterns of Mg-Ti NPs after hydrogen sorption cycles at elevated temperature. Open circles are experimental data while the calculated Rietveld best fit is represented by the solid line. The fit residual is shown below each pattern, and the coloured vertical bars mark the Bragg reflections of the main crystalline phases. The sample Mg-15Ti (shown in b) underwent a hydrogen desorption at 423 K before XRD analysis and therefore metallic Mg overwhelms MgH_2. For the other samples, the last step was hydrogen absorption and therefore metallic Mg is not detected.

higher temperatures, coarsening phenomena and spectacular morphological changes become dominant. Figure 5.31 highlights two typical features:

i. large Mg NPs, several hundreds of nm in size, where Ti is not uniformly distributed but concentrated in localized spots (Figure 5.31a, c), and

ii. small NPs with size similar to the initial state, but internally depleted from Mg resulting in a nearly hollow morphology (Figure 5.31b, d). Only few NPs with size and morphology similar to as-prepared NPs can be detected after cycling in this temperature range.

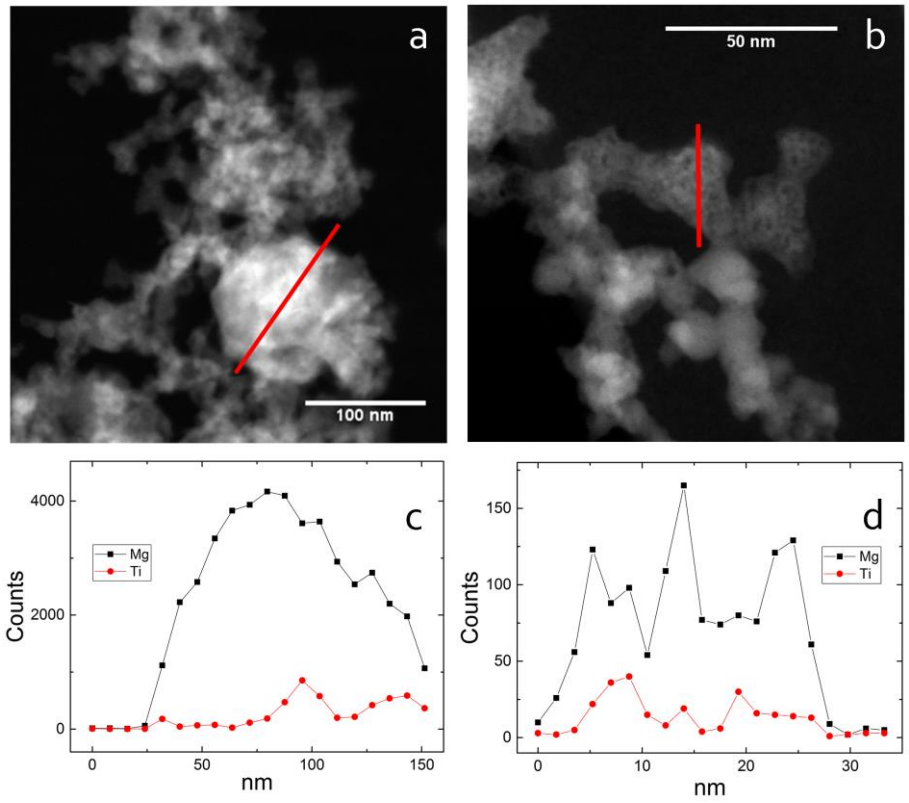

Figure 5.30 HAADF-STEM images of MgTi6 NPs subjected to hydrogen sorption cycles up to T=523 K; c and d represent the STEM-EDX line scans taken along the red lines in a and b, respectively.

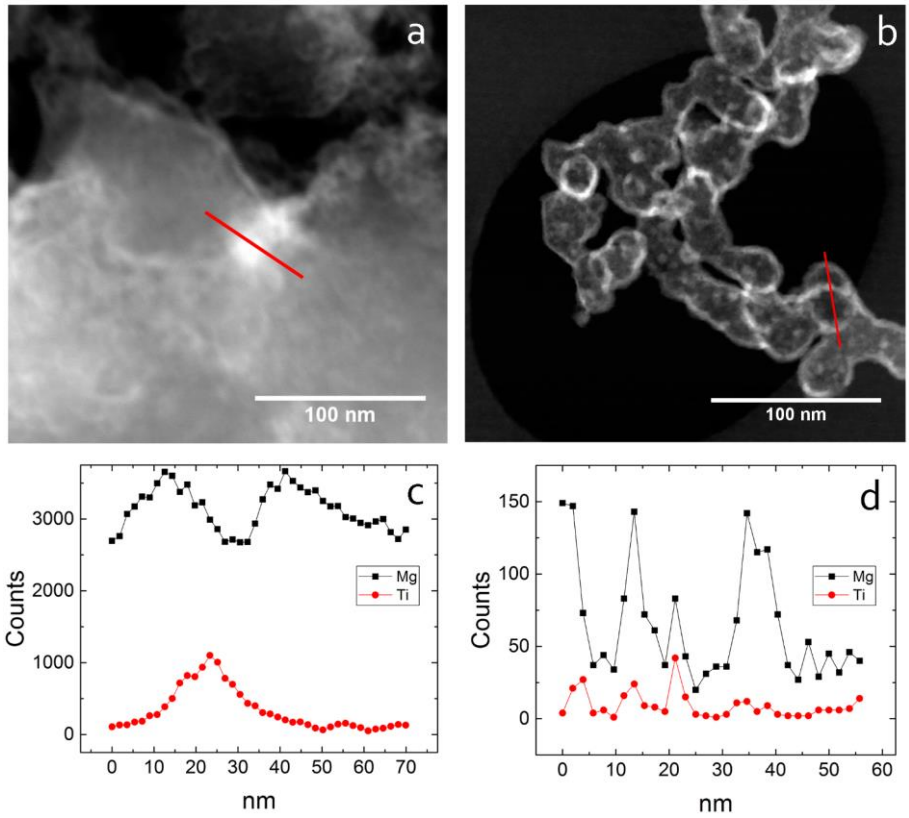

Figure 5.31 HAADF-STEM images of MgTi6 NPs subjected to hydrogen sorption cycles up to T=523 K; c and d represent the STEM-EDX line scans taken along the red lines in a and b, respectively.

Conclusions

Mg-Ti NPs were synthesised both via Inert and Reactive Gas Condensation. After the very first contact with H_2, during evaporation for RGC or during the *in situ* treatment for IGC, the Mg-Ti NPs turn into a MgH_2-TiH_2 nanocomposite.

In situ SR-XRD revealed that the ongoing reaction during H-sorption is the transition between the metallic and the hydride phase of Mg, while TiH_2 acts as a spectator. The enthalpy and entropy of formation were measured, $\Delta H = 68.1 \pm 0.9$ kJ $\mathrm{mol}_{\mathrm{H_2}}^{-1}$ and $\Delta S = 119 \pm 2$ J K^{-1} $\mathrm{mol}_{\mathrm{H_2}}^{-1}$, both slightly lower than MgH_2 bulk values, starting from data scattered in the Van 't Hoff plot over a very wide, low temperature range, between 340 K and 550 K. H sorption measurements at such low temperatures were possible thanks to the outstanding kinetic properties of these NPs. Even a relatively small Ti addition (~6 at%) is sufficient to greatly enhance the H-sorption kinetics, while keeping a high storage capacity, up to 5.3 wt%. The combination of the nanostructure of Mg and the presence of TiH_2 allowed to cycle

the samples in ~2000 s at 473 K. On cycling at higher temperatures (573 K) the activation energy for both absorption (68 kJ mol^{-1}) and desorption (78 kJ mol^{-1}) is reduced owing to surface activation effects. Increasing Ti content (~24 at%) still yields a MgH_2-TiH_2 nanocomposite with reduced grain growth during synthesis and cycling and slightly improved reaction speed, but at the cost of a reduced capacity.

6 TiO_2-BASED NANOPARTICLES

In this final chapter will be described the research carried out on a completely different type of material, titanium dioxide, TiO_2, with the addition of vanadium, V. The materials studied are in the form of nanoparticles, synthesised via gas condensation; this technique once again has proved to be very versatile and efficient in the synthesis of nanoparticles with non-trivial compositions.

In the next Section is motivated the interest in TiO_2-based materials and the general properties of TiO_2 are resumed while in Section 6.2 is presented the experimental work on V-doped TiO_2 nanoparticles.

6.1 TiO_2 for photocatalysis

Titanium dioxide, or titania, is probably one of the most studied materials of the last decades because of its wide range of applications, like superhydrophilic coatings, titanium-bone implant fixation, cleaning of polluted waters and air, photoelectrolysis of H_2O in pure H_2 and O_2 and of course dye-sensitised solar cells. Most of these applications arise from the highly efficient photocatalycity of TiO_2, combined with other properties like chemical stability at high temperatures or in wet environments, biological compatibility and cost-effectiveness. The nanoparticle morphology is one of the most desirable morphologies for these kind of applications as it will be explained in the following subsections.

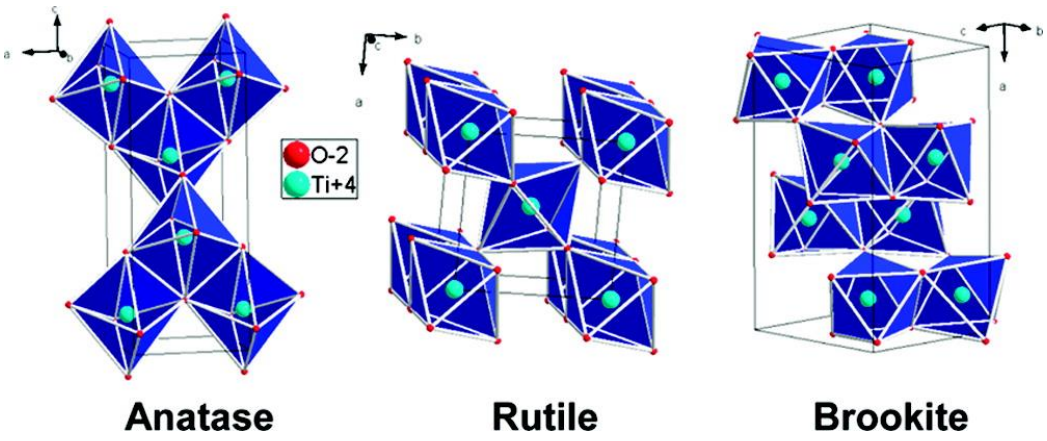

Figure 6.1 Representations of the TiO_2 anatase, rutile, and brookite forms. Highlighted in blue are the TiO_6 octahedra.[117]

Structural properties

The most common phases of TiO_2 that can be also found in nature as minerals are rutile, anatase and, in the third place, brookite. Many other polymorphs exist[78–83], synthesised at extreme pressure and/or temperature conditions artificially or in meteorite impacts. The general interest is mainly focussed on rutile and anatase, since they have greater photocatalytic activity.

Rutile is the most thermodynamically stable TiO_2 phase at ambient conditions. It has a tetragonal structure (space group $P4_2/mnm$) where each Ti atom is coordinated with 6 O atoms arranged in a slightly distorted octahedron.

The anatase structure is tetragonal, (space group $I4_1/amd$), composed of TiO_6 octahedra too, but more distorted and stacked with a different geometry, resulting with a density about 9% lower compared to rutile[84].

Brookite has an orthorhombic crystalline structure (space group *Pbca*), in the TiO_6 octahedra the Ti-O bond lengths are all different. Octahedra arrangement produces a crystalline structure with tunnels along the c-axis, in which small cations like hydrogen or lithium can be incorporated[85].

In the synthesis of TiO_2 nanoparticles, often the initial structure is amorphous and crystallisation of the above mentioned structures is induced by annealing in air at temperatures >200 °C.

The size dependence of the stability of various TiO_2 phases has been reported[86]: rutile is the most stable phase for particles above 35 nm in size, anatase is the most stable phase for nanoparticles below 11 nm, brookite has been found to be the most stable for nanoparticles in the 11-35 nm range.

However, other works as well as the one presented in this Thesis do not agree with these results, leaving the discussion still open. As it often happens when it comes to nanoparticles, it is difficult to set general rules because many factors like synthesis conditions and technique strongly influence the outcome.

As stated at the beginning of this Chapter, having the material composed of nanoparticles is optimal for photocatalytic applications because the nanometric scale allows the photogenerated charges to easily reach the surface where the redox events take place (steps C and D of Figure 6.3) and the high surface-to-volume ratio, like for any normal catalyst, improves its efficiency.

Electronic and catalytic properties

Titanium oxide is a n-type, wide band gap semiconductor. Its n-type nature arises from the formation, at standard conditions, of intrinsic n-type defects, *i.e.* O vacancies and Ti interstitials.[87] In most conventional semiconductors, such as Si and Ge, covalent bonding dominates. In general, the bonding in metal oxide semiconductors is very different in nature. Since O has a much higher electronegativity than Ti, the valence electrons are fully transferred from the oxygen to the metal ion, forming an ionic bond.

The electronic band structure and DOS of rutile TiO_2 are shown in Figure 6.2. The valence band is mainly composed of O-2p orbitals, whereas the

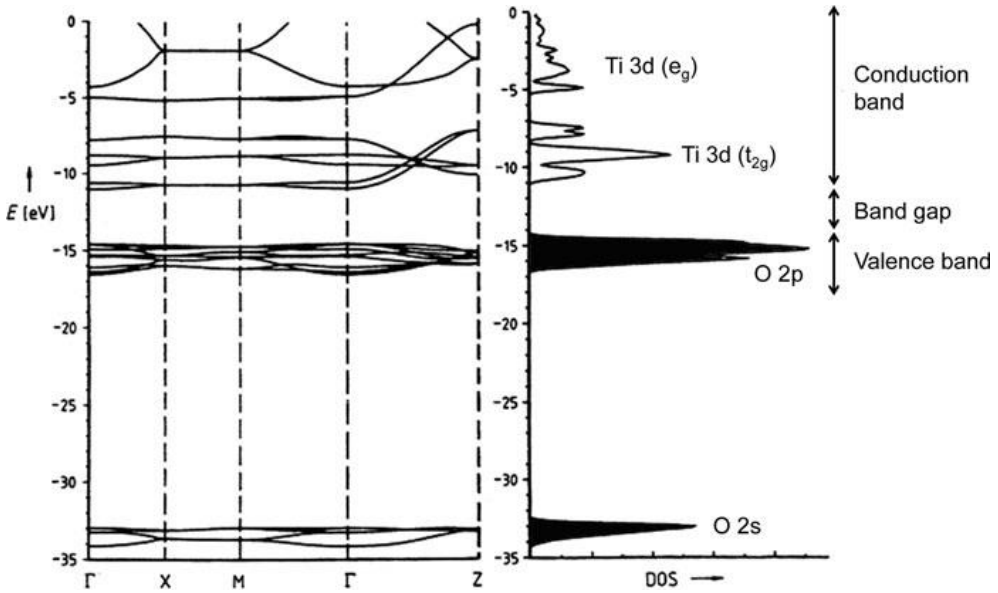

Figure 6.2 Calculated electronic band structure and density-of-states (DOS) of rutile TiO_2. The black parts of the DOS indicate completely filled bands.[118]

conduction band is primarily Ti-3d in character. One could think of the valence band as being occupied with the electrons that originally resided on the titanium atoms, before they were transferred to the more electronegative oxygen during the formation of the bond. This local view is a key feature that distinguishes metal oxide semiconductors from their covalently bonded counterparts. For example, electrons in the conduction band that usually considered as free, may be localised on a Ti cation that is then considered as a Ti^{3+} species even in the bulk, far from the surface, where the electronic structure is not distorted. Anatase is usually considered to have an *indirect* band gap, while rutile and brookite have a *direct* one, however the horizontal-running *E-k* lines in their band structure (see Figure 6.2) obscure the direct vs. indirect nature.[88]

As said at the beginning of this subsection, TiO_2 has a wide band gap; it is different for each phase: the band gap is 3.0 eV for rutile, 3.2 eV for anatase and values from 3.1 to 3.4 eV have been reported for brookite. Anatase is the most active photocatalyst because charge carriers for photocatalytic reactions can originate from much deeper below the surface for anatase than for rutile[89], despite the slightly larger band gap. Pure brookite is rather difficult to be prepared so that its photocatalytic properties have not been much studied, but recently, brookite also has showed to be an interesting candidate for photocatalytic applications.[90]

6.2 V-doped TiO_2 nanoparticles

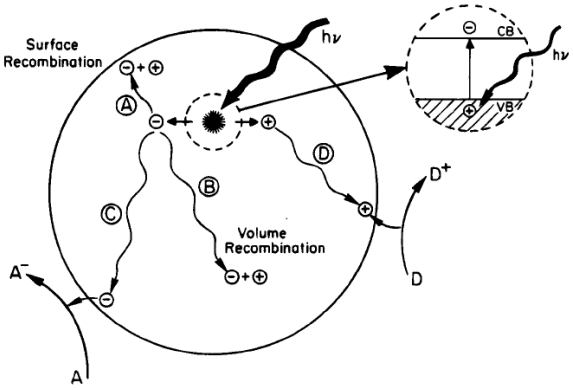

Figure 6.3 Schematic photoexcitation in a solid followed by deexcitation events. Surface (A) or volume recombination (B) of the photogenerated electron-hole pair, reduction of an electron acceptor (C) and oxidation of a donor (D).[119]

Because of the TiO_2 wide band gap, only a small fraction of the solar spectrum, *i.e.*, UV light (3–5% of total), can be used for photocatalytic processes. The incorporation of 3d-transition metals in TiO_2 is an effective approach to decrease t

he band gap and to improve visible-light photocatalytic activity.[91] Band gap reduction is the result of the creation of states in the band gap of the matrix, as systematically investigated theoretically by Umebayashi *et al.*[92] They found that V, Cr, Mn, Fe, and Co create donor states, their position shifting toward the valence band with increasing atomic number; V, the subject of the present work, was predicted to create a gap state near the bottom of the conduction band. Another route for band gap reduction is N doping, which induces acceptor states above the valence band maximum.[93] Clearly, photocatalysis is due to more complex processes than just light absorption, many of which are crucially linked to dopant sites. In fact, dopants may induce charge carrier recombination (steps A and B of Figure 6.3) or scattering (which lead to reduced efficiency) or may trap charge carriers for long time intervals near the surface of NPs, making them available for oxidation and reduction processes (leading to improved efficiency). Therefore, a detailed atomistic knowledge of the charge dynamics involving defect sites is of paramount importance for a physical understanding of the material's function and may lead to knowledge-based device engineering. For the reasons explained so far, it is important to report in-depth study of V-doped TiO_2 NPs, characterising the overall, as well as local, structure, morphology and optical properties.

Sample preparation

For the growth of V-doped TiO_2 nanoparticles, Ti powders (99.9% purity, -50 mesh, Alfa Aesar) and V powders (99.5% purity, -325 mesh, Alfa Aesar) were gently mixed and loaded in one crucible. The Ti–V phase diagram[94] indicates complete miscibility above the temperature of 882 °C, which corresponds to the *hcp* $\rightarrow$ *bcc* structural transition in pure Ti. In order to obtain a Ti–V alloy precursor, the powder mixture was first heated under vacuum above the melting point of Ti (1668 °C) and then rapidly cooled down to about 1200 °C where no measurable evaporation takes place and left to homogenise for 2 h. Afterward, He was admitted in the chamber at a flow rate of 65 ml_n/min, keeping the pressure constant at 270 Pa. The temperature of the W crucible was slowly increased to attain the desired deposition rate.

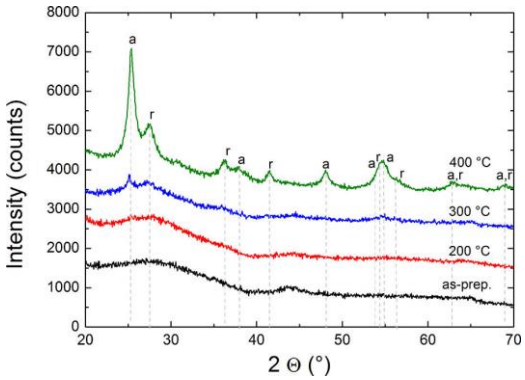

Figure 6.4 XRD patterns of a nanopowder sample with 8 at% V subjected to 6 h annealing at different temperatures. The Bragg reflections of anatase (a) and rutile (r) TiO_2 are indicated. The different patterns are vertically shifted for the sake of clarity.

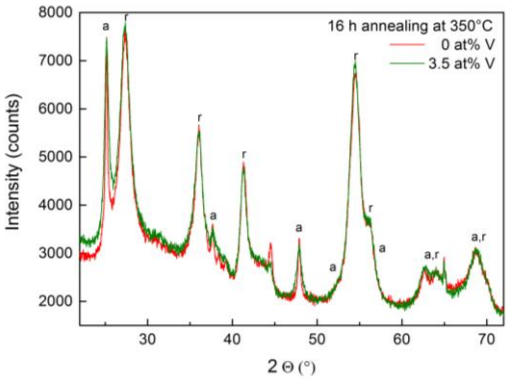

Figure 6.5 XRD pattern of a nanopowder sample with 3.5 at% V superimposed to a sample without V addition. Both samples were annealed for 16 h at 350 °C.

Both nanopowder collection on the rotating cylinder and deposition on substrates experiments were performed for this class of materials and the type of sample will be specified as the results will be presented. After the deposition, high vacuum was restored in the chamber, and finally the nanoparticles were oxidized by admitting O_2 up to a final pressure of 2.6 kPa.

Typically, the V content in the samples determined by EDX was about 4 times lower than in the precursor alloy, due the lower vapour pressure of V compared to Ti in the Ti–V alloy. In the following, the V content will be given by an atomic percentage (at%), obtained dividing the number of V atoms by the total number of Ti plus V atoms (i.e., not counting O atoms). For instance, 4 at% V corresponds to an overall composition of $Ti_{0.96}V_{0.04}O_2$.

Crystalline samples were prepared by annealing the as-deposited nanoparticle-assembled films.

Structural characterisation

The as-deposited samples were structurally amorphous and became crystalline after annealing in air at sufficiently high temperature. The structural evolution of a sample with 8 at% V after an annealing time of 6 h at different temperatures is shown by XRD patterns in Figure 6.4. Bragg reflections of anatase (a) and rutile (r) TiO_2 began to appear after annealing at 300 °C, while full crystallization was induced by annealing at 400 °C. Bragg reflections attributable to metallic vanadium, vanadium oxides or any other V-containing phases were not detected. As it can be clearly seen in Figure 6.5, the raw XRD patterns of a nanopowder with 3.5 at% V annealed for 16 h

at 350 °C perfectly matches the pattern of a Ti-only nanopowder that underwent the same annealing treatment. For these samples, Rietveld refinement determines a mean crystallite size $d_a = 34 \pm 4$ nm for anatase and $d_r = 8.1 \pm 1.0$ nm for rutile. The higher rutile to anatase ratio observed in Figure 6.5 compared to Figure 6.4 is due to the longer annealing time, that favours the crystallisation of rutile.

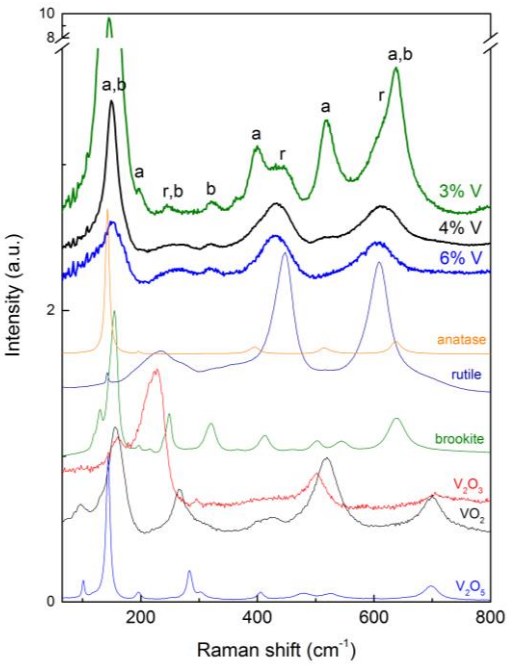

Figure 6.6 Raman spectra of V-TiO_2 nanopowders with V content between 3 and 6 at% annealed at 400 °C for 6 h. For comparison, the spectra of TiO_2 polymorphs and vanadium oxides are also shown.

V-TiO_2 nanopowders were also investigated by Raman spectroscopy with a Renishaw inVia confocal Raman microscope using a 532 nm laser, thanks to a collaboration with LMER - EPFL, Sion, Switzerland. The spectra of samples with V content between 3 and 6 at% annealed at 400 °C for 6 h are shown in Figure 6.6. In the 3 at% V sample, the main peak at 147 cm^{-1} belongs to anatase; the other anatase peaks at 195 cm^{-1}, 400 cm^{-1}, 515 cm^{-1} and 635 cm^{-1} are also clearly visible, highlighted with an "a" in the plot. Less intense rutile and brookite bands are also detected, marked respectively "r" and "b" in the plot. At 4 and 6 at% V the rutile to brookite intensities ratio does not change while the anatase signal drastically decreases, almost vanishing at 6 at% V. This effect is not ascribed to the changing V content, too dramatic over such small concentration variations, but rather to different deposition rates. The anatase-rich sample (with 3 at% V) was deposited at a rate of 0.49 mg min^{-1}, for the anatase-poor sample (with 6 at% V) instead the deposition rate was 18.45 mg min^{-1}. A slower deposition rate correlates with smaller NPs, as it will be deducted in the following electron microscopy study, where anatase is most stable.

Raman spectroscopy is a much more phase-sensitive technique than XRD, in fact in addition to anatase and rutile, it is able to detect also brookite traces in the samples. Therefore, the absence of vanadium oxides signatures

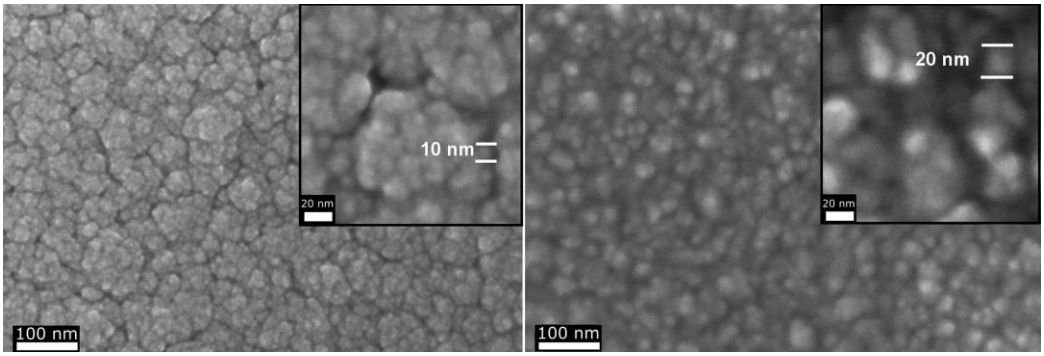

Figure 6.7 FESEM images of V-doped TiO_2 nanoparticle-assembled films on silicon substrates: samples with 3.5 at% (a) and 4.4 at% V (b) both annealed at 400 °C for 15 h. The insets on the top-right corner are the same samples taken at higher magnification. The typical NP sizes in the two samples are indicated.

in XRD and Raman spectra allows to definitively rule out their presence in V-TiO_2 NPs.

Single NP structure

The morphology of both as-deposited and crystalline nanoparticle-assembled films on silicon substrates was examined by FE-SEM and HR-TEM. Figure 6.7 displays the morphology of annealed samples with 3.5 at% (a) and 4.4 at% V (b) at different magnifications. The NPs assemble in large agglomerates with a size of several tens of nanometers. Primary NPs with a typical diameter in the 10–20 nm range can be easily recognized within the agglomerates. The 4.4 at% V sample, deposited at 1.9 nm min^{-1}, exhibits a larger NP size compared to the 3.5 at% V one, deposited at 1.4 nm min^{-1}. This suggests that the NP size coarsens with increasing evaporation/deposition rate, a phenomenon commonly observed in gas-phase condensation[95].

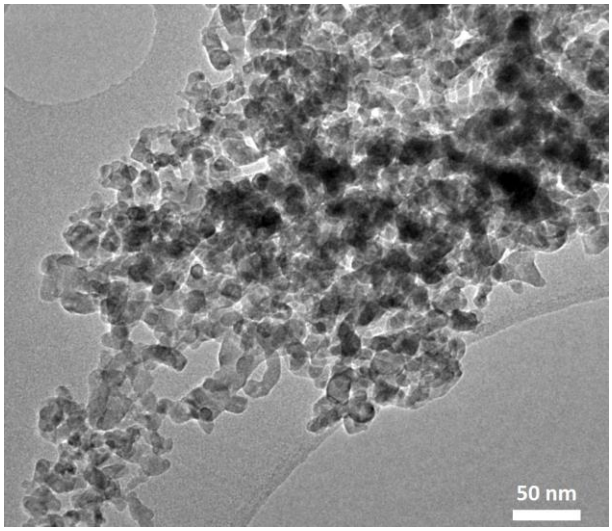

Figure 6.8 TEM image of 3.5 at% V-doped TiO_2 nanoparticles annealed at 400 °C for 15 h.

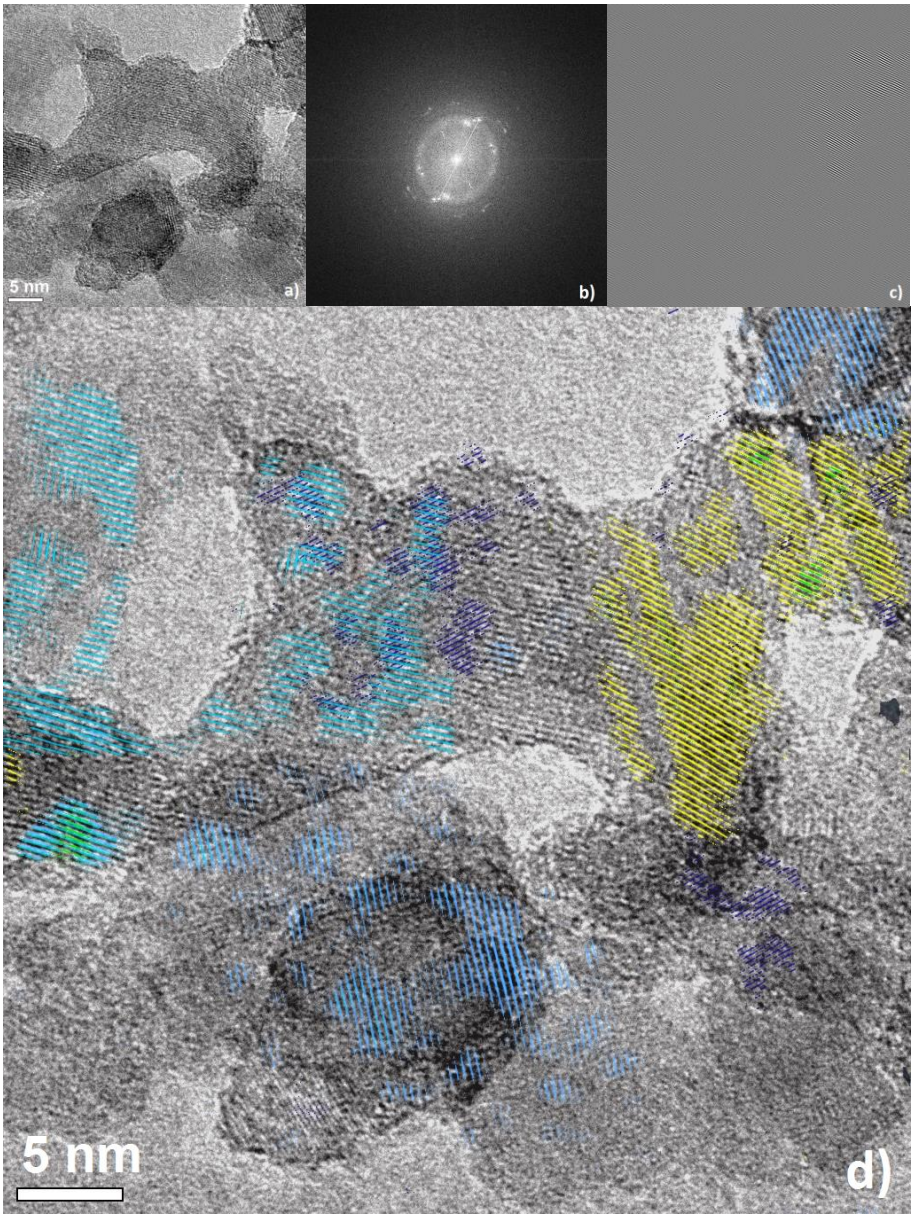

Figure 6.9 Steps needed for creating a "crystallographic map": (a) the original HR-TEM image, (b) the Fourier transformed of the original image, (c) the inverse Fourier transform after filtering. (d) The final map, where blue and light blue areas indicate the presence of different anatase orientations, while yellow and green indicate presence of brookite.

The NP size influences the relative anatase/rutile phase abundance, as it will be shown in the next sections. FE-SEM also revealed that annealing at 400 °C did not induce any significant coarsening of the nanoparticles but from HR-TEM images in Figure 6.8 can be seen that after the annealing the nanoparticles are sintered.

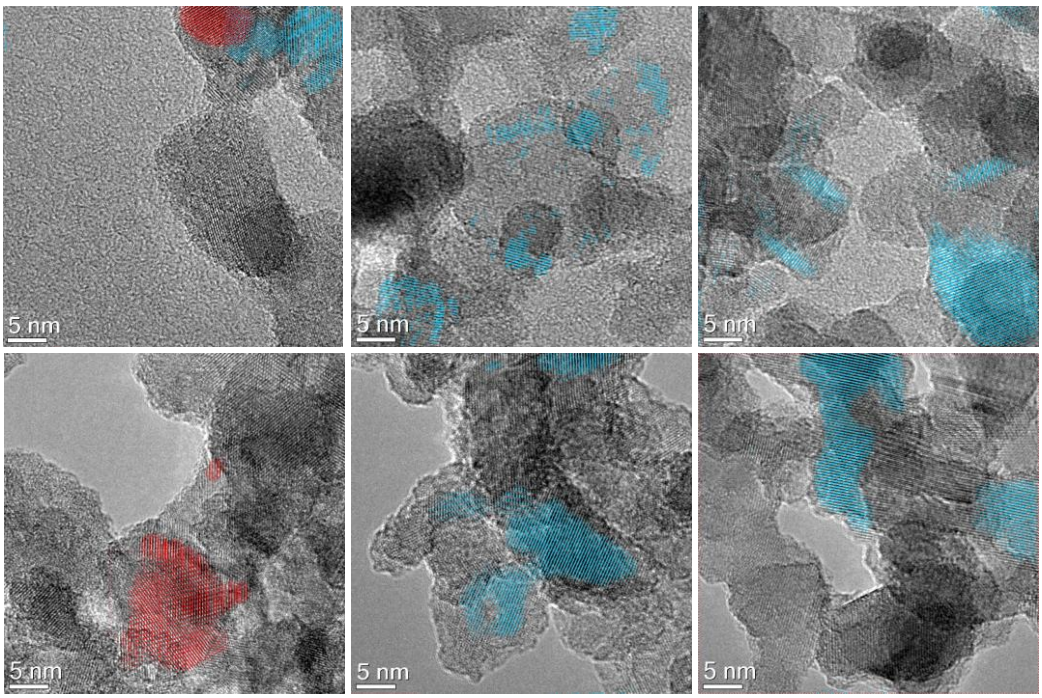

Figure 6.10 Crystallographic maps obtained like Figure 6.9d. Here the blue and red areas correspon to anatase and rutile phases, respectively.

A study of the distribution of the crystallites in the nanoparticles was conducted on the 3.5 at% V sample, whose nanoparticles, dispersed in ethanol, were drop-cast on a holey carbon TEM grid. From HR-TEM images at high magnification it is possible to produce coloured maps of the crystalline structures observed. By taking the Fourier transform of the whole picture (Figure 6.9b) then filtering everything but the two centrosymmetric peaks that correspond to a series of parallel planes of a particular phase and then taking the inverse Fourier transform (Figure 6.9c), it is possible to isolate one crystal orientation at a time. Colouring the filtered images and superimposing them on the original one gives the "crystallographic maps" (Figure 6.9d). The measure of interplanar distance reveals whether the phase isolated is anatase, rutile or brookite. This procedure has been followed for many HR-TEM images on different spots, showed in Figure 6.10. Even if the images are not completely mapped, the crystallite size is clearly the same as the nanoparticle size, the nanoparticles are single-phase.

Optical properties

Crystallisation was accompanied by a marked change in the color of the samples as shown in Figure 6.11: nanopowders turned from nearly black to

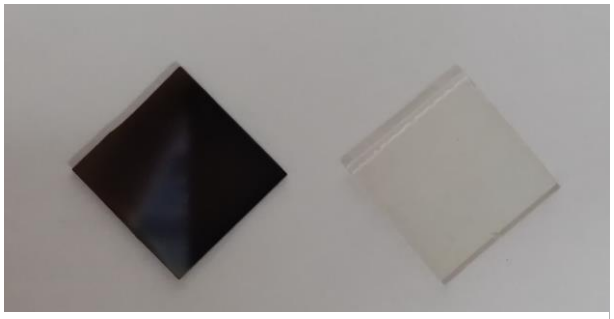

Figure 6.11 Picture of the nanoparticle-assembled films deposited on glass, as deposited on the left, after annealing on the right.

Figure 6.12 Annealed TiO_2 nanopowders with increasing V content from left (0 at%) to right (6.6 at%).

orange, while films deposited on glass gained a yellowish transparency. Figure 6.12 shows the colour change correlated to the V-doping: from white to dark brown as the V content increases. In order to assess the effect of V-doping on the optical properties of crystalline V-TiO_2, we measured UV–vis diffuse reflectance (DR) spectra. For these experiments, we used a small amount of nanopowder, scraped from the substrate holder after evaporation and annealed under the same conditions as the nanoparticle-assembled films. The DR spectra were collected by a PerkinElmer Lambda 45 double beam spectrophotometer equipped with an RSA-PE-20 integrating accessory (Labsphere).

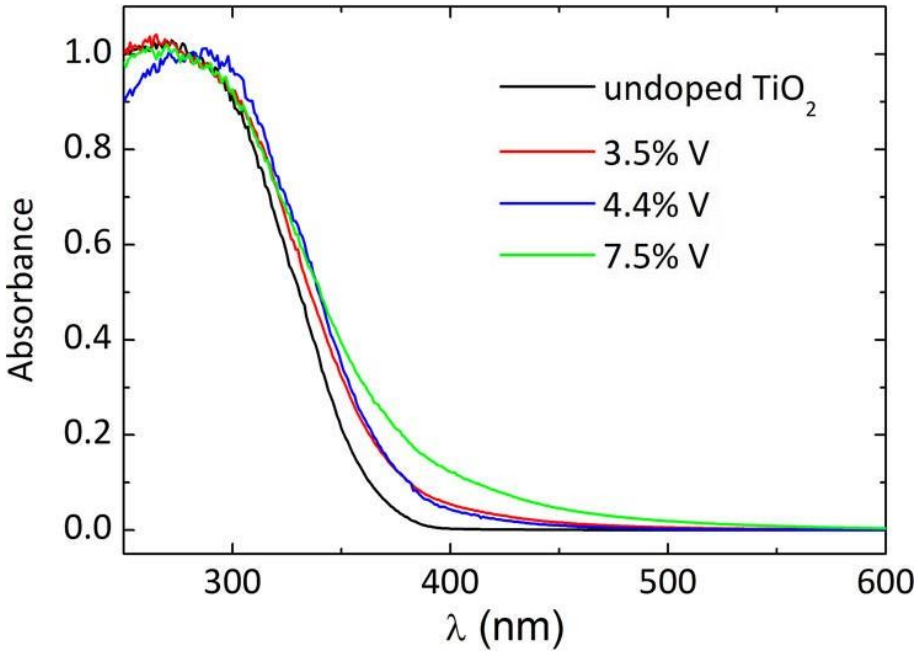

Figure 6.13 UV–vis absorbance of annealed V-doped and undoped TiO_2 NPs, obtained by applying the Kubelka–Munk function to DR spectra and normalised to unit value at 280 nm.

The samples were measured as solid mixtures in a matrix of ground NaCl. Prior to measurement, a blank of pure NaCl was recorded as a reference. To test the suitability of NaCl for its employment in the UV region, a spectrum of the blank was recorded against the $BaSO_4$ reference (100%R) and did not show any strong absorption band in the investigated interval, thus assessing the reliability of the measurement in the interval 200−1100 nm. DR spectra were converted into absorbance by the Kubelka−Munk function, and the band gap of the samples was estimated by applying the Tauc method[96]. Figure 6.13 displays the absorbance of V-doped crystalline samples compared to an undoped sample, which was prepared under the same conditions using pure Ti as precursor. Figure 6.13 shows that V-doping induces a shift of the absorption band edge toward longer wavelengths. In addition, V-doped samples exhibit an absorption tail that extends above 500 nm. These two features are very similar in the samples with 3.5 and 4.4 at% V, a similar V content, while they are stronger for the sample with the highest V-doping.

Accordingly, the Tauc analysis yields a band gap of 3.18(3) eV for the undoped sample, 2.98(3) eV at 3.5 at% V, 3.01(3) eV at 4.4 at% V and 2.81(3) at 7.5 at% V. The V-induced shift of optical absorption features toward the visible-light region fully agrees with previous studies[91,97–100], which attribute it to V incorporation in the TiO_2 structure.

X-ray Near Edge Absorption Spectroscopy

Hard XANES measurements at the Ti and V *K*-edges were performed at the BM2345 beamline of the ESRF in Grenoble, France using a double bounce flat crystal Si(111) monochromator. Reference samples (Ti and V oxides) were measured in the transmission mode using finely ground powders dispersed in polyethylene; samples were measured in the fluorescence mode using a Vortex Si drift diode detector placed in the horizontal plane at right angles to the impinging beam. Soft XANES measurements at the Ti and V $L_{2,3}$-edges were performed at the BACH46 beamline of Elettra, in Trieste, Italy. In this case, all spectra were collected in the total-electron-yield (TEY) mode, by measuring the drain current from the sample to ground.

For all XAS measurements, nanoparticle-assembled films were deposited on super smooth (111) Si substrates (Agar scientific, surface finish roughness <1 nm) at room temperature. The film thickness, determined by the calibrated quartz microbalance and checked by atomic force microscopy, was about 240 nm for all samples. In Table 6.1 is reported, along with the sample

Table 6.1 V content, deposition rate, and annealing treatment of the V-doped TiO_2 nanoparticle-assembled films numbered from 1 to 8; all annealing times are 15 h. The remaining samples are commercial reference materials. Types of XANES measurements performed at Ti and V edges are also summarised.

Sam-ple	V/V+Ti (%)	Deposition rate (nm/min)	description	XANES edges
1	3.5 ± 1.0	1.4	as-deposited	*Ti K, V K*
2	3.5 ± 1.0	1.4	annealed at 400 °C	*Ti K, V K*
3	4.4 ± 1.1	1.9	as-deposited	*Ti K, V K*
4	4.4 ± 1.1	1.9	annealed at 350 °C	*Ti K, V K*
5	4.4 ± 1.1	1.9	annealed at 400 °C	*Ti K, V K*
6	7.5 ± 0.9	1.6	annealed at 400 °C	*Ti K, V K*
7	8.0 ± 1.2	1.6	as-deposited	*Ti $L_{2,3}$, V $L_{2,3}$*
8	8.0 ± 1.2	1.6	annealed at 400 °C	*Ti $L_{2,3}$, V $L_{2,3}$*
m	-	-	Ti metal reference	*Ti K*
a	-	-	anatase reference	*Ti K*
r	-	-	rutile reference	*Ti K*
V_2O_5	-	-	reference	*V K*
VO_2	-	-	reference	*V K*
V_2O_3	-	-	reference	*V K*

characteristics, the XANES measurements and data analysis performed on the various samples, distinguishing between *K* and $L_{2,3}$-edges.

Local Environment of Ti in TiO_2 Nanoparticles: The Host Matrix

In Figure 6.14 is reported the pre- and main-edge regions of the Ti *K*-edge XAS spectrum of the samples. By inspection of this data and comparison with the literature[101–106], the following qualitative comments can be made.

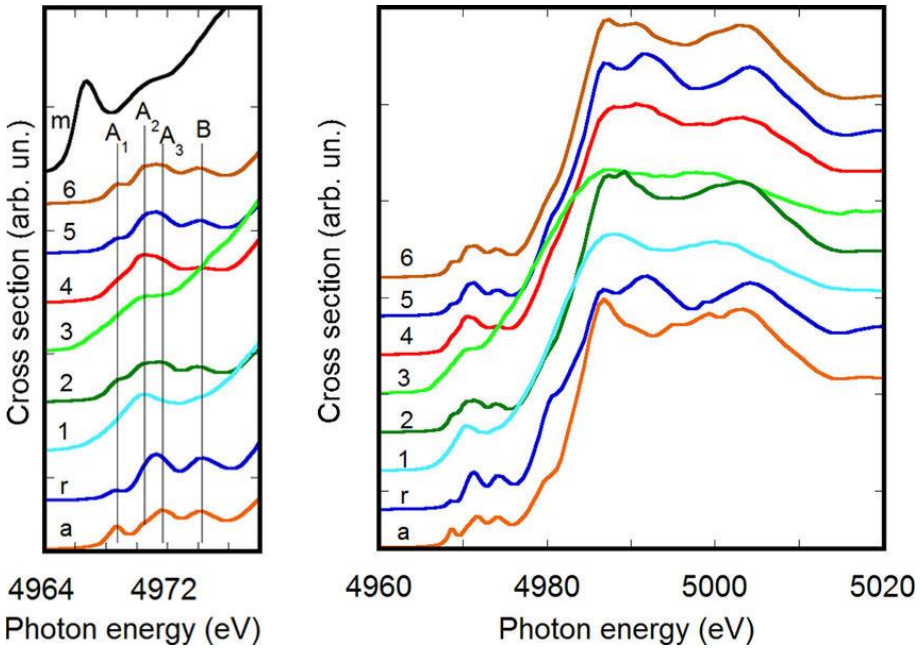

Figure 6.14 Pre-edge (left) and main edge (right) region of the Ti K-edge XAS in the samples and selected reference compounds.

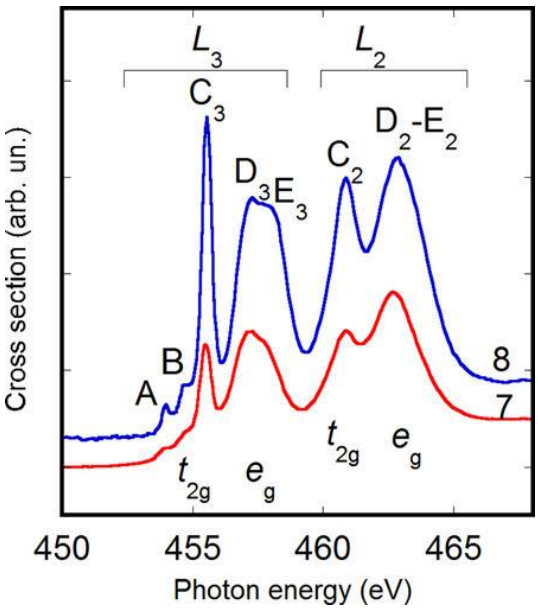

Figure 6.15 Ti $L_{2,3}$-edge XAS spectra for as-deposited sample 7 and annealed sample 8.

The as-deposited samples 1 and 3 exhibit a very broad line shape in both the pre- and main-edge regions; the onset of the main edge is significantly shifted toward low energy. These observations indicate that these samples are highly disordered and may contain a fraction of metallic Ti.

Annealed samples exhibit lineshapes reminiscent of crystalline rutile or anatase. Sample 4, which was annealed at 350 °C, has broader features compared to the others, indicating a poorer degree of ordering. The remaining samples, annealed at 400 °C, exhibit lineshapes that are never identical to rutile or anatase; however, it is noted that sample 2 is more similar to anatase and sample 5 to rutile. This observation suggests that a lower deposition rate, which results in smaller primary NPs, favours the crystallization of anatase. In fact, anatase has a lower surface energy compared to rutile, and therefore its formation is preferred at lower nanoparticle sizes[107]. Sample 6 has pre-edge features similar to rutile but an intermediate main edge line shape. In all these cases the A_2 pre-edge component is more intense than in crystalline oxides; this indicates the presence of under-coordinated, 5-fold, Ti ions. Based on these results, it is suggested that the V content in the explored range has no or little influence on the relative anatase/rutile phase abundance, which appears to depend mainly on the deposition rate and nanoparticle size.

The qualitative observations deduced from the Ti *K*-edge spectra are confirmed by $L_{2,3}$-edge ones. In Figure 6.15 are reported such spectra for samples 7 and 8, respectively, as-deposited and annealed at 400 °C; features related to the L_3- and L_2-edges and to transitions to t_{2g} and e_g orbitals are indicated, and individual peaks are labelled as in previous papers[101,108]. Annealing clearly induces a sharpening of spectral features also of the *L*-edge spectra, a result of greater ordering. The line shape of the sample 8 spectrum is intermediate between those of rutile and anatase reported in the literature;

specifically, the features labelled D_3 and E_3 are approximately of the same intensity, while the former is significantly higher than the latter in anatase and the reverse occurs in rutile[101,109]. This confirms that these NP samples exhibit a local structure intermediate between rutile and anatase.

Local environment of V dopants in TiO_2 nanoparticles

XAFS spectra at the V *K* and $L_{2,3}$-edges were measured with the aim of determining the incorporation site of V in the TiO_2 NPs. At the *K*-edge, good quality XANES spectra were recorded despite the overlap of the Ti K_β and V K_α fluorescence lines. These spectra, along with those for V_2O_3, VO_2, and V_2O_5 reference compounds, are reported in Figure 6.16; the oxides are plotted in order of increasing oxidation state of V from bottom to top (3+, 4+, and 5+), recalling the relation between energy of spectral features and oxidation state[106,110–112]. The rutile and anatase spectra shifted by +500 eV (energy difference between V and Ti *K*-edges) are also report as a comparison. In Figure 6.17 the derivatives of the spectra for annealed samples and reference compounds are reported, to allow a more detailed comparison.

First, it is noted that as-deposited samples 1 and 3 exhibit broad spectral features, indicating a rather disordered V environment, in analogy to the Ti environment in the oxide NP matrix, as described previously. Annealing induces a sharpening of spectral features and a shift to higher energy of the main edge, as also found at the Ti edge. In annealed samples 2, 5, and 6, the pre-edge region is characterised by a sharp peak and a weak shoulder at higher photon energy. These pre-edge features, due to dipole and quadrupole transitions to bound hybridized orbitals originating from O p and V d atomic ones, are reminiscent of the pre-edge peak features of V_2O_5; the intensity of the pre-edge peak in the samples is, however, less than in V_2O_5. The main edge features of the spectra do not bear a strong correspondence to those of V_2O_5; especially significant is the energy onset of the main

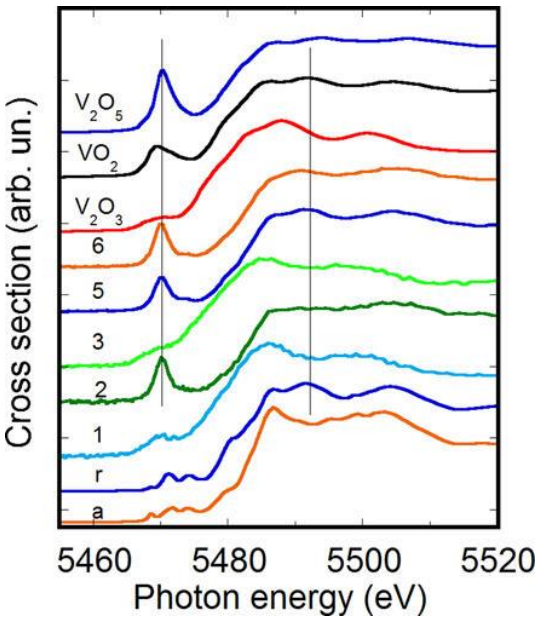

Figure 6.16 V K-edge XANES of selected samples and reference compounds. Also reported are the Ti K-edge spectra of rutile and anatase shifted by +500 eV. The vertical lines are guides to the eye.

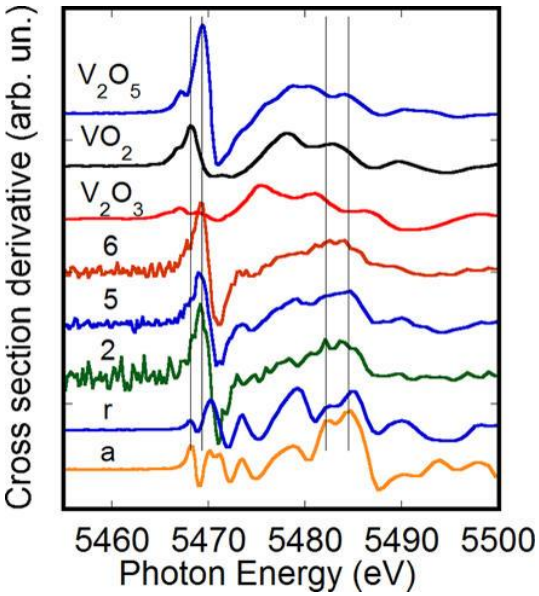

Figure 6.17 Derivatives of the spectra presented in Figure 6.16.

edge, which is significantly shifted to higher energies in the samples with respect to the reference V oxides. The closest (albeit not complete) correspondence is between spectra of sample 2 and anatase on one hand and, especially, between sample 5 and rutile on the other. Recall that analysis of the Ti-edge XANES and EXAFS indicated a local Ti environment similar to anatase in sample 2 and similar to rutile in sample 5. For sample 6, the Ti XANES pre- and main-edge features indicated a mixed environment, and this has a correspondence with the V *K*-edge spectrum. The V-edge data therefore strongly suggest that V substitutionally occupies a Ti site in the NP matrix, irrespective of whether it is similar to rutile, anatase, or mixed. Regarding the oxidation state, a conclusive result is difficult to reach with certainty since pre-edge and XANES lineshapes depend on the oxidation state of the absorber, its local point symmetry, and the elemental composition of its first coordination shells. Thus, it is not possible to rigorously compare spectra of V oxide reference compounds and of samples in which an isolated V is surrounded by a TiO_2 matrix. The coincidence of the energy position of the pre-edge peak of the samples with that of V_2O_5 suggests an oxidation state close to 5+. However, its intensity, intermediate between those of V_2O_5 and VO_2 pre-edge peaks, is also compatible with the presence of V^{4+} ions. A mixed oxidation state may arise from V occupying both bulk-like and surface-like sites in the NPs. In bulk-like sites, the most stable V oxidation state is 4+[98] because its associated donor transition level lies deep in the TiO_2 gap[92,113]. On the other hand, surface V ions may attain the 5+ oxidation state, most stable under oxygen-rich conditions. In the present case, due to the small NP size coupled with the positive energy of formation of the substitutional cationic defect, significant surface enrichment by V may be expected. In V-doped TiO_2 NPs prepared by chemical methods, the formation of V^{5+} vana-

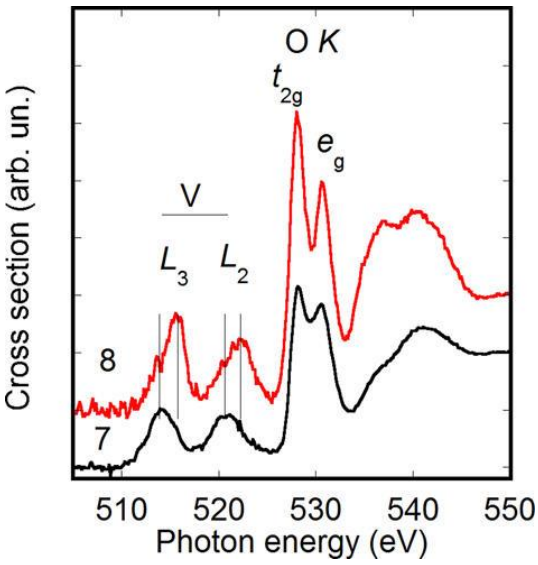

Figure 6.18 V $L_{2,3}$- and O K-edge XANES spectra in as-deposited sample 7 and annealed sample 8.

date surface-cluster species for V contents higher than about 5% was reported[91,98]. Surface enrichment by V^{5+} ions, which implies a stronger contribution from surface-like sites to the V *K*-edge spectra, may also account for the differences observed between the V *K*-edge and the shifted Ti *K*-edge XANES of nanoparticle-assembled films.

Besides contributing to band gap narrowing, V^{4+} ions can trap both electrons and holes, thus favouring charge separation and enhancing visible-light photocatalytic activity[98]. In addition, V^{5+} surface species were reported to scavenge photogenerated electrons from TiO_2 and to facilitate their transfer to oxygen molecules on the NP surface, eventually forming superoxide radicals active in the degradation of toxic dyes[91].

The sharpening of spectral features upon annealing and the blue-shift of V-related ones are also evident from combined V $L_{2,3}$- and O *K*-edge XANES spectra, reported in Figure 6.18. The lineshapes of the O *K*-edge spectra, in comparison to the literature[101,108], indicate once more a local structure intermediate between rutile and anatase for annealed sample 8.

Conclusion

In conclusion, a complete characterisation of V-doped TiO_2 NPs was carried, also thanks to the versatility of the IGC technique to prepare samples in forms suitable for a wide variety of measurements. The synthesised NPs are a mixture (mainly) composed of anatase and rutile with relative abundances that depend on the annealing treatment and the deposition rate. No

structural or morphological properties correlate with the V content, but optical properties do: the NPs band gap is effectively reduced by V addition. An in-depth study of the location of V dopants in TiO_2 NPs has been reported, showing that V ions occupy substitutional cationic sites in the TiO_2 matrix, irrespective of whether it is similar to rutile, anatase, or mixed. Therefore, IGC is a viable technique to grow nanoparticle-assembled metal-ion-doped TiO_2 films with an anatase-to-rutile ratio that can be tuned by adjusting the evaporation parameters.

FINAL REMARKS

This last discussion intends to give a global overlook of the main results presented through this Thesis and comment their implications for future research.

Advances in the gas condensation of NPs

The work done improving a synthesis technique has obvious implications in widening the possibilities of studying new systems. IGC is an old technique, dated back in the 1930s, that initially could prepare only metallic NPs but now many other materials can be synthesised.

One of the peculiar features of the set-up used in this Thesis is the double thermal source. It allows the simultaneous evaporation of any two compounds (compatibles with the IGC technique). It is only thanks to that that it has been made possible the co-deposition of Mg and Ti, elements which evaporate at very different temperatures, and observe the metastable formation of the Mg-Ti alloy.

The implementation of a reactive gas flow is such an important modification that deserved to also modify the name of the technique from inert to reactive gas condensation. The very first synthesis of NPs condensed directly into a hydride is showed using a He/H_2 gas mixture. Adding O_2 to the inert atmosphere, instead, it was possible to synthesise metal-oxide core-shell NPs. The combination of double thermal source and reactive gas flow permits the investigation of tri-elemental NPs (the Mg-Ti-H case has been showed). In

principle it is possible to study also quaternary or higher systems, evaporating alloys or other compounds instead of pure elements and using other reactive gas mixtures.

The great versatility of this technique involves not only the range of materials it can synthesise but also the types of sample. The NPs can be in "free-standing" nanopowder form, compact pellets or films deposited on any type of substrate, depending on their application. This is an important feature also to make available many different investigation techniques; for example, it was crucial to completely characterise the V-TiO_2 NPs, few milligrams of nanopowder were required for XRD measurements, while a film deposited on a substrate was needed by XAS experiments.

Moreover, this gas condensation set-up has some new *in situ* capabilities. Right after the evaporation, the NPs can be annealed in vacuum or in a controlled atmosphere, taking advantage of the ultra-clean ambient inside the chambers. The development of an *in situ* Sievert apparatus is of great use in the study of the true gas-solid reaction properties, especially for materials sensitive to impurities.

For all these reasons the gas condensation technique can be still considered as a modern technique, that can satisfy the growing interest in complex NPs both from a compositional and morpho-structural point of view.

Mg-based NPs

The chapters focussing on Mg-based NPs have to be considered as parts of the same research: in the search of a Mg-based H-storage material, it was observed that pure Mg NPs could not be prepared, because they grow already at room temperature into single crystals losing their "nano" nature. The mechanism responsible for the self-assembly of Mg NPs is found to be the grain rotation coalescence/oriented attachment. The RGC synthesis of Mg NPs using O_2 creates an oxide layer around the metallic core that keeps the NPs in the 20-30 nm size range, however these Mg-MgO NPs did not show interesting H-storage properties despite other reports[114]. This is a general approach for the stabilisation of small NPs that can be used in other systems that face the same problem.

The addition of Ti, instead, showed a great enhancement of the H-sorption properties. The condensation of the Mg and Ti vapours ended up in the metastable solution of Ti in Mg which is however lost after the first hydro-

genation turning the NPs into MgH_2-TiH_2 nanocomposites. The same material is obtained in the synthesis of Mg-Ti NPs by RGC using H_2. Compacted pellet samples can be handled more easily and are more air-stable because of their reduced porosity but, for the very same reasons, exhibit slightly poorer H-storage properties than the nanopowder counterpart. The best performances are achieved for the Mg nanopowders with 6 at% addition of Ti, a good compromise between high H storage capacity (5.3 wt%) and very fast kinetics. The great rapidity of the H-sorption kinetics of this material is due to the high surface-to-volume ratio (that improves the hydrogen and thermal exchange with the environment), the fine TiH_2 crystallites embedded in the MgH_2 NPs and their high purity, *i.e.* the low MgO content. Low temperature kinetics, even at room temperature, are found in literature on Mg-based materials usually for absorptions only; rarely[115,116], H desorptions are reported at temperatures below 473 K. Thanks to the great performances of the Mg-Ti NPs and to the development of the *in situ* Sievert apparatus it was possible to measure both absorptions and desorptions at temperatures as low as 343 K. For the same reason, also equilibrium measurements span over a wide temperature range where no clear modifications of the thermodynamics of the bulk Mg-H system were found.

V-doping of TiO_2 NPs

Controlled V addition to TiO_2 NPs was achieved by IGC calibrating the V content of the precursor Ti-V alloy. The V addition induced visible optical changes in the colour of the samples, correlated with a decrease of the energy band gap and a higher light absorption in the visible range as the V content increases. The TiO_2 NPs resulted in a mixture of mainly rutile and anatase polymorphs with relative compositions depending on the annealing treatment and on the average NP size, in turn depending on the evaporation rate. No structural changes were observed changing the V content and it has been proved that V is incorporated in the TiO_2 matrix, substitutional of Ti, disregarding whether it is in the rutile or anatase phase.

This Thesis may be over, but research never is; other experiments are ongoing on this system, like the measurement of the photoelectrochemical properties and the characterisation of RGC (with O_2) synthesised NPs.

BIBLIOGRAPHY

List of publications

1. M. Ponthieu, M. Calizzi, L. Pasquini, J.F. Fernández and F. Cuevas, "*Synthesis by reactive ball milling and cycling properties of MgH_2-TiH_2 nanocomposites: Kinetics and isotopic effects*", International Journal of Hydrogen Energy 39 (2014) 9918-9923, http://dx.doi.org/10.1016/j.ijhydene.2014.01.055;
2. F. Venturi, M. Calizzi, S. Bals, T. Perkisas and L. Pasquini, "*Self-assembly of gas-phase synthesized magnesium nanoparticles on room temperature substrates*", Material Research Express 2 (2015) 015007, http://dx.doi.org/10.1088/2053-1591/2/1/015007;
3. M. Calizzi, F. Venturi, M. Ponthieu, F. Cuevas, V. Morandi, T. Perkisas, S. Bals and L. Pasquini, "*Gas-phase synthesis of Mg–Ti nanoparticles for solid-state hydrogen storage*", Physical Chemistry Chemical Physics 18 (2016) 141-148, http://dx.doi.org/10.1039/C5CP03092G;
4. Molinari, F. D'Amico, M. Calizzi, Y. Zheng, C. Boelsma, L. Mooij, Y. Lei, H. Hahn, B. Dam and L. Pasquini, "*Interface and strain effects on the H-sorption thermodynamics of size-selected Mg nanodots*", International Journal of Hydrogen Energy 41 (2016) 9841-9851, http://dx.doi.org/10.1016/j.ijhydene.2016.02.003;
5. G. Rossi, M. Calizzi, V. Di Cintio, S. Magkos, L. Amidani, L. Pasquini and F. Boscherini, "*Local Structure of V Dopants in TiO_2 Nanoparticles: X-ray Absorption Spectroscopy, Including Ab-Initio and Full Potential Simulations*", The Journal of Physical Chemistry C 120 (2016) 7457-7466, http://dx.doi.org/10.1021/acs.jpcc.5b12045;
6. M. Calizzi, D. Chericoni, L.H. Jepsen, T.R. Jensen and L. Pasquini, "*Mg–Ti nanoparticles with superior kinetics for hydrogen storage*", International Journal of Hydrogen Energy 41 (2016) 14447-14454, http://dx.doi.org/10.1016/j.ijhydene.2016.03.071;
7. M. Gajdics, M. Calizzi, L. Pasquini, E. Schafler and Á. Révész, "*Characterization of a nanocrystalline Mg–Ni alloy processed by high-pressure torsion during hydrogenation and dehydrogenation*",

International Journal of Hydrogen Energy 41 (2016) 9803-9809, http://dx.doi.org/10.1016/j.ijhydene.2015.12.224;

8. Á. Révész, M. Gajdics, E. Schafler, M. Calizzi and L. Pasquini, *"Dehydrogenation-hydrogenation characteristics of nanocrystalline Mg2Ni powders compacted by high-pressure torsion"*, Journal of Alloys and Compounds, accepted.

References

1. 15 Global Challenges. Available at: http://www.millennium-project.org/millennium/challenges.html. (Accessed: 16th January 2017)
2. Archer, D. *Global warming : understanding the forecast*. (John Wiley & Sons, 2012).
3. International Energy Agency. Key World Energy Statistics. 80 (2016). Available at: http://www.iea.org/publications/freepublications/publication/key-world-energy-statistics.html.
4. Nanotechnology Timeline | Nano. Available at: https://www.nano.gov/timeline.
5. Granqvist, C. G. & Buhrman, R. A. Ultrafine metal particles. *J. Appl. Phys.* **47,** 2200–2219 (1976).
6. Binns, C. Nanoclusters deposited on surfaces. *Surf. Sci. Rep.* **44,** 1–49 (2001).
7. Birringer, R., Gleiter, H., Klein, H. P. & Marquardt, P. Nanocrystalline materials an approach to a novel solid structure with gas-like disorder? *Phys. Lett. A* **102,** 365–369 (1984).
8. Balluffi, R. W., Allen, S. M. & Carter, W. C. *Kinetics of Materials*. *John Wiley & Sons* (2005). doi:10.1002/0471749311
9. Lutterotti, L., Bortolotti, M., Ischia, G., Londarelli, I. & Wenk, H.-R. Rietveld texture analysis from diffraction images. *Zeitschrift für Krist. Suppl.* **26,** 125–130 (2007).
10. Graham, T. On the Absorption and Dialytic Separation of Gases. *Philos. Trans. R. Soc. London* **156,** 399–439 (1866).
11. Walker, G. B. & Marezio, M. Lattice parameters and zone overlap in solid solutions of lead in magnesium. *Acta Metall.* **7,** 769–773 (1959).
12. Bortz, M., Bertheville, B., Böttger, G. & Yvon, K. Structure of the

high pressure phase γ-MgH2 by neutron powder diffraction. *J. Alloys Compd.* **287,** L4–L6 (1999).

13. *Technical System Targets: Onboard Hydrogen Storage for Light-Duty Fuel Cell Vehicles*. (2012).
14. Paskevicius, M., Sheppard, D. A. & Buckley, C. E. Thermodynamic changes in mechanochemically synthesized magnesium hydride nanoparticles. *J. Am. Chem. Soc.* **132,** 5077–5083 (2010).
15. Jepsen, L. H. *et al.* Boron-nitrogen based hydrides and reactive composites for hydrogen storage. *Mater. Today* **17,** 129–135 (2014).
16. Ley, M. B. *et al.* Complex hydrides for hydrogen storage - New perspectives. *Mater. Today* **17,** 122–128 (2014).
17. Liang, G. Synthesis and hydrogen storage properties of Mg-based alloys. *J. Alloys Compd.* **370,** 123–128 (2004).
18. Lu, J., Choi, Y. J., Fang, Z. Z., Sohn, H. Y. & Boule, V. Hydrogen Storage Properties of Nanosized MgH2-0.1TiH2 Prepared by Ultrahigh-Energy-High-Pressure Milling. *J. Am. Chem. Soc.* **131,** 15843–15852 (2009).
19. Cuevas, F., Korablov, D. & Latroche, M. Synthesis, structural and hydrogenation properties of Mg-rich MgH2–TiH2 nanocomposites prepared by reactive ball milling under hydrogen gas. *Phys. Chem. Chem. Phys.* **14,** 1200 (2012).
20. Liang, G. & Schulz, R. Synthesis of Mg-Ti alloy by mechanical alloying. *J. Mater. Sci.* **38,** 1179–1184 (2003).
21. Mooij, L. P. A. *et al.* Interface energy controlled thermodynamics of nanoscale metal hydrides. *Adv. Energy Mater.* **1,** 754–758 (2011).
22. Vermeulen, P., Niessen, R. A. H. & Notten, P. H. L. Hydrogen storage in metastable $\mathrm{MgyTi(1\&\#xa0;-\&\#xa0;y)}$ thin films. *Electrochem. commun.* **8,** 27–32 (2006).
23. Borsa, D. M. *et al.* Structural, optical, and electrical properties of Mgy Ti1-y Hx thin films. *Phys. Rev. B - Condens. Matter Mater. Phys.* **75,** 1–9 (2007).
24. Liu, Y., Zou, J., Zeng, X. & Ding, W. A co-precipitated Mg-Ti nano-composite with high capacity and rapid hydrogen absorption kinetics at room temperature. *RSC Adv.* **4,** 42764–42771 (2014).
25. Baldi, A., Gonzalez-Silveira, M., Palmisano, V., Dam, B. & Griessen, R. Destabilization of the Mg-H system through elastic constraints. *Phys. Rev. Lett.* **102,** 1–4 (2009).

26. Pasquini, L. *et al.* Hydride destabilization in core-shell nanoparticles. *Int. J. Hydrogen Energy* **39,** 2115–2123 (2014).
27. Ostwald, W. -. *Z. Phys. Chem.* **37,** 385 (1901).
28. Lifshitz, I. M. & Slyozov, V. V. The kinetics of precipitation from supersaturated solid solutions. *J. Phys. Chem. Solids* **19,** 35–50 (1961).
29. Wagner, C. Theorie der Alterung von Niederschlägen durch Umlösen (Ostwald-Reifung). *Zeitschrift für Elektrochemie* **65,** 581–591 (1961).
30. Talapin, D. V., Rogach, A. L., Haase, M. & Weller, H. Evolution of an ensemble of nanoparticles in a colloidal solution: Theoretical study. *J. Phys. Chem. B* **105,** 12278–12285 (2001).
31. Kuo, C. L. & Hwang, K. C. Does morphology of a metal nanoparticle play a role in Ostwald ripening processes? *Chem. Mater.* **25,** 365–371 (2013).
32. Lee Penn, R. & Banfield, J. L. Imperfect Oriented Attachment: Dislocation Generation in Defect-Free Nanocrystals. *Science (80-.).* **281,** 969–971 (1998).
33. Harris, K. E., Singh, V. V. & King, A. H. Grain rotation in thin films of gold. *Acta Mater.* **46,** 2623–2633 (1998).
34. Leite, E. R. *et al.* Crystal growth in colloidal tin oxide nanocrystals induced by coalescence at room temperature. *Appl. Phys. Lett.* **83,** 1566–1568 (2003).
35. Zhang, J., Huang, F. & Lin, Z. Progress of nanocrystalline growth kinetics based on oriented attachment. *Nanoscale* **2,** 18–34 (2010).
36. Jia, G. *et al.* Couples of Colloidal Semiconductor Nanorods Formed By Self-Limited Assembly. *Nat. Mater.* **13,** 301–307 (2014).
37. Flagan, R. C. & Lunden, M. M. Particle structure control in nanoparticle synthesis from the vapor phase. *Mater. Sci. Eng. A* **204,** 113–124 (1995).
38. Höfler, H. J., Averback, R. S., Hahn, H. & Gleiter, H. Diffusion of bismuth and gold in nanocrystalline copper. *J. Appl. Phys.* **74,** 3832–3839 (1993).
39. Friedrichs, O., Kolodziejczyk, L., Sánchez-López, J. C., López-Cartés, C. & Fernández, A. Synthesis of nanocrystalline MgH2 powder by gas-phase condensation and in situ hydridation: TEM, XPS and XRD study. *J. Alloys Compd.* **434–435,** 721–724 (2007).
40. Pasquini, L. *et al.* Metal-hydride transformation kinetics in Mg nanoparticles. *Appl. Phys. Lett.* **94,** 41918 (2009).

41. Callini, E. *et al.* Hydrogen sorption in Pd-decorated Mg-MgO core-shell nanoparticles. *Appl. Phys. Lett.* **94,** 221905 (2009).
42. Kooi, B. J., Palasantzas, G. & De Hosson, J. T. M. Gas-phase synthesis of magnesium nanoparticles: A high-resolution transmission electron microscopy study. *Appl. Phys. Lett.* **89,** 161914 (2006).
43. Kim, K. C., Dai, B., Johnson, J. K. & Sholl, D. S. Assessing nanoparticle size effects on metal hydride thermodynamics using the Wulff construction. *Nanotechnology* **20,** 204001 (2009).
44. Margrave, J. L. Vapour pressure of the elements (Nesmeyanov, An. N.). *J. Chem. Educ.* **41,** A590 (1964).
45. Bardotti, L., Jensen, P., Hoareau, A., Treilleux, M. & Cabaud, B. Experimental observation of fast diffusion of large antimony clusters on graphite surfaces. *Phys. Rev. Lett.* **74,** 4694–4697 (1995).
46. Jensen, P., Barabsi, A. L., Larralde, H., Havlin, S. & Stanley, H. E. Deposition, diffusion, and aggregation of atoms on surfaces: A model for nanostructure growth. *Phys. Rev. B* **50,** 15316–15329 (1994).
47. Yoon, B. *et al.* Morphology control of the supported islands grown from soft-landed clusters. *Surf. Sci.* **443,** 76–88 (1999).
48. Moldovan, D., Wolf, D. & Phillpot, S. R. Theory of diffusion-accommodated grain rotation in columnar polycrystalline microstructures. *Acta Mater.* **49,** 3521–3532 (2001).
49. Moldovan, D., Yamakov, V., Wolf, D. & Phillpot, S. R. Scaling behavior of grain-rotation-induced grain growth. *Phys. Rev. Lett.* **89,** 206101 (2002).
50. Tang, J.-J., Yang, X.-B., OuYang, L., Zhu, M. & Zhao, Y.-J. A systematic first-principles study of surface energies, surface relaxation and Friedel oscillation of magnesium surfaces. *J. Phys. D. Appl. Phys.* **47,** 115305 (2014).
51. Yin, Y. *et al.* Formation of Hollow Nanocrystals Through the Nanoscale Kirkendall Effect. *Science (80-.).* **304,** (2004).
52. Lide, D. R. CRC Handbook of Chemistry and Physics. 3485 (2003). doi:978-1466571143
53. Asano, K., Enoki, H. & Akiba, E. Synthesis of HCP, FCC and BCC structure alloys in the Mg-Ti binary system by means of ball milling. *J. Alloys Compd.* **480,** 558–563 (2009).
54. Asano, K. *et al.* Synthesis and structural study of Ti-rich Mg-Ti hydrides. *J. Alloys Compd.* **593,** 132–136 (2014).

55. Anastasopol, A. *et al.* Reduced Enthalpy of Metal Hydride Formation for Mg–Ti Nanocomposites Produced by Spark Discharge Generation. *J. Am. Chem. Soc.* **135,** 7891–7900 (2013).
56. Krishnan, G. *et al.* Synthesis and exceptional thermal stability of Mg-based bimetallic nanoparticles during hydrogenation. *Nanoscale* **6,** 11963–11970 (2014).
57. Ellinger, F. H. *et al.* The preparation and some properties of magnesium hydride. *J. Am. Chem. Soc.* **77,** 2647–2648 (1955).
58. Rongeat, C. *et al.* Determination of the Heat of Hydride Formation/Decomposition by High-Pressure Differential Scanning Calorimetry (HP-DSC). *J. Phys. Chem. B* **111,** 13301–13306 (2007).
59. Murray, J. L. The Mg-Ti (Magnesium-Titanium) system. *Bull. Alloy Phase Diagrams* **7,** 245–248 (1986).
60. Suryanarayana, C. & Froes, F. H. Nanocrystalline titanium-magnesium alloys through mechanical alloying. *J. Mater. Res.* **5,** 1880–1886 (1990).
61. Rousselot, S., Guay, D. & Roué, L. Synthesis of fcc Mg–Ti–H alloys by high energy ball milling: Structure and electrochemical hydrogen storage properties. *J. Power Sources* **195,** 4370–4374 (2010).
62. Korablov, D., Besenbacher, F. & Jensen, T. R. Ternary compounds in the magnesium–titanium hydrogen storage system. *Int. J. Hydrogen Energy* **39,** 9700–9708 (2014).
63. Asano, K., Enoki, H. & Akiba, E. Synthesis of Mg-Ti FCC hydrides from Mg-Ti BCC alloys. *J. Alloys Compd.* **478,** 117–120 (2009).
64. Moser, D. *et al.* Structure and stability of high pressure synthesized Mg–TM hydrides (TM = Ti, Zr, Hf, V, Nb and Ta) as possible new hydrogen rich hydrides for hydrogen storage. *J. Mater. Chem.* **19,** 8150 (2009).
65. Kyoi, D. *et al.* A new ternary magnesium-titanium hydride Mg7TiHx with hydrogen desorption properties better than both binary magnesium and titanium hydrides. *J. Alloys Compd.* **372,** 213–217 (2004).
66. Ponthieu, M. *et al.* Structural properties and reversible deuterium loading of MgD 2-TiD2 nanocomposites. *J. Phys. Chem. C* **117,** 18851–18862 (2013).
67. Venturi, F., Calizzi, M., Bals, S., Perkisas, T. & Pasquini, L. Self-assembly of gas-phase synthesized magnesium nanoparticles on room

temperature substrates. *Mater. Res. Express* **2,** (2015).

68. Tao, S., Notten, P., van Santen, R. & Jansen, A. Density functional theory studies of the hydrogenation properties of Mg and Ti. *Phys. Rev. B* **79,** 1–7 (2009).
69. Hirscher, M. *et al. Handbook of Hydrogen Storage*. *Topics in applied physics* **12,** (2010).
70. Asano, K. *et al.* Destabilization of Mg Hydride by Self-Organized Nanoclusters in the Immiscible Mg-Ti System. *J. Phys. Chem. C* **119,** 12157–12164 (2015).
71. Hao, S. Q. & Sholl, D. S. Effect of TiH2-induced strain on thermodynamics of hydrogen release from MgH2. *J. Phys. Chem. C* **116,** 2045–2050 (2012).
72. Noritake, T. *et al.* Chemical bonding of hydrogen in MgH2. *Appl. Phys. Lett.* **81,** 2008–2010 (2002).
73. Kalita, P. E., Cornelius, A. L., Lipinska-Kalita, K. E., Gobin, C. L. & Peter Liermann, H. In situ observations of temperature- and pressure-induced phase transitions in TiH2: Angle-dispersive and synchrotron energy-dispersive X-ray diffraction studies. *J. Phys. Chem. Solids* **69,** 2240–2244 (2008).
74. Hansen, B. R. S. *et al. In situ* X-ray diffraction environments for high-pressure reactions. *J. Appl. Crystallogr.* **48,** 1234–1241 (2015).
75. Fernández, J. F. & Sánchez, C. R. Rate determining step in the absorption and desorption of hydrogen by magnesium. *J. Alloys Compd.* **340,** 189–198 (2002).
76. Barkhordarian, G., Klassen, T. & Bormann, R. Effect of Nb2O5 content on hydrogen reaction kinetics of Mg. *J. Alloys Compd.* **364,** 242–246 (2004).
77. Molinari, A. *et al.* Interface and strain effects on the H-sorption thermodynamics of size-selected Mg nanodots. *Int. J. Hydrogen Energy* **41,** 9841–9851 (2016).
78. Shen, P., Hwang, S.-L., Chu, H.-T. & Yui, T.-F. α-PbO 2 –Type TiO 2 : From Mineral Physics to Natural Occurrence. *Int. Geol. Rev.* **43,** 366–378 (2001).
79. Akimoto, J. *et al.* Topotactic Oxidation of Ramsdellite-Type Li0.5TiO2, a New Polymorph of Titanium Dioxide: TiO2(R). *Journal of Solid State Chemistry* **113,** 27–36 (1994).
80. Sato, H. *et al.* Baddeleyite-Type High-Pressure Phase of TiO2. *Science*

(80-.). **251,** 786–788 (1991).

81. Dubrovinskaia, N. A. *et al.* Experimental and theoretical identification of a new high-pressure TiO2 polymorph. *Phys. Rev. Lett.* **87,** 275501 (2001).
82. Mattesini, M. *et al.* High-pressure and high-temperature synthesis of the cubic TiO2 polymorph. *Phys. Rev. B - Condens. Matter Mater. Phys.* **70,** 1–4 (2004).
83. Dubrovinsky, L. S. *et al.* Materials science. The hardest known oxide. *Nature* **410,** 653–654 (2001).
84. Lazzeri, M., Vittadini, A. & Selloni, A. Structure and energetics of stoichiometric TiO2 anatase surfaces. *Phys. Rev. B - Condens. Matter Mater. Phys.* **63,** 1554091–1554099 (2001).
85. Di Paola, A., Bellardita, M. & Palmisano, L. *Brookite, the Least Known TiO 2 Photocatalyst*. *Catalysts* **3,** (2013).
86. Fujishima, A., Zhang, X. & Tryk, D. A. TiO2 photocatalysis and related surface phenomena. *Surf. Sci. Rep.* **63,** 515–582 (2008).
87. Morgan, B. J. & Watson, G. W. Intrinsic n-type defect formation in TiO2: A comparison of rutile and anatase from GGA+U calculations. *J. Phys. Chem. C* **114,** 2321–2328 (2010).
88. van de Krol, R. & Gratzel, M. *Photoelectrochemical Hydrogen Production*. (Springer, 2012).
89. Luttrell, T. *et al.* Why is anatase a better photocatalyst than rutile?--Model studies on epitaxial TiO2 films. *Sci. Rep.* **4,** 4043 (2014).
90. Bellardita, M., Di Paola, A., Megna, B. & Palmisano, L. Absolute crystallinity and photocatalytic activity of brookite TiO2 samples. *Appl. Catal. B Environ.* **201,** 150–158 (2017).
91. Jaiswal, R., Patel, N., Kothari, D. C. & Miotello, A. Improved visible light photocatalytic activity of TiO2 co-doped with Vanadium and Nitrogen. *Appl. Catal. B Environ.* **126,** 47–54 (2012).
92. Umebayashi, T., Yamaki, T., Itoh, H. & Asai, K. Analysis of electronic structures of 3d transition metal-doped TiO2 based on band calculations. *J. Phys. Chem. Solids* **63,** 1909–1920 (2002).
93. Asahi, R., Morikawa, T., Ohwaki, T., Aoki, K. & Taga, Y. Visible-Light Photocatalysis in Nitrogen-Doped Titanium Oxides. *Science (80-.).* **293,** (2001).
94. CRCT, École Polytechnique de Montréal. Available at: http://www.crct.polymtl.ca/FACT/documentation/.

95. Pasquini, L. *et al.* Size and oxidation effects on the vibrational properties of nanocrystalline α-Fe. *Phys. Rev. B* **66,** 73410 (2002).
96. Wood, D. L. & Tauc, J. Weak absorption tails in amorphous semiconductors. *Phys. Rev. B* **5,** 3144–3151 (1972).
97. Avansi, W., Arenal, R., de Mendonça, V. R., Ribeiro, C. & Longo, E. Vanadium-doped TiO2 anatase nanostructures: the role of V in solid solution formation and its effect on the optical properties. *CrystEngComm* **16,** 5021 (2014).
98. Kubacka, A., Fuerte, A., Martínez-Arias, A. & Fernández-García, M. Nanosized Ti–V mixed oxides: Effect of doping level in the photocatalytic degradation of toluene using sunlight-type excitation. *Appl. Catal. B Environ.* **74,** 26–33 (2007).
99. Liu, J. *et al.* Enhanced Photoactivity of V−N Codoped TiO_2 Derived from a Two-Step Hydrothermal Procedure for the Degradation of PCP−Na under Visible Light Irradiation. *J. Phys. Chem. C* **115,** 4507–4515 (2011).
100. Chang, S. & Liu, W. Surface doping is more beneficial than bulk doping to the photocatalytic activity of vanadium-doped TiO2. *Appl. Catal. B Environ.* **101,** 333–342 (2011).
101. Kucheyev, S. O. *et al.* Electronic structure of titania aerogels from soft x-ray absorption spectroscopy. *Phys. Rev. B* **69,** 245102 (2004).
102. Hanley, T. L., Luca, V., Pickering, I. & Howe, R. F. Structure of Titania Sol-Gel Films : A Study by X-Ray Absorption Spectroscopy. *Society* 1153–1160 (2002). doi:10.1021/JP012225H
103. Luca, V., Djajanti, S. & Howe, R. F. Structural and Electronic Properties of Sol−Gel Titanium Oxides Studied by X-ray Absorption Spectroscopy. *J. Phys. Chem. B* **102,** 10650–10657 (1998).
104. Luca, V. Comparison of Size-dependent structural and electronic properties of anatase and rutile nanoparticles. *J. Phys. Chem. C* **113,** 6367–6380 (2009).
105. Marchiori, C. *et al.* Unraveling the Cooperative Mechanism of Visible-Light Absorption in Bulk N,Nb Codoped TiO2 Powders of Nanomaterials. *J. Phys. Chem.* **118,** 24152−24164 (2014).
106. Wong, J., Lytle, F. W., Messmer, R. P. & Maylotte, D. H. K-edge absorption spectra of selected vanadium compounds. *Phys. Rev. B* **30,** 5596–5610 (1984).
107. Hanaor, D. A. H. & Sorrell, C. C. Review of the anatase to rutile

phase transformation. *J. Mater. Sci.* **46,** 855–874 (2011).
108. Stewart, S. J., Fernández-García, M., Belver, C., Simon Mun, B. & Requejo, F. G. Influence of N-doping on the structure and electronic properties of titania nanoparticle photocatalysts. *J. Phys. Chem. B* **110,** 16482–16486 (2006).
109. De Groot, F. M. F. *et al.* 2p X-ray absorption of titanium in minerals. *Phys. Chem. Miner.* **19,** 140–147 (1992).
110. Bianconi, A. Multiplet splitting of final-state configurations in x-ray-absorption spectrum of metal VO2: Effect of core-hole-screening, electron correlation, and metal-insulator transition. *Phys. Rev. B* **26,** 2741–2747 (1982).
111. Sutton, S. R. *et al.* Vanadium K edge XANES of synthetic and natural basaltic glasses and application to microscale oxygen barometry. *Geochim. Cosmochim. Acta* **69,** 2333–2348 (2005).
112. Whittaker, L., Wu, T.-L., Patridge, C. J., Sambandamurthy, G. & Banerjee, S. Distinctive Finite Size Effects on the Phase Diagram and Metal–Insulator Transitions of Tungsten-Doped Vanadium(IV) Oxide. *J. Mater. Chem.* **21,** 5580–5592 (2011).
113. Osorio-Guill??n, J., Lany, S. & Zunger, A. Atomic control of conductivity versus ferromagnetism in wide-gap oxides via selective doping: V, Nb, Ta in anatase TiO2. *Phys. Rev. Lett.* **100,** (2008).
114. Ares-Fernández, J.-R. & Aguey-Zinsou, K.-F. Superior MgH2 Kinetics with MgO Addition: A Tribological Effect. *Catalysts* **2,** 330–343 (2012).
115. Jeon, K.-J. *et al.* Air-stable magnesium nanocomposites provide rapid and high-capacity hydrogen storage without using heavy-metal catalysts. *Nat. Mater.* **10,** 286–290 (2011).
116. Hanada, N., Ichikawa, T., Hino, S. & Fujii, H. Remarkable improvement of hydrogen sorption kinetics in magnesium catalyzed with Nb2O5. *J. Alloys Compd.* **420,** 46–49 (2006).
117. Dambournet, D., Belharouak, I. & Amine, K. Tailored preparation methods of TiO2 anatase, rutile, brookite: Mechanism of formation and electrochemical properties. *Chem. Mater.* **22,** 1173–1179 (2010).
118. Bertani, R. *Solids and surfaces. A chemist's view of bonding in extended structures. Inorganica Chimica Acta* **168,** (1990).
119. Linsebigler, A. L. *et al.* Photocatalysis on TiO2 Surfaces: Principles, Mechanisms, and Selected Results. *Chem. Rev.* **95,** 735–758 (1995).

ACKNOWLEDGEMENTS

During these three years I had the chance to meet and work with a lot of people, that I wish to thank and acknowledge for the contribution they gave in the research resumed in this Thesis and for the things I learned from them.

First of all, I wish to thank Professor Luca Pasquini. I am sincerely grateful for having had him as a supervisor, which I consider more like a mentor; he always showed me esteem and trust, taught me all sort of things and was always available when I needed him. Thank you for caring about me and for giving me the best PhD experience.

I want to thank my colleagues (former and current) for the everyday collaboration and for creating a wonderful atmosphere in the lab and in the office, I rarely had the impression of going "to work". Thank you Prof. Boscherini and Giacomo, Laura, Lucia, Martina, Maria, Filippo, Tobias, Isacco, Andrea, Marco. Many thanks to the bachelor and master students that helped me: Azzurra, Domizia, Valeria, Matteo, Federico, Simone, Maurizio and the one that became also my deskmate, Nicola.

I really want to thank Prof. Züttel for hosting me in his laboratory for six months and all the people from LMER for their warm welcome. Thank you Elsa, Kun, Constance, Mariana, Shunske, David, Jérémie and Robin.

I want to thank for their collaboration Prof. Jensen and his group from the Aarhus University, Prof. Falini and Matteo from the department of Chemistry, Dr. Morandi and Dr. Migliori from IMM-CNR.

I cannot end this Thesis without thanking my friends, even if I wanted to. Many thanks to all the balotta.

Above all, my family.
"I owe you all I am".